Superbubble Feedback in Galaxy Evolution

Superbubble Feedback in Galaxy Evolution

By B.W. Keller,
B. Sc. University of Calgary 2011

A Thesis Submitted to the School of Graduate Studies in Partial Fulfilment of the Requirements for the Degree Doctor of Philosophy

McMaster University

Doctor of Philosophy (2017) McMaster University
(Physics & Astronomy) Hamilton, Ontario

TITLE: Superbubble Feedback in Galaxy Evolution

AUTHOR: B.W. Keller

SUPERVISOR: Professor James W. Wadsley

NUMBER OF PAGES: ix, 182

Abstract

Galaxy formation is a complex, nonlinear process that occurs over scales that span orders of magnitude in space and time. Of the many phenomena taking place within a galaxy, supernovae (SN) are among the most important. SN heat, stir, and eject gas from the galaxy. This has profound impact on the galaxy's evolution over cosmic time. Numerical simulations of galaxies must often include models for feedback from SN. We present a new model for SN feedback that captures the effects of previously ignored physics: thermal conduction. Massive stars form in clusters, allowing their SN ejecta to merge into a superbubble, which can vent from the disc to drive a high-entropy galactic outflow. Thermal conduction determines how much mass is mixed into this superbubble.

We use this to study SN feedback in galaxy evolution, and come to four major conclusions. First, superbubbles drive stronger galactic outflows in compared to past models of SN feedback. Second, these outflows are key to both preventing the over-production of stars and the formation of too-massive central bulges. High redshift outflows eject starforming gas, and preferentially remove bulge forming gas. Third, we show that SN cannot prevent runaway star formation in galaxies more massive than our own ($M_{halo} > 10^{12}$ M$_\odot$). In these galaxies, SN are unable to prevent transport of gas towards the centre of the galaxy. These results suggest a transition between regulation from stars to regulation from supermassive black holes occurs at roughly this mass. Finally, we use our simulated galaxies to show recent observations of the Radial Acceleration Relation (RAR) are consistent with ΛCDM cosmology. The RAR ties galaxy kinematics to baryonic mass, in a tight, universal scaling relation. While this has been claimed as potential evidence of exotic new physics, we show this same tight relation occurs for galaxies formed in ΛCDM.

Co-Authorship

Chapters 2,3,4, and 5 of this thesis contain original scientific research written by myself, B.W. Keller. Chapters 2-4 have been published as peer-reviewed journal articles in the Monthly Notices of the Royal Astronomical Society (MNRAS). Chapter 5 has been published as a peer-reviewed journal articles in The Astrophysical Journal Letters (ApJL). The first work is referenced as: *Keller, B.W., Wadsley, J., Benincasa, S.M., & Couchman, H.M.P. 2014, MNRAS Volume 442, Issue 4, pp. 3013-3025.* My supervisor, Dr. James Wadsley, is the second author. Samantha Benincasa, the third author, helped test and run the method. Dr Hugh Couchman is the fourth author. The second work is referenced as: *Keller, B.W., Wadsley, J., Couchman, H.M.P 2015, MNRAS Volume 453, Issue 4, pp. 3499-3509.* Once again, Dr. James Wadsley and Dr. Hugh Couchman are co-authors. The third publication is referenced as: *Keller, B.W., Wadsley, J., Couchman, H.M.P. 2016, MNRAS Volume 463, Issue 2, pp. 1431-1445.* Again, Dr. James Wadsley and Dr. Hugh Couchman are co-authors. The final publication has the author list: *Keller, B.W. & Wadsley, J.W. 2017, ApJL Volume 853, Issue 1, pp. 17-22.* Dr. James Wadsley is the only co-author for this letter. All previously published material has been reformatted to conform to the required thesis style. I hereby grant an irrevocable, non-exclusive license to McMaster University and the National Library of Canada to reproduce this material as part of this thesis.

Acknowledgements

The work presented here would not have been possible without the immense help of my supervisor and collaborators. Thank you to James Wadsley for exemplifying Proverbs 27:17, and for helping steer me on to a successful path. Thanks to Hugh Couchman for your unfailingly sage advice. Thanks to Samantha Benincasa for always being there to raise an eyebrow at the right moment. To my collaborators beyond McMaster, thanks for showing me the forest beyond the trees. To my parents, thank you for instilling in me a lifelong love of learning. I wouldn't be here without your love and guidance making me the person I am today. To my friends in Calgary, I miss you all, and I wish I could have been with you during this journey. Finally, to my beloved wife: there aren't enough pages here to do this justice, so thank you for standing beside me.

Dedicated to Walter Labchuk. I wish I could have met you...

Contents

List of Figures

List of Tables

List of Acronyms

Λ **CDM** Cosmological Constant and Cold Dark Matter Cosmology

AGN Active Galactic Nucleus

AGORA Assembling Galaxies of Resolved Anatomy

AHF AMIGA's Halo Finder

APOSTLE A Project of Simulations of the Local Environment

B/T Bulge/Total

CDM Cold Dark Matter Cosmology

CFHT Canada-France-Hawaii Telescope

CGM Circumgalactic Medium

CMB Cosmic Microwave Background Radiation

COS Cosmic Origins Spectrograph

CR Cosmic Ray

DM Dark Matter

EAGLE Evolution and Assembly of Galaxies and their Environments

FB Feedback

FIRE Feedback in Realistic Environments

GIMIC Galaxies Intergalactic Medium Interaction Calculation

HI Neutral Hydrogen

IC Initial Conditions

IGM Intergalactic Medium

IMF Initial Mass Function

IR Infrared

ISM Interstellar Medium

MAGICC Making Galaxies in a Cosmological Context

MOND Modified Newtonian Dynamics

MUGS McMaster Unbiased Galaxy Simulations

MW Milky Way

NIHAO Numerical Investigation of a Hundred Astrophysical Objects

RAR Radial Acceleration Relation

SDSS Sloan Digital Sky Survey

SF Star Formation

SFR Star Formation Rate

SMBH Super Massive Black Hole

SMHMR Stellar Mass Halo Mass Relation

SN Supernova

SNII Type II Core Collapse Supernova

SPARC Spitzer Photometry and Accurate Rotation Curves

SPH Smoothed Particle Hydrodynamics

UV Ultraviolet

WMAP Wilkinson Microwave Anisotropy Probe

Chapter 1

Introduction

1.1 The Cosmological Context of Galaxy Formation

The modern picture of galaxy formation sits within the context of a Λ Cold Dark Matter (ΛCDM) cosmology (Rees & Ostriker, 1977; White & Rees, 1978; Blumenthal et al., 1984; Mo et al., 1998). Observations of the cosmic microwave background radiation, along with measurements of the subsequent cosmic expansion have revealed the composition of the universe to staggering precision. Ours is a universe which has a no curvature ($\Omega = 1$), and today has the majority of its mass-energy in dark energy Λ ($\Omega_\Lambda = 0.6911 \pm 0.0062$), and most of its matter in a collisionless form (dark matter) ($\Omega_m = 0.3089 \pm 0.0062$) (Planck Collaboration et al., 2016b). Roughly 5% of the matter-energy density of the universe exists as baryons ($\Omega_b = 0.048613 \pm 0.00031$). The composition of the universe, and the precise value of the mass-energy density for these components, sets the lifetime of the universe, how rapidly it expands (or contracts), and exactly determines the growth of large-scale structure. Within this structure is ultimately where galaxies will form. All of this began 13.799 ± 0.021 billion years ago (Planck Collaboration et al., 2016b), with the universe emerging from a state of high temperature and density, expanding to form what we see today. The primordial elemental abundances, with $\sim 4/5$ of the universe's baryons in hydrogen (the remainder in helium), were established just a few minutes after the big bang, during a brief period of "Big Bang Nucleosynthesis" (Alpher et al., 1948). The remaining heavier elements have been formed via stellar nucleosynthesis, through fusion in the cores of stars and in energetic processes that take place during supernovae (SN) (Wagoner et al., 1967). A small fraction of these metals form via the capture of high energy cosmic ray protons and α particles by carbon, nitrogen, or oxygen nucleii (Reeves, 1970). The chemical composition of the universe establishes the kinds of stars that form within galaxies and the rates at which gas within the interstellar medium (ISM) and beyond cools.

Much of what we know about the cosmology of our universe comes from observations of the first light to escape the universe's surface of last scattering as it became optically thin: the cosmic microwave background radiation (CMB). When the CMB was emitted, the baryons of the universe were in the form of a nearly isothermal ($\delta T/T \sim 10^{-5}$) gas of hydrogen and helium. Prior to a redshift of $z \approx 1100$, the universe had a high ionization fraction such that the mean free path for photons was short, making all of space effectively opaque. Once the universe became cool enough that hydrogen became fully neutral, the optical depth fell low enough that photons could free-stream, decoupled from baryons. We observe this ultraviolet light today, redshifted to microwaves with a temperature of 2.729 ± 0.004 K (Fixsen et al., 1996). When the power spectrum of this radiation is measured (Spergel et al., 2003), features in that spectrum can be used to determine the components of the universe (with some degeneracy that can be resolved via SN Ia and large scale structure measurements (Riess et al., 1998; Perlmutter et al., 1999; Beutler et al., 2011; Blake et al., 2011)). These features also reveal the spectrum of density perturbations that will eventually form galaxies (Press & Schechter, 1974; Peebles, 1980). The CMB is the single most important observational tool for understanding the cosmology of our universe.

The formation of structure within the universe began with the gravitational collapse of small, linear density perturbations seeded by quantum fluctuations amplified by inflation (Guth, 1981; Linde, 1982). These perturbations grow through gravitational collapse. Until $z \sim 1100$, only dark matter perturbations were able to grow. Prior to this, baryons were coupled to photons, causing density perturbations to oscillate as stable sound waves. This early collapse of matter meant that when decoupling occurred at $z \sim 1100$, baryons were able to collapse into the deeper potential wells grown out of dark matter density perturbations. These overdensities expand slower that the surrounding medium, as they experience a drag from their own self-gravity. Eventually, these regions stop expanding and begin collapsing at the turnaround time t_{turn}, and virialize at roughly 2 t_{turn} (Peebles, 1980). The first galaxies likely began to form around $z \sim 20 - 50$, with minimum sizes set by the baryonic physics of Silk damping and radiative cooling (Silk, 1968). Without the earlier growth of dark matter perturbations, structure formation would have occurred much later, and the number of galaxies and distribution of their masses would be different than those we see today (Davis et al., 1985).

The density perturbation spectrum describes the complete statistics of the Gaussian random field from which structure forms. Press & Schechter (1974) were able to show this produces a halo mass spectrum at a given time with a form that matched the functional form for the observed galaxy mass function (Schechter, 1976):

$$\frac{dn}{dM}(M,t) = \sqrt{\frac{2}{\pi}} \frac{\rho_0 \delta_c(t)}{M^2 \sigma(M)} \left| \frac{d \ln \sigma}{d \ln M} \right| \exp\left[-\frac{\delta_c^2(t)}{2\sigma^2(M)} \right] \tag{1.1}$$

In this equation, ρ_0 is the mean density of the universe, and $\delta_c(t)$ is the critical overdensity for collapse at a given time t. The mass variance spectrum, $\sigma^2(M)$ can be determined observationally using the CMB power spectrum (Fixsen et al., 1996; Spergel et al., 2003; Planck Collaboration et al., 2016a) and an assumption of a specific cosmology. This function gives an approximate distribution of masses for the dark matter halos in which galaxies will begin to form. As these halos collapse, non-linear gravitational tugs from their surroundings will impart torques on them (Barnes & Efstathiou, 1987), causing halos to have a distribution of angular momenta. High resolution N-body simulations have found that dark matter halos have both a universal density profile (Navarro et al., 1996; Merritt et al., 2006) as well as a universal angular momentum profile (Bullock et al., 2001). These dark matter halos serve as the environment in which the collapse of baryons and formation of stars take place, fed by accretion along large-scale filaments.

The collapse of baryons within halos will depend strongly on whether the post-virialized gas can cool radiatively (Rees & Ostriker, 1977). As gas accretes onto a halo with overdensity Δ it collisionally converts its potential energy into heat, with a characteristic virial temperature:

$$T_{virial} = \frac{2}{3}\frac{G\mu m_H}{k_B}\left(\frac{4\pi\rho_0\Delta M^2}{3}\right)^{1/3} \tag{1.2}$$

This means that more massive halos have larger virial temperatures, and, depending on the mode of radiative cooling (atomic cooling from primordial hydrogen, molecular hydrogen cooling, or cooling through metal lines), this may give cooling times shorter than the current age of the universe. These halos are the ones in which galaxy formation may begin, as their hot gaseous halos can collapse to form a central concentration where star formation can occur. In some halos, virial shocks may be unstable to cooling, allowing the direct collapse of cold gas onto the disc (Birnboim & Dekel, 2003).

As gas begins to cool within these halos, it will lose pressure support (by radiating away thermal energy), but *not* angular momentum. For large spiral galaxies, this means that the baryons, which typically carry the same specific angular momentum as the halo itself, will flatten to form an exponential disc as they cool (Fall & Efstathiou, 1980; Mo et al., 1998). A combination of heating and cooling processes will render this gas multiphase, containing both warm/hot ($T > 10^4$ K) and cold ($T \sim 10-100$ K) gas in quasistatic equilibrium (McKee & Ostriker, 1977). This multiphase state is highly dependent on both the metallicity and the local heating rates (which themselves can vary with redshift) (Field et al., 1969; Wolfire et al., 1995; Norman & Spaans, 1997). In the disc of the galaxy, this dense multiphase gas forms the ISM from which stars collapse and are born.

The formation of stars has a dramatic impact on the galaxy. As molecular clouds begin to construct O/B stars with masses $> 5\,\mathrm{M}_\odot$, these stars immediately begin to obliterate the clouds from which they form. A typical 10^5 $\mathrm{M}_\odot$ cluster will have an ionizing UV luminosity of $\sim 10^5$ $\mathrm{L}_\odot$ during its first few Myr of life. This UV flux ionizes the surrounding gas, heating it to $\sim 10^4$ K (Dale et al., 2005; Murray et al., 2011). Along with ionizing radiation, massive stars drive fast $v > 10^3\,\mathrm{km\,s^{-1}}$ stellar winds, further shocking and destroying the cold, dense gas which stars form from. By the time the most massive stars reach the end of their short lives, ~ 4 Myr later, they detonate as core-collapse supernovae not in dense ($n > 100\,\mathrm{cm^{-3}}$) clouds, but in their significantly more diffuse remnants (Rogers & Pittard, 2013). The longer cooling times this results in allow supernovae to expand through the ISM, driving turbulance (Ostriker et al., 2010) and filling most of the volume with hot, diffuse gas. Much of this hot gas is in fact able to leave the ISM, driven out as buoyant, high-entropy gas. These feedback-driven outflows remove gas from the disc, slowing the rate of star formation, and polluting the intergalactic medium with metals from stellar ejecta. In the most massive galaxies ($M > 10^{12}$ $\mathrm{M}_\odot$), these outflows can be driven by the accretion luminosity of the central supermassive black hole (SMBH). These active galactic nuclei (AGN) are observed in giant elliptical galaxies, and can be seen blowing hot bubbles within the intracluster medium of nearby galaxy clusters. Further discussion on feedback can be found in section 1.3.

These are of course all highly idealized, simple models for the broadest strokes of galaxy formation. Each of these halos will begin to undergo mergers and interactions (Navarro & White, 1993; Kauffmann et al., 1999; Cole et al., 2000) with each other that can strip stars and gas through tidal and ram pressure forces (Gunn & Gott, 1972; Dressler, 1980). Inside each of these halos, the process of disc collapse, the formation of a multiphase ISM, star formation, and feedback from those stars involves the complex, nonlinear interplay of radiation, hydrodynamics, magnetic fields, and gravity on length scales as much as 10^{11} times smaller than the virial radius. None of this physics is simple enough to be fully captured by analytic models. As figure

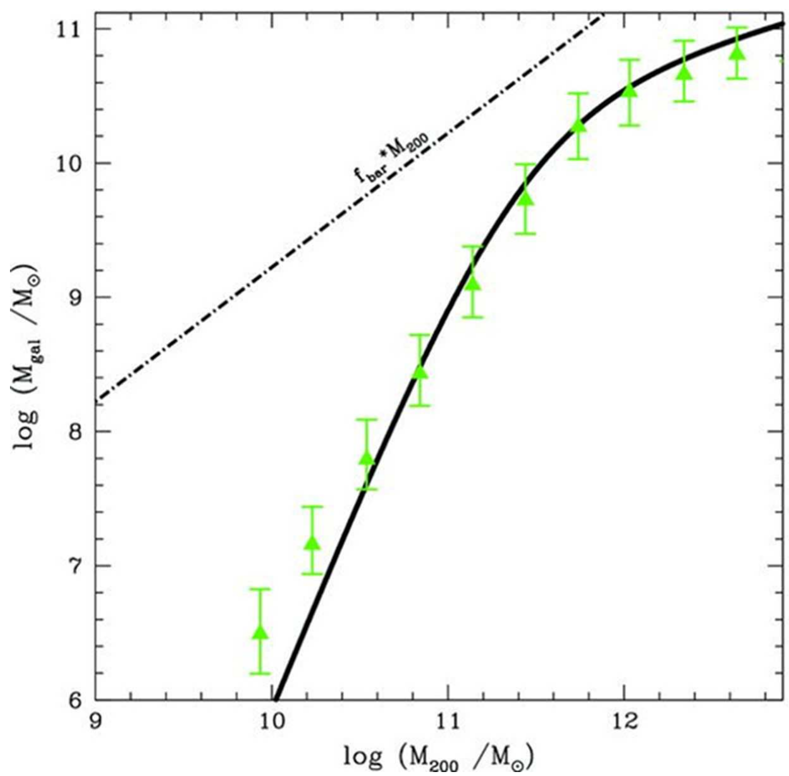

Figure 1.1: The observed mass function for galaxies in the nearby universe (derived using abundance matching for the solid line and semi-analytic modelling for the green points) does not match the mass function for dark matter halos given in equation 1, scaled by the baryon fraction (dashed line). This tells us that there are additional physical processes involved in the formation of galaxies within their dark matter halos. The most likely candidate for this is feedback from stars and black holes. Of particular interest is the peak in star formation efficiency near $M_{200} = 10^{12} M_{\odot}$. *Image credit: Adapted from figure 1 in Ferrero et al. (2012)*

.

1.1 shows, the observed mass function for galaxies does not match what would be expected from the total baryon budget for each halo, implying that at least some of these processes must change the galactic star formation efficiency as a function of halo mass, establishing the population of galaxies we see today. Numerical simulations have therefore become a keystone for galaxy formation research.

1.2 Numerical Simulations of Galaxies

N-body simulations of galaxies actually predate *digital* simulations of galaxies. Holmberg (1941) presented, as the author termed it, a “new integration procedure” that was the first attempt to simulate the evolution of a galaxy. By relying on the fact that light flux, just as gravity, scales as r^{-2}, Holmberg was able to construct a simulated galaxy disc out of light bulbs, and then using photocells to measure the flux at each bulb’s position, repositioned the bulbs using the forces “simulated” by the light-measuring process. This allowed him to painstakingly trace the tidal interactions of passing galaxies as they merged with each other.

In the intervening 75 years, we have migrated to much less labor-intensive simulations, relying on the constantly growing power of digital computers. As Gordon Moore first observed in 1965, the processing power of computers has been continuously growing at an exponential rate for more than half a century. This has meant that, even without advances in numerical methods and algorithm design, the ability of simulators today to model a system in high resolution is monumentally greater than just 10 years ago. Beyond the simple improvement of hardware, significant advances have been made in the underlying algorithms used in simulations, allowing the same hardware to perform larger, higher-resolution simulations than ever before. These algorithmic improvements have increased the speed and scalability of simulation codes even faster than improvements in hardware.

The earliest numerical simulations of galaxy formation focused on the effects of gravity alone. A classic example of this are the simulations presented in Toomre & Toomre (1972), which showed that the irregular structures seen in galaxies like NGC 4676 (“The Mice”) or NGC4038/4039 (“The Antennae Galaxies”) are the results of major mergers between two disc galaxies, as is clear from figure 1.2. These simulations used discs composed of a mere 120 test particles, and ignored the effects of self-gravity between these particles. Despite their crudeness, these simulations showed that the

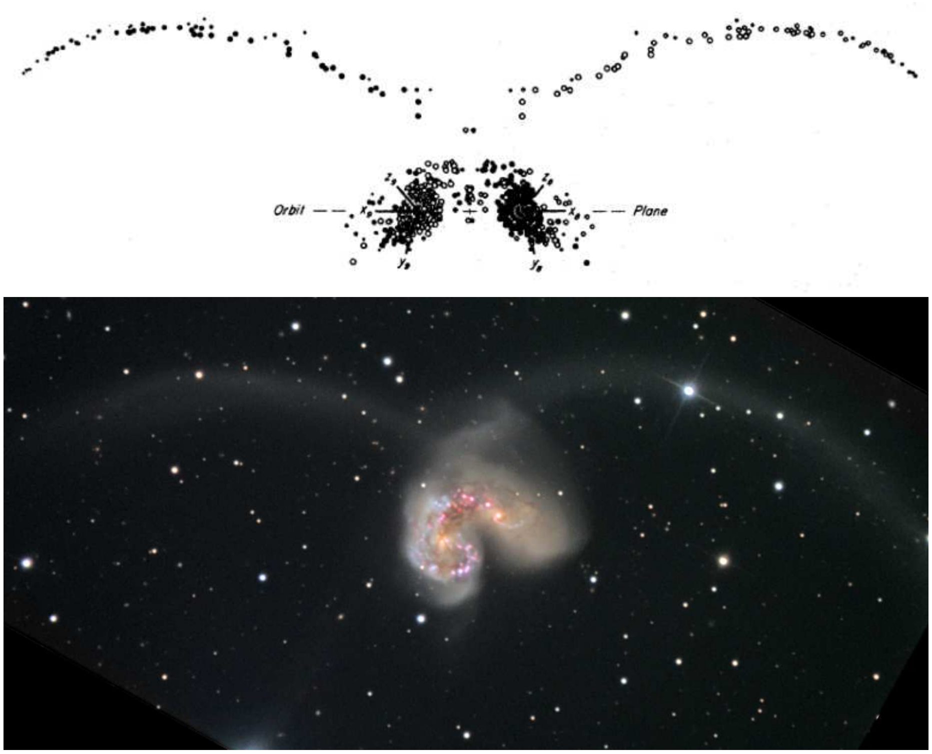

Figure 1.2: The simulations of Toomre & Toomre (1972) showed how the kinematics of galaxy mergers can produce the variety of tidal structures seen in objects like the Antennae galaxies. The top image shows the result of one of the Toomre & Toomre (1972) simulations. *Image credit: Adapted from figure 23 of Toomre & Toomre (1972)* The bottom image shows an observation of the actual object itself, the Antennae galaxies NGC 4038/4039. *Image credit: NOAO/AURA/NSF, B. Twardy, B. Twardy, and A. Block (NOAO)*

morphologies of galactic bridges and tails could be formed by the tidal interactions of two passing/merging galaxies. The IBM 360/95 that Toomre & Toomre (1972) (with an inflation-adjusted purchase price in the millions of dollars) used for their simulations was capable of 5.5 million instructions per second, roughly 0.2% the speed of a $35 Raspberry Pi 3 available today.

Modern galaxy simulations do far more than merely integrate the equations of motion for a few hundred test particles in a gravitational field. Today, state of the art simulations will track gravity (including self-gravity) for stars, gas, and dark matter (Aarseth & Fall, 1980; Stadel, 2001; Dehnen, 2002); evolve Euler's equations for the hydrodynamics of gaseous baryons (Wadsley et al., 2004; Teyssier, 2002; Bryan et al., 2014); include models for radiative cooling of gas that allow for cooling from both hydrogen and metal lines (Marri & White, 2003; Shen et al., 2010); form stars from dense gas (Katz, 1992; Agertz & Kravtsov, 2015); and include models for feedback from massive stars and black holes (Katz, 1992; Springel & Hernquist, 2003; Di Matteo et al., 2005). These feedback models have been the focus of much research in the past decade, as we shall discuss further in this work. Simulations also include treatments for radiative transfer (Gendelev & Krumholz, 2012; Krumholz & Thompson, 2013) and magneto-hydrodynamics (Girichidis et al., 2016) as well.

Numerical modeling of galaxies is a difficult problem, as it involves processes that take place over scales (both spatial and temporal) that span many orders of magnitude. This means that simulations will always be unable to resolve at least some fraction of the physics taking place within the galaxy. For this, carefully designed "sub-grid" models are required to include the macroscopic effects that unresolvable microscopic processes yield.

1.2.1 Gravity

Gravity is typically solved using algorithms designed to minimize the workload that would be needed for a direct summation of each particle or grid cell ($\mathcal{O}(N^2)$ for N grid cells/particles). This becomes intractable for larger numbers of resolution elements, as the workload will scale as the sixth power of the linear resolution (an order of magnitude better linear resolution will be 10^6 times more expensive!). In order to reduce these costs, algorithms have been developed that allow for more efficient gravitational force calculations. Tree-based methods (Barnes & Hut, 1986) reduce the computational cost of long-ranged (and thus less significant) force calculations by using space-partitioning trees. Short-range force calculations are done particle-by-particle, while long-range forces are calculated against larger tree cells, thus reducing the cost of calculating gravity to $\mathcal{O}(N \log N)$. Particle-Particle/Particle-Mesh (P^3M) methods (Couchman, 1991) produce similar scalings, but rather than using a spatial tree, rely on a spectral Fourier-based approach to calculate long-ranged interactions. Recently, the Fast Multipole Method (Greengard & Rokhlin, 1987) has been applied to the calculation of gravitational forces (Dehnen, 2002; Hahn et al., 2013) using a multipole expansion of Green's functions. This allows for extremely efficient gravity calculation, scaling linearly with particle number ($\mathcal{O}(N)$). This method allows it to now be possible to run N-body simulations with greater than 10^{12} particles (Potter et al., 2016).

1.2.2 Hydrodynamics

Hydrodynamical solvers usually come in one of two classes: Eulerian or Lagrangian. Eulerian methods discretize space into fixed-volume elements with fixed boundaries. By breaking a simulation volume into a grid of cells that each contains scalar and vector quantities, those quantities can be advected between cells according to the solver scheme. Eulerian schemes typically allow for higher-order solvers, lower intrinsic noise, and better resolved shocks (when at rest relative to the grid) (Teyssier, 2002; Stone et al., 2008; Bryan et al., 2014). They suffer from intrinsic mixing and diffusion that scales with the flow velocity relative to the grid, poor integration of circular orbits, and costly timestep limits (Agertz et al., 2007; Tasker et al., 2008). A variety of Eulerian solvers exist, ranging from the staggered mesh, high-order upwind & artificial viscosity scheme ZEUS, used in codes such as ENZO (Stone, 1999; Bryan et al., 2014), to the 2nd order Godunov method MUSCL used by RAMSES (van Leer, 1976; Teyssier, 2002), or the 3rd order PPM scheme of ATHENA (Stone et al., 2008). Lagrangian methods instead discretize mass, breaking the volume into discrete points, each of which moves at the fluid velocity to advect the quantities it contains, with smoothing functions used to interpolate values in-between particles; hence the name for the most common Lagrangian method, Smoothed Particle Hydrodynamics (SPH). Lagrangian methods couple easily to tree and particle-mesh codes for gravity calculation, are Galilean invariant, and intrinsically conserve mass, energy, and momentum (linear and angular) (Katz et al., 1996; Wadsley et al., 2004; Springel et al., 2005). The perfect conservation of angular momentum is critical for accurately tracking orbits. SPH methods typically use artificial viscosity to handle shocks, and as such have difficulty with capturing subsonic turbulence (Bauer & Springel, 2012). Recently, new methods have begun to extend the basic SPH method using higher order gradient estimates that are allowing accuracy on subsonic tests that rival the best Eulerian schemes (Springel, 2010; Hopkins, 2015; Valdarnini, 2016).

Modern galaxy simulations also now use a variety of strategies for judiciously applying computational power where it is most needed. Eulerian methods will commonly use Adaptive Mesh Refinement (AMR)(AMR) xies to increase resolution in regions of interest (typically where gas is densest). Lagrangian methods automatically do this, as a denser region definitionally must contain more fluid elements.

1.2.3 Designing Simulations

Beyond the choice of algorithms, the construction of appropriate inital conditions is also important. To study large populations of galaxies (along with large-scale structure) large-volume cosmological boxes with volumes $\gtrsim 10^6$ Mpc^3, and with spatial resolutions $\sim$ kpc are used (for example, the *Illustris* simulations have a softening length of 1.4 kpc (Vogelsberger et al., 2014)). Studying how individual galaxies form is typically done with cosmological zoom simulations, where a comparatively cheap dark-matter only simulation is first run to select a region of interest, which is then resimulated with higher resolution and baryonic physics included (Navarro & White, 1993). Zoom-in simulations can typically achieve an order of magnitude or better resolution than full cosmological boxes. A number of groups today are using these zoom-in simulations to study the impact of feedback processes over cosmic time (Stinson et al., 2013; Hopkins et al., 2014; Agertz & Kravtsov, 2015). Isolated galaxy disc simulations use constructed disc profiles containing gas and stars, embedded within a dark halo. These cannot show how galaxies form in a cosmological environment, but can be run with $\sim$ pc resolution to study closely how internal processes within a galaxy take place (Hopkins et al., 2011; Benincasa et al., 2016). Details of these internal processes are discussed in section 1.3.

The earliest attempt to track the formation of a galaxy in a cosmological context with the effects of star formation and feedback included was by Katz (1992). This simulation used the Lagrangian TREESPH (Hernquist & Katz, 1989) to evolve a volume of gas and dark matter from an initial linear perturbation, including small-scale power derived from CDM predictions (Zel'dovich, 1970; Peebles, 1982). Gas was allowed to cool radiatively using rates calculated for primordial gas. This study introduced a model for star formation that is still the standard for most simulations of galaxy formation. Observations (Kennicutt, 1998) have suggested that the star formation rate is a power law of the gas density: $\dot{\Sigma}_* \propto \Sigma_{gas}^{\alpha}$, with $\alpha = 1 - 2$. If it is assumed that gas collapses to form stars in some multiple c_* of its freefall time (Schmidt, 1959), t_{ff}, a simple 3-dimensional star formation model, can be built with the form:

$$\dot{\rho}_* = \frac{c_* \rho_{gas}}{t_{ff}} = c_* \sqrt{\frac{\rho_{gas}^3}{4\pi G}} \tag{1.3}$$

Katz (1992) used a c_* parameter of 0.1, which is within the range of what is typically used in simulations today ($1-100\%$). On top of the model for star formation, feedback was included without the use of any significant subgrid model: 10^{51} erg/SN worth of energy was injected back into the ISM by smoothing it over a number of resolution elements. One of the key findings of Katz (1992) was that the vast majority of SN energy was radiated away, making them very ineffective at regulating star formation within the galaxy. In the end, Katz (1992) found that the peak star formation in the simulated galaxy was nearly 10 times greater than in observed galaxies. Thacker & Couchman (2000) later showed that the smoothing of energy used by Katz (1992) resulted in a large overestimation of the cooling rates in feedback-heated gas. Since then, much work has gone into developing models for feedback that address the issue of overcooling that was present in these earlier simulations. These efforts will be described in detail in the next section.

1.3 The Importance of Feedback

Evidence has been building for decades that galaxy & star formation is not a one-way process of gravitational collapse. A number of internal processes can release a tremendous amount of energy back into the ISM of the galaxy, stirring or even ejecting that gas. Analytic calculations that omit feedback processes found that gas should rapidly collapse into the smallest halos that can cool radiatively (halos with a virial temperature of $\sim 10^4$ K, or a mass of $\sim 10^8$ $\mathrm{M}_\odot$). This leads to an overproduction of stars in small galaxies at high redshift (the "cooling catastrophe") (Cole et al., 2001; Benson et al., 2003). The observational signatures of feedback are abundant. Lyman α forest observations probing the intergalactic medium (IGM) have found that the

Figure 1.3: The evidence for feedback is no clearer than here in the Cigar Galaxy, M82. The Hubble Space Telescope reveals massive outflows of hot ionized gas through the red $H\alpha$ emission as gas is blasted out of the galaxy in a bipolar flow. *Image credit: NASA, ESA and the Hubble Heritage Team STScI/AURA*

IGM is polluted with metal ions at great distances from any galaxies (Sargent et al., 1988; Songaila & Cowie, 1996; Davé et al., 1998). These metals must have been ejected by galactic outflows from the ISM of galaxies where they formed. Figure 1.3 shows a composite image of the dwarf starburst M82, where fast, massive outflows have been seen leaving the ISM. These outflows have been observed as a ubiquitous feature of starburst galaxies and quasar host galaxies (Veilleux et al., 2005; Werk et al., 2014). Numerical models have also pointed towards feedback as an essential ingredient in forming both realistic galaxies and the structures within them. Simulated galaxies develop unrealistically compact morphologies without feedback (Stinson et al., 2006). Inside of the galaxy, simulations of individual molecular clouds have star formation rates an order of magnitude too high (Agertz et al., 2013) when feedback is omitted. Clearly, if we wish to accurately simulate galaxies, we must also accurately model the feedback processes that shape those galaxies.

The two primary sources of feedback energy are massive stars and SMBHs. Massive stars ($M > 5M_{\odot}$) experience short, violent lives. Prior to their death, they will drive fast $v > 1000$ km/s stellar winds (Weaver et al., 1977), and ionize their surrounding gas with UV radiation (Krumholz & Matzner, 2009). At the end of their lives, $4 - 30$ Myr later, these stars die in energetic core-collapse SN, liberating $\sim 10^{51}$ erg (Wilson, 1985; Bethe, 1990). Figure 1.4 shows the total budget of available energy liberated by a population of stars with a standard Chabrier (2003) IMF. The total energy released by a population of stars with solar metallicity is $\sim 2 \times 10^{51}$ erg/M$_{\odot}$. Most of this energy is released as photons, over the lifetime of each star. These will both couple weakly with the ISM, depositing little energy, and only heat gas to a relatively modest temperature, much cooler than the virial temperature for galaxies like our own. While stellar winds from a cluster will have comparable luminosity to supernovae, two factors limit the effectiveness of these winds at driving galaxy-scale outflows. First, because these stellar winds are produced early, they couple to the dense environment of the cluster's natal cloud, resulting in orders of magnitude shorter cooling times for the hot bubbles they drive. Second, the vast majority of the energy liberated in stellar winds comes from the most massive stars, which die within 4 Myr, giving stellar winds a total energy budget of 10% of the supernovae budget Leitherer et al. (1999). This means that supernovae, despite only contributing $\sim 1\%$ of the total energy released by a stellar population, may have the greatest impact on galactic scales. This energy imparts heat and momentum to the surrounding ISM,

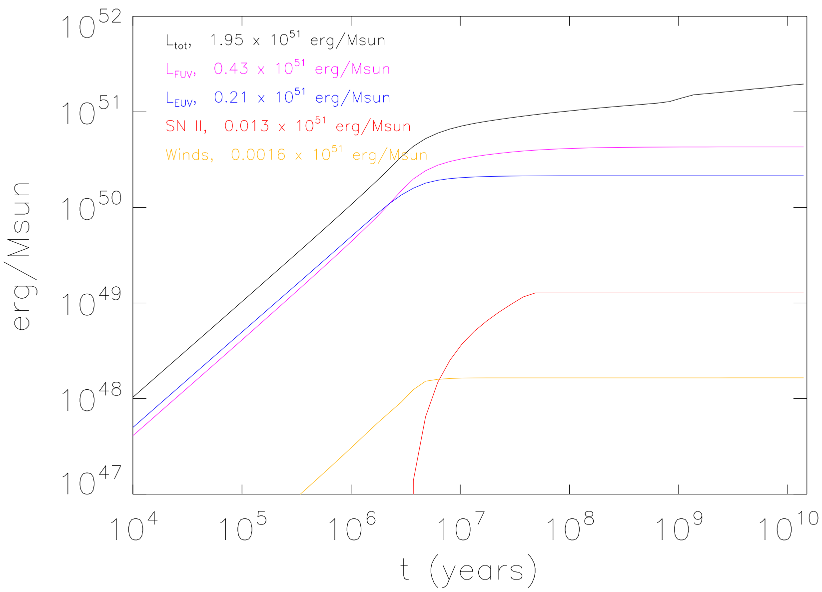

Figure 1.4: Most of the energy released by a stellar population comes from the luminosity of the stars within that population. Despite this, because supernovae couple more easily to the ISM, it is believed they have the greatest effect on galactic scales. The data shown here was produced with STARBURST99 (Leitherer et al., 1999)

and can accelerate cosmic rays in the shocks that result (Bell, 1978). In galaxies with actively growing SMBHs, the accretion disc that forms as gas funnels into the black hole can reach temperatures exceeding 10^9 K through viscous heating (Antonucci, 1993). This makes these accretion discs some of the most luminous objects in the universe, and can heat the gas that surrounds the galaxy to choke off the accretion of gas onto the galaxy, shutting off star formation.

The coupling of feedback energy to the ISM is what determines the effectiveness of that feedback. In the lowest-mass galaxies, UV photoheating may be the primary regulator of star formation (Efstathiou, 1992). However, UV radiation has characteristic temperatures too low to drive galactic winds. Large HII regions, such as 30 Doradus, have observed expansion rates of only 25 km/s (Chu & Kennicutt, 1994), far below the velocities needed to drive galaxy-scale outflows. Radiation pressure on dust grains has been suggested as a driving mechanism for outflows (Murray et al., 2011). Simulations that see a large effect from radiation-driven galactic winds have thus far relied on major approximations (Roškar et al., 2014; Agertz & Kravtsov, 2015) and questionably large infrared optical depths (Hopkins et al., 2014). Without high optical depths and multiple scattering, UV photons will be reprocessed to IR radiation that escapes before imparting significant energy or momentum to the surrounding gas (Dale et al., 2005; Walch et al., 2012; Krumholz & Thompson, 2013).

On top of releasing just 10% of the energy released by supernovae, stellar winds are active during the early stages of a massive star's life. Simulations of molecular clouds with feedback from star clusters (Gendelev & Krumholz, 2012; Rogers & Pittard, 2013) have found that most stellar wind energy is expended disrupting the molecular clouds the clusters live in. While these winds (along with radiation pressure and UV-heated gas) do not significantly escape the cluster, the channels they open within the cloud allow a large fraction of SN energy to escape the dense molecular environment. The energy from winds and radiation are expended in disrupting the cloud. Thus, for galaxy-scale simulations that do not resolve the internal structure of individual molecular clouds, the effects of UV radiation and stellar winds can be safely omitted.

On the galactic scale, feedback regulates star formation in two primary ways. Energy and momentum deposited into the ISM can heat and disrupt the cool clouds of gas which form stars (Rogers & Pittard, 2013), and increase the ISM scale height to limit the formation of cool clouds out of the warm ISM (Ostriker et al., 2010; Benincasa et al., 2016). If that feedback is vigorous enough, gas can actually be ejected from the disc into the circumgalactic medium (CGM) (Larson, 1974; Heckman et al., 1987; Hopkins et al., 2012). Even if this material is still bound to the halo, it can take $\sim$ Gyr to return to the ISM. This limits star formation by simply removing the fuel for the process. These outflows are needed to explain observations of low star formation efficiencies in massive galaxies (Behroozi et al., 2013; Moster et al., 2013), observations of outflowing gas (Lynds & Sandage, 1963; Heckman et al., 1987), a metal-polluted intergalactic medium (Shen et al., 2010), and the low bulge fraction in star forming galaxies (Brook et al., 2012). In order to see how the local deposition of feedback energy drives these winds, simulations with realistic models for hot stellar feedback are required.

1.3.1 Numerical Challenges for Hot Feedback

The greatest difficulty with including the effects of feedback in simulations of galaxy evolution is the combination of extreme gradients of temperature, density, and velocity all in a relatively small mass/volume. Without overwhelmingly high resolution, hot feedback gas will be numerically mixed with cold ISM, often resulting in gas with relatively high density and temperatures of $\sim 10^5$ K, where radiative cooling times are extremely short. This results in feedback energy being completely lost due to radiative cooling, as was first seen by Katz (1992). Indeed, as Thacker & Couchman (2000) showed, how feedback energy is deposited into the ISM has a huge impact on whether that feedback has any effect. This problem has been tackled using a few different strategies.

Since overcooling is the problem, many models have attacked this directly by either temporarily disabling cooling (Thacker & Couchman, 2000; Stinson et al., 2006) or depositing feedback energy into a second, nonthermal energy component (Agertz et al., 2013). While this does limit radiative losses, it produces gas that exists in an unphysical region of the $\rho - T$ phase diagram. This gas may lack the high temperatures and velocities required to actually escape the disc. It also has the potential to introduce an *undercooling* problem as resolution becomes higher and feedback-heated gas becomes resolvable. Alternatively, energy may be injected not as heat, but as momentum, which naturally does not cool (Navarro & White, 1993; Mihos & Hernquist, 1994; Scannapieco et al., 2006; Dalla Vecchia & Schaye, 2008; Dubois & Teyssier, 2008). Unfortunately, this adds the additional complexity of momentum cancellation (how to treat neighbouring stars/clusters, where two stars are depositing momentum with opposing directions), and if this momentum results in strong shocks, these shocks will convert the momentum back into thermal energy that can radiate away the very energy the model is designed to preserve (Durier & Dalla Vecchia, 2012). This often means kinetic/momentum feedback models must be combined with hydrodynamic decoupling that renders feedback-heated gas into a form that does not interact with the surrounding ISM (Springel & Hernquist, 2003; Vogelsberger et al., 2013). Naturally, this makes outflow properties strongly influenced by numerical choices (Dalla Vecchia & Schaye, 2008). A third choice is to stochastically deposit feedback energy only when enough energy is available to produce gas temperatures high enough for cooling times to be short (Dalla Vecchia & Schaye, 2012; Crain et al., 2015). In these models, SN events are effectively grouped together, somewhat decoupling feedback spatially from star formation. The choice of temperature to heat gas to is a purely numerical parameter, and can dramatically change the effectiveness of these models. Finally, some (Springel & Hernquist, 2003; Murante et al., 2015) attempt to directly address the unphysical numerical mixing of hot and cold gas by separating the two phases and tracking each component separately. This completely solves the overcooling problem, and allows the two components to cool radiatively. Unfortunately, it also means that cold star-forming gas is permanently coupled to hot feedback-heated gas. This prevents the simulation of a resolved multiphase ISM, and effectively makes the cold/warm ISM an anchor holding down potential hot outflows. This means these multiphase models have to be coupled with parameterized models to capture outflows (Springel & Hernquist, 2003). Often, these simple models simply choose a fraction of feedback energy to be deposited as kinetic "kicks" to some gas particles. Like other kinetic feedback models, this is frequently combined with hydrodynamical decouplings (Vogelsberger et al., 2013).

All of these models attempt to solve the problem of overcooling with unphysical approximations: disabled cooling, hydrodynamic decoupling, stochastic deposition of feedback energy, and imposed multiphase ISM models. These choices make it difficult to understand which details of simulated galaxy evolution are a result of these numerical free parameters, as opposed to the actual physics of self-regulated star formation and SN-driven outflows. What is needed is a model that captures the effects of feedback while matching as closely as possible the actual physical processes involved below the resolution scale. Simulations that rely on complex, numerically-motivated subgrid models are devoid of serious predictive power. When the results obtained depend heavily of the tuning of multiple free parameters, those results can at best probe one point in the space of the possible, rather than hew away at that space to discover the region of the probable, and ultimately, the truth.

1.3.2 Superbubbles: The Natural Scale for Feedback

The formation of massive stars takes place mostly in clusters of 10^4 or more stars. This means that the SN of these stars can be treated not as individual dumps of 10^{51} erg/SN, but instead as a luminosity of $10^{34}\ \frac{\mathrm{erg}}{\mathrm{s \cdot M_\odot}}$. This allows us to use stellar wind models like those of Weaver et al. (1977) to study the evolution of superbubbles driven by hot stellar feedback processes, like SN or stellar winds. Each individual SN's ejecta thermalizes in a small region within the center of the bubble, and the resulting hot gas drives a shock that sweeps up the surrounding ISM. In a short time, the swept-up ISM can radiatively cool, efficiently resulting in a thin, cold shell surrounding a hot, diffuse bubble.

The structure and evolution of superbubbles have been the subject of a great deal of analytic study. Castor et al. (1975) found that the time evolution of superbubbles has a similarity solution, similar to the Sedov (1959) adiabatic blast wave solution:

$$R(t) = 27 n_0^{-1/5} L_{36}^{1/5} t_6^{3/5} \text{ pc} \tag{1.4}$$

$$V(t) = 16 n_0^{-1/5} L_{36}^{1/5} t_6^{-2/5} \text{ km/s} \tag{1.5}$$

n_0 is the ambient density in cm^{-3}, L_{36} is the luminosity of the star cluster in 10^{36} erg/s, and t_6 is the time in 10^6 yr. The evolution of hot mass in the bubble, and the effects of cooling in the swept-up shell, were examined in Weaver et al. (1977). The Weaver et al. (1977) results were extended to clustered SN by Mac Low & McCray (1988). They calculated that the typical cooling time for the hot bubble was ~ 15 Myr, with a weak dependence on the total luminosity and ambient density. Before significant cooling can occur in the hot interior, $\sim 35\%$ of the total feedback luminosity is lost to cooling of the swept-up shell, which cools in $\sim 10^4$ yr. This means that, rather than the $1 - 10\%$ of energy preserved from a single supernova blast (Chevalier, 1974), $\sim 65\%$ of the initial energy budget is retained in the kinetic energy of the cold shell and thermal energy of the hot interior. Mac Low & McCray (1988) also demonstrated that, as superbubbles do not have surface tension, they are not depressurized by cold clouds, and instead simply deform around them while continuing to expand. Silich et al. (1996) studied the effects of an ISM permeated with cold clumps in greater detail, finding that the general behaviour discussed in Mac Low & McCray (1988) held even in the case of an inhomogeneous ISM. Even with 50% of the ISM mass trapped in cold clouds (which penetrate the cold shell of the superbubble), the total hot mass within the superbubble will only vary by $\sim 20\%$.

A key insight in these studies was that hot bubbles would evaporate their cold shell through thermal conduction. In a hot ionized plasma, electrons are able to penetrate temperature gradients and deposit energy within cooler material. This produces a pressure gradient that establishes a mass flux against the temperature gradient, evaporating the cold shell into the hot bubble. This evaporation means that a hot bubble with temperature T and radius R gains mass at a rate of:

$$\frac{\mathrm{d}M_b}{\mathrm{d}t} = \frac{16\pi\mu}{25 k_B} C T^{5/2} R \tag{1.6}$$

Where C is the Spitzer conduction coefficient, $C = 6 \times 10^{-7}$ erg s^{-1} cm^{-1} K$^{7/2}$, and

μ is the mean molecular weight of the gas in the bubble. As the cold, evaporated material acts to cool the hot bubble, this makes the bubble's interior temperature self-regulating: higher temperatures give higher mass flux, cooling the bubble. This acts to push interior bubble temperatures to $10^6 - 10^7$ K.

Dalla Vecchia & Schaye (2012) showed that the temperature of feedback-heated gas can ultimately determine its effectiveness in driving outflows and regulating star formation, even with constant feedback energy. The self-regulating temperature of superbubbles provides the natural mechanism for setting this temperature: thermal evaporation. By including the effects of thermal evaporation between unresolved hot bubbles and the surrounding cool ISM, feedback energy can be deposited into the correct amount of ISM mass, giving realistic temperatures, densities, and cooling times for feedback-heated gas. This superbubble feedback model is described in detail, and applied to the problem of Milky Way-like galaxy formation in the chapters that follow.

1.4 This Work and Organization of Chapters

In this thesis, I present a new sub-grid model for the feedback from massive stars. I use this new model to study the importance of well-modelled SN feedback in the cosmological evolution of Milky Way-like galaxies, and how that feedback can drive the outflows that are key to forming physically realistic galaxies. I then turn to the question of SN-regulation at the peak of star formation efficiency, and examine whether the turnover in this efficiency seen by studies such as Behroozi et al. (2013) and Moster et al. (2013) can be attributed to SN feedback alone. Finally, I apply the simulations generated during these investigations to see whether SN-regulated galaxies formed in a ΛCDM cosmological context can match observed scaling relations of nearby disc galaxies.

Chapter 2 presents the new superbubble feedback model, and describes the implementation of this model in the simulation code GASOLINE2 (Wadsley et al. 2016, submitted). I show a series of tests that demonstrate the model is robust to resolution changes, insensitive to magnetic field strength (which affects conduction rates), and able to handle cases involving unresolved ISM structure. Finally, I show that simulations of isolated dwarf and Milky Way-like disc galaxies regulate their star formation and drive efficient galactic outflows with this new feedback model.

Chapter 3 applies the feedback model described in chapter 2 to a cosmological simulation of a Milky Way like galaxy. This allows us to see how galaxies like the Milky Way assemble themselves by regulating the flow of gas into the disc, ejecting material to prevent the formation of a central stellar bulge and slow the formation of stars. We compare this to the same simulation run with the simpler Stinson et al. (2006) feedback model to reproduce the results of Stinson et al. (2010), which used the same initial conditions as this study. We use our results to study how this new, physically motivated feedback model changes prior assumptions about the effectiveness of SN feedback. We also examine how SN-driven outflows remove the fuel for star formation and bulge growth to produce a realistic, bulgeless disc galaxy.

Chapter 4 extends the results presented in chapter 3 by simulating an additional 17 cosmological galaxies, reproducing the McMaster Unbiased Galaxy Simulations (MUGS) presented in Stinson et al. (2010) with updated hydrodynamics and the new feedback model described in chapter 2. This MUGS2 sample spans the peak of the star formation efficiency found by abundance matching studies like Moster et al. (2013), and using it we are able to show that SN feedback is unable to regulate galaxies more massive than the peak halo mass of 10^{12} $M_{\odot}$. By analyzing the outflow properties of these galaxies, we are able to determine a global relation between the halo mass (or disc mass) and the outflow mass loadings. We examine how the mass loading of galactic outflows is set through evaporation, and how the effective temperature determines the effectiveness of these outflows at regulating the formation of the galaxies in the MUGS2 sample.

Chapter 5 uses the sample of galaxies developed in the previous chapter to test whether recent observational results presented in McGaugh et al. (2016) are consistent with ΛCDM. The radial acceleration relation (RAR) seen in the SPARC sample (Lelli et al., 2016) of observed rotationally supported galaxies shows that the accelerations within these galaxies are tightly correlated with the accelerations due to baryons alone. We show, using the sample of galaxies generated in chapter 4, that this relation simply falls out of the dissipative collapse of baryons in a collisionless dark matter halo. We also show that this result is independent of stellar feedback. Despite the insensitivity to feedback processes at $z = 0$, we show that feedback does result in evolution of the RAR with redshift, and predict that a different RAR would be observed if a similar study to Lelli et al. (2016) were done for high-redshift galaxies.

Finally, in chapter 6 we conclude with a discussion of how each of these results together improve our understanding of SN-regulated star formation in the formation of disc galaxies. We discuss how the results presented here improve the understanding developed in past research, and its impact on the direction of subsequent research in galaxy evolution theory. We conclude with a discussion of the future directions that this research points to, and a number of open questions raised by this research.

Bibliography

Aarseth S. J., Fall S. M., 1980, ApJ, 236, 43

Agertz O., Kravtsov A. V., 2015, ApJ, 804, 18

Agertz O., et al., 2007, MNRAS, 380, 963

Agertz O., Kravtsov A. V., Leitner S. N., Gnedin N. Y., 2013, ApJ, 770, 25

Alpher R. A., Herman R., Gamow G. A., 1948, Physical Review, 74, 1198

Antonucci R., 1993, ARAA, 31, 473

Barnes J., Efstathiou G., 1987, ApJ, 319, 575

Barnes J., Hut P., 1986, Nature, 324, 446

Bauer A., Springel V., 2012, MNRAS, 423, 2558

Behroozi P. S., Wechsler R. H., Conroy C., 2013, ApJ, 770, 57

Bell A. R., 1978, MNRAS, 182, 147

Benincasa S. M., Wadsley J., Couchman H. M. P., Keller B. W., 2016, MNRAS, 462, 3053

Benson A. J., Bower R. G., Frenk C. S., Lacey C. G., Baugh C. M., Cole S., 2003, ApJ, 599, 38

Bethe H. A., 1990, Reviews of Modern Physics, 62, 801

Beutler F., et al., 2011, MNRAS, 416, 3017

Birnboim Y., Dekel A., 2003, MNRAS, 345, 349

Blake C., et al., 2011, MNRAS, 418, 1707

Blumenthal G. R., Faber S. M., Primack J. R., Rees M. J., 1984, Nature, 311, 517

Brook C. B., Stinson G., Gibson B. K., Roškar R., Wadsley J., Quinn T., 2012, MNRAS, 419, 771

Bryan G. L., et al., 2014, ApJS, 211, 19

Bullock J. S., Dekel A., Kolatt T. S., Kravtsov A. V., Klypin A. A., Porciani C., Primack J. R., 2001, ApJ, 555, 240

Castor J., McCray R., Weaver R., 1975, ApJ, 200, L107

Chabrier G., 2003, PASP, 115, 763

Chevalier R. A., 1974, ApJ, 188, 501

Chu Y.-H., Kennicutt Jr. R. C., 1994, ApJ, 425, 720

Cole S., Lacey C. G., Baugh C. M., Frenk C. S., 2000, MNRAS, 319, 168

Cole S., et al., 2001, MNRAS, 326, 255

Couchman H. M. P., 1991, ApJ, 368, L23

Crain R. A., et al., 2015, MNRAS, 450, 1937

Dale J. E., Bonnell I. A., Clarke C. J., Bate M. R., 2005, MNRAS, 358, 291

Dalla Vecchia C., Schaye J., 2008, MNRAS, 387, 1431

Dalla Vecchia C., Schaye J., 2012, MNRAS, 426, 140

Davé R., Hellsten U., Hernquist L., Katz N., Weinberg D. H., 1998, ApJ, 509, 661

Davis M., Efstathiou G., Frenk C. S., White S. D. M., 1985, ApJ, 292, 371

Dehnen W., 2002, Journal of Computational Physics, 179, 27

Di Matteo T., Springel V., Hernquist L., 2005, Nature, 433, 604

Dressler A., 1980, ApJ, 236, 351

Dubois Y., Teyssier R., 2008, A&A, 477, 79

Durier F., Dalla Vecchia C., 2012, MNRAS, 419, 465

Efstathiou G., 1992, MNRAS, 256, 43P

Fall S. M., Efstathiou G., 1980, MNRAS, 193, 189

Ferrero I., Abadi M. G., Navarro J. F., Sales L. V., Gurovich S., 2012, MNRAS, 425, 2817

Field G. B., Goldsmith D. W., Habing H. J., 1969, ApJ, 155, L149

Fixsen D. J., Cheng E. S., Gales J. M., Mather J. C., Shafer R. A., Wright E. L., 1996, ApJ, 473, 576

Gendelev L., Krumholz M. R., 2012, ApJ, 745, 158

Girichidis P., et al., 2016, ApJ, 816, L19

Greengard L., Rokhlin V., 1987, Journal of Computational Physics, 73, 325

Gunn J. E., Gott III J. R., 1972, ApJ, 176, 1

Guth A. H., 1981, Phys. Rev. D, 23, 347

Hahn O., Abel T., Kaehler R., 2013, MNRAS, 434, 1171

Heckman T. M., Armus L., Miley G. K., 1987, AJ, 93, 276

Hernquist L., Katz N., 1989, ApJS, 70, 419

Holmberg E., 1941, ApJ, 94, 385

Hopkins P. F., 2015, MNRAS, 450, 53

Hopkins P. F., Quataert E., Murray N., 2011, MNRAS, 417, 950

Hopkins P. F., Quataert E., Murray N., 2012, MNRAS, 421, 3522

Hopkins P. F., Kereš D., Oñorbe J., Faucher-Giguère C.-A., Quataert E., Murray N., Bullock J. S., 2014, MNRAS, 445, 581

Katz N., 1992, ApJ, 391, 502

Katz N., Weinberg D. H., Hernquist L., 1996, ApJS, 105, 19

Kauffmann G., Colberg J. M., Diaferio A., White S. D. M., 1999, MNRAS, 303, 188

Kennicutt Jr. R. C., 1998, ApJ, 498, 541

Krumholz M. R., Matzner C. D., 2009, ApJ, 703, 1352

Krumholz M. R., Thompson T. A., 2013, MNRAS, 434, 2329

Larson R. B., 1974, MNRAS, 169, 229

Leitherer C., et al., 1999, ApJS, 123, 3

Lelli F., McGaugh S. S., Schombert J. M., 2016, preprint, (arXiv:1606.09251)

Linde A. D., 1982, Physics Letters B, 108, 389

Lynds C. R., Sandage A. R., 1963, ApJ, 137, 1005

Mac Low M.-M., McCray R., 1988, ApJ, 324, 776

Marri S., White S. D. M., 2003, MNRAS, 345, 561

McGaugh S., Lelli F., Schombert J., 2016, preprint, (arXiv:1609.05917)

McKee C. F., Ostriker J. P., 1977, ApJ, 218, 148

Merritt D., Graham A. W., Moore B., Diemand J., Terzić B., 2006, AJ, 132, 2685

Mihos J. C., Hernquist L., 1994, ApJ, 425, L13

Mo H. J., Mao S., White S. D. M., 1998, MNRAS, 295, 319

Moster B. P., Naab T., White S. D. M., 2013, MNRAS, 428, 3121

Murante G., Monaco P., Borgani S., Tornatore L., Dolag K., Goz D., 2015, MNRAS, 447, 178

Murray N., Ménard B., Thompson T. A., 2011, ApJ, 735, 66

Navarro J. F., White S. D. M., 1993, MNRAS, 265, 271

Navarro J. F., Frenk C. S., White S. D. M., 1996, ApJ, 462, 563

Norman C. A., Spaans M., 1997, ApJ, 480, 145

Ostriker E. C., McKee C. F., Leroy A. K., 2010, ApJ, 721, 975

Peebles P. J. E., 1980, The large-scale structure of the universe

Peebles P. J. E., 1982, ApJ, 263, L1

Perlmutter S., et al., 1999, ApJ, 517, 565

Planck Collaboration et al., 2016a, A&A, 594, A11

Planck Collaboration et al., 2016b, A&A, 594, A13

Potter D., Stadel J., Teyssier R., 2016, preprint, (arXiv:1609.08621)

Press W. H., Schechter P., 1974, ApJ, 187, 425

Rees M. J., Ostriker J. P., 1977, MNRAS, 179, 541

Reeves H., 1970, Nature, 226, 727

Riess A. G., et al., 1998, AJ, 116, 1009

Rogers H., Pittard J. M., 2013, MNRAS, 431, 1337

Roškar R., Teyssier R., Agertz O., Wetzstein M., Moore B., 2014, MNRAS, 444, 2837

Sargent W. L. W., Boksenberg A., Steidel C. C., 1988, ApJS, 68, 539

Scannapieco C., Tissera P. B., White S. D. M., Springel V., 2006, MNRAS, 371, 1125

Schechter P., 1976, ApJ, 203, 297

Schmidt M., 1959, ApJ, 129, 243

Sedov L. I., 1959, Similarity and Dimensional Methods in Mechanics

Shen S., Wadsley J., Stinson G., 2010, MNRAS, 407, 1581

Silich S. A., Franco J., Palous J., Tenorio-Tagle G., 1996, ApJ, 468, 722

Silk J., 1968, ApJ, 151, 459

Songaila A., Cowie L. L., 1996, AJ, 112, 335

Spergel D. N., et al., 2003, ApJS, 148, 175

Springel V., 2010, MNRAS, 401, 791

Springel V., Hernquist L., 2003, MNRAS, 339, 289

Springel V., Di Matteo T., Hernquist L., 2005, MNRAS, 361, 776

Stadel J. G., 2001, PhD thesis, UNIVERSITY OF WASHINGTON

Stinson G., Seth A., Katz N., Wadsley J., Governato F., Quinn T., 2006, MNRAS, 373, 1074

Stinson G. S., Bailin J., Couchman H., Wadsley J., Shen S., Nickerson S., Brook C., Quinn T., 2010, MNRAS, 408, 812

Stinson G. S., Brook C., Macciò A. V., Wadsley J., Quinn T. R., Couchman H. M. P., 2013, MNRAS, 428, 129

Stone J. M., 1999, Journal of Computational and Applied Mathematics, 109, 261

Stone J. M., Gardiner T. A., Teuben P., Hawley J. F., Simon J. B., 2008, ApJS, 178, 137

Tasker E. J., Brunino R., Mitchell N. L., Michielsen D., Hopton S., Pearce F. R., Bryan G. L., Theuns T., 2008, MNRAS, 390, 1267

Teyssier R., 2002, A&A, 385, 337

Thacker R. J., Couchman H. M. P., 2000, ApJ, 545, 728

Toomre A., Toomre J., 1972, ApJ, 178, 623

Valdarnini R., 2016, preprint, (arXiv:1608.08361)

Veilleux S., Cecil G., Bland-Hawthorn J., 2005, ARAA, 43, 769

Vogelsberger M., Genel S., Sijacki D., Torrey P., Springel V., Hernquist L., 2013, MNRAS, 436, 3031

Vogelsberger M., et al., 2014, MNRAS, 444, 1518

Wadsley J. W., Stadel J., Quinn T., 2004, New Astronomy, 9, 137

Wagoner R. V., Fowler W. A., Hoyle F., 1967, ApJ, 148, 3

Walch S. K., Whitworth A. P., Bisbas T., Wünsch R., Hubber D., 2012, MNRAS, 427, 625

Weaver R., McCray R., Castor J., Shapiro P., Moore R., 1977, ApJ, 218, 377

Werk J. K., et al., 2014, ApJ, 792, 8

White S. D. M., Rees M. J., 1978, MNRAS, 183, 341

Wilson J. R., 1985, in Centrella J. M., Leblanc J. M., Bowers R. L., eds, Numerical Astrophysics. p. 422

Wolfire M. G., Hollenbach D., McKee C. F., Tielens A. G. G. M., Bakes E. L. O., 1995, ApJ, 443, 152

Zel'dovich Y. B., 1970, A&A, 5, 84

van Leer B., 1976, in Computing in Plasma Physics and Astrophysics.

Chapter 2

A Superbubble Feedback Model for Galaxy Simulations

Reprinted from B.W. Keller, J. Wadsley, S.M. Benincasa, & H.M.P. Couchman 2014, Monthly Notices of the Royal Astronomical Society *Volume 442, Issue 4, pp. 3013-3025, DOI: 10.1093/mnras/stu1058. Published by Oxford University Press on behalf of the Royal Astronomical Society.*

Abstract

We present a new stellar feedback model that reproduces superbubbles. Superbubbles from clustered young stars evolve quite differently to individual supernovae and are substantially more efficient at generating gas motions. The essential new components of the model are thermal conduction, sub-grid evaporation and a sub-grid multi-phase treatment for cases where the simulation mass resolution is insufficient to model the early stages of the superbubble. The multi-phase stage is short compared to superbubble lifetimes. Thermal conduction physically regulates the hot gas mass without requiring a free parameter. Accurately following the hot component naturally avoids overcooling. Prior approaches tend to heat too much mass, leaving the hot ISM below 10^6 K and susceptible to rapid cooling unless ad-hoc fixes were used. The hot phase also allows feedback energy to correctly accumulate from multiple, clustered sources, including stellar winds and supernovae.

We employ high-resolution simulations of a single star cluster to show the model is insensitive to numerical resolution, unresolved ISM structure and suppression of conduction by magnetic fields. We also simulate a Milky Way analog and a dwarf galaxy. Both galaxies show regulated star formation and produce strong outflows.

2.1 Introduction

Galaxies are star factories: with their large potential wells, they accrete gas and convert that gas into stars. The throttle for this process is the energy released from these stars through winds and supernovae: stellar feedback. Without this large source of energy ($\sim 3 \times 10^{38}$ erg s^{-1} per solar mass of stars) to stir and heat the interstellar medium, star formation would consume all available gas for every galaxy in less than a Hubble time. Not only does stellar feedback allow star formation to self-regulate, it is one of the most important processes in producing a multiphase ISM (McKee & Ostriker, 1977). A third way feedback shapes the history and structure of gas in a galaxy is by cycling (and even ejecting) gas through outflows. Galactic winds can remove potential star-forming gas from a galaxy by propelling it out of a galaxy faster than the escape velocity. Gas 'fountains' can reduce the cold gas available in a galactic disc by cycling it between the disc and high in the galactic halo. This acts to temporarily store gas in a reservoir above the galactic plane, where it is too hot and diffuse to form stars. These outflows are likely an important component in determining the ultimate fate of a galaxy, and are the most plausible mechanism for metal enrichment observed in the circumgalactic medium (Songaila & Cowie, 1996; Davé et al., 1998).

Much work has been done to build feedback models based on the evolution of individual supernova blastwaves (e.g. Stinson et al., 2006), but these efforts have overlooked two key factors. First, star formation is clustered; new stars are spatially and temporally correlated, and feedback from their individual winds and supernovae merge, thermalize and grow as a *superbubble* rather than a series of isolated supernovae. Second, because superbubbles have both hot gas $> 10^6$ K and sharp temperature gradients, thermal conduction is significant (Weaver et al., 1977). Omitting this process can cause one to incorrectly estimate the interior density (and thus the amount of hot gas) of superbubbles by orders of magnitude, regardless of whether or not one can resolve the superbubble. In simulations of galaxy evolution, the temporal resolution required to resolve the pre-thermalization Sedov phase is out of reach (on the order of 100 yr), and even the post-thermalization early superbubble can require shorter timesteps than are practical. Worse still, during this period the amount of mass contained within the hot, rarefied interior of a superbubble is less than the mass of the progenitor star cluster. This can make it impossible to spatially resolve this stage in simulations where resolution elements are comparable in mass to star particles. This leads to denser, cooler feedback regions. These overcool and lead to ineffective feedback overall (Katz, 1992).

A number of approaches exist to attack the problem of overcooling. The earliest techniques were to simply deposit a fraction of the energy released in feedback events as kinetic energy (Navarro & White (1993), Mihos & Hernquist (1994), Dubois & Teyssier (2008), etc.). Gerritsen (1997) detailed a second approach; by introducing cooling shutoff, where feedback-heated gas is explicitly prevented from cooling radiatively, and Thacker & Couchman (2000) explored a range of different times for this shutoff period. Stinson et al. (2006) proposed using the time required to resolve a Sedov-Taylor blastwave, and showed that this can be an effective way of modelling feedback in cosmological simulations of galaxy evolution. Agertz et al. (2013) used a decaying non-cooling energy, where energy in a non-cooling state decayed back to the 'normal' cooling form. Another technique is to manually decouple density estimates and hydrodynamic interactions between feedback-heated gas and the cold ISM (Marri & White (2003), Scannapieco et al. (2006), etc.). With extremely high resolution, it is possible to generate rarefied hot gas from feedback directly without a subgrid treatment (e.g. Hopkins et al., 2012). However, as we argue here, mass transfer between hot and cold gas depends on the physics of conduction which relies on sub-parsec gradients. These are beyond the reach of even the highest resolution galaxy scale simulations so some subgrid modeling may be unavoidable.

Another approach has been to explicitly model the multiphase ISM below the resolution limit. Springel & Hernquist (2003) described a multiphase model based on the theoretical framework of McKee & Ostriker (1977). Each particle was composed of an isobaric mix of cold clouds and ambient warm to hot gas. Radiative cooling converts warmer gas into cold. The cold phase forms stars on a characteristic timescale chosen to yield a Schmidt-type star formation law. An empirical model of stellar feedback evaporates the cold phase. Springel & Hernquist (2003) recognized that while this model works well for simulating star formation and feedback in quiescent galaxies, the coupling of hot and cold mass can prevent hot gas from leaving the disc as winds or outflows. Their solution was to convert a fraction of the feedback energy in a kinetic kick on selected particles, in the same vein as Mihos & Hernquist (1994).

Both Dalla Vecchia & Schaye (2012) and Hopkins et al. (2012) have shown that it is possible to get consistent wind results for a given energy input model. Dalla

Vecchia & Schaye (2012) demonstrated that simply depositing energy stochastically to ensure a constant temperature increase for feedback-heated gas can directly generate winds. They found that for the same feedback energy, changing the temperature of feedback-heated gas results in significant differences in both star formation regulation and galactic outflows. Higher feedback temperatures, $\Delta T > 10^7$ K, avoid overcooling and allow for more efficient regulation and higher velocity galactic winds. This still leaves open the question of what sets this temperature? This question is equivalent to asking: *what sets the mass-loading in stellar feedback?* Previous feedback models have not explored key physical mechanisms, such as conduction, that affect mass-loading.

The above sub-grid models are reasonably successful at preventing overcooling. However, many of them have limitations which are increasingly severe with improving resolution. For example, stellar feedback in the form of kinetic energy is rapidly converted into thermal energy as it encounters the ISM and shocks (Durier & Dalla Vecchia, 2012). In nature, the gas heated by feedback doesn't completely stop cooling radiatively, it merely cools inefficiently. Applying a cooling shutoff is unlikely to give the correct behaviour in different star forming environments and is also dependent on the integrated energy injection from all nearby stars. Finally, because star formation is clustered, feedback is localized within starforming regions.

Recent studies such as Nath & Shchekinov (2013) and Sharma et al. (2014) have emphasized that feedback from clustered stars forms superbubbles, which behave quite differently from isolated supernovae. A key outcome is that superbubbles are intrinsically more efficient than individual supernovae at converting feedback energy into gas motions, particularly at late times and over larger scales. The reason for this difference is that gas heated by feedback remains distinct from the cooler surrounding material. Most current models smear together the hot bubble with the cold shell surrounding it. This results in an intermediate effective temperature that is prone to overcooling. Separating the hot and cold phases automatically avoids overcooling. Dalla Vecchia & Schaye (2012) achieved this with a stochastic feedback model. An alternative approach is to add an explicit hot reservoir to accumulate feedback mass and energy. This avoids overcooling without artificially turning off cooling and correctly handles feedback from multiple sources over time without resorting to a stochastic approach. Such a model still leaves the bubble mass as a free parameter. Mac Low & McCray (1988) showed that thermal conduction controls the mass flow into the hot bubble from the cold shell. This evaporation process regulates the temperature of the hot bubble and determines how much mass is heated by feedback. Adding a sub-grid model for evaporation allows the physics of thermal conduction to set bubble temperatures and masses.

Drawing on these facts, we can construct a *superbubble*-based feedback model. As outlined in Mac Low & McCray (1988), superbubbles efficiently convert feedback energy into thermal energy in a hot phase and kinetic energy in an expanding cold shell. The rarefied hot phase cools inefficiently, avoiding overcooling. Thus a correct model requires following distinct hot and cold phases even when they may be difficult to resolve directly. A new requirement with respect to prior feedback models is the inclusion of thermal conduction. Conduction both smooths the temperature distribution in the hot gas and mediates mass flows where hot gas meets a cold phase. Thus a second feature of such a model is that an explicit physical process sets the amount of hot gas in the ISM and in outflows.

In this paper, we begin by explaining the theoretical underpinning and numerical implementation of the superbubble-based feedback method in section 2.2. In section 2.3.1 we use a single star cluster to illustrate the effectiveness of our model at capturing the basic behaviour of superbubbles at high and low resolution. In section 2.3.2 we apply the model to simulations of isolated galaxies to explore the impact on the galaxy scale ISM and the production of outflows.

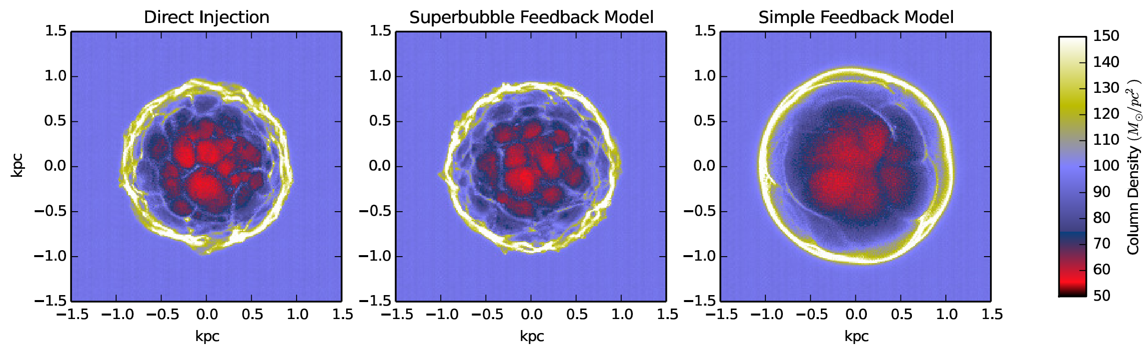

Figure 2.1: Column density projections from the simulations of a single star cluster with mass 3×10^4 $M_\odot$, 50 Myr after the cluster has formed. The superbubble feedback model (center column) produces bubbles with radius and enclosed mass that match well to the direct injection simulations (left column). This is shown quantitatively in figure 2.2 and figure 2.6. The simple model (right column), despite injecting the same amount of energy, fails to generate enough hot mass inside the bubble, and subsequently suppresses the growth of Vishniac instabilities along the bubble edge because of the poorly resolved hot interior.

2.2 Thermal Conduction and Feedback Method

Our new treatment of feedback has three components. The first is the addition of thermal conduction. Inside resolved hot bubbles, thermal conduction maintains uniform temperatures. In the presence of strong gradients, thermal conduction can lead to evaporative mass flows from cold to hot gas. The second component is a stochastic model of evaporation to allow resolved hot gas to continue to gain mass from nearby cold gas. Thus, the amount of cold gas heated by feedback is not a free parameter, but is set by thermal conduction. Without a mechanism like thermal conduction, this hot gas mass is set by how many fluid elements have feedback energy deposited into them. It is important to note that in our model these processes operate everywhere temperatures are above $10^5 K$.

Finally, in the first few Myr of feedback heating, the mass contained within a hot bubble can be smaller than the simulation gas mass resolution. To prevent overcooling, we allow resolution elements to become briefly two-phase; a hot interior (bubble) in contact with a cold shell. Evaporation of the cold shell moderates this two-phase period, rapidly returning particles to single phase once their cold phase has been fully evaporated. Our model does not assume all fluid elements are multiphase, but only those in which a partial feedback region exists. This allows the model to follow winds and outflows without continuing to rely on sub-grid machinery.

Young stellar populations steadily release energy in the form of winds and SNe at a rate of 3×10^{38} erg $\mathrm{s}^{-1}\mathrm{M}_\odot^{-1}$ for around 40 Myr (Leitherer et al., 1999). We deposit this energy into the gas particle nearest to the star particle. In following with past work, we use the feedback rates and times for supernovae, but the method is general enough to handle heating from stellar winds, ionization, etc. Heating takes effect 4 Myr after a star forms, and continues until 30 Myr after the star particle forms (the time associated with SNII from OB stars). Thus, each supernova releases 10^{51} erg, and each star particle will release 10^{49} $\mathrm{erg}\mathrm{M}_\odot^{-1}$ using the Chabrier (2003) IMF.

2.2.1 Thermal Conduction

In an ionized gas, thermal conduction, mediated by electrons, transports heat down temperature gradients. This flux, $\mathbf{Q} = -\kappa \nabla T$, depends on the temperature gradient and the conduction coefficient, as derived by Cowie & McKee (1977),

$$\kappa(T) = 1.8 \left(\frac{2}{\pi}\right)^{3/2} \frac{T^{5/2} k_B^{7/2}}{m_e\, e^4 \ln \Lambda}. \tag{2.1}$$

This coefficient depends only on the Coulomb logarithm $\ln \Lambda$ (which has an extremely weak dependence on density), and is well approximated by $\kappa(T) = \kappa_0\, T^{5/2}$, where κ_0 is 6.1×10^{-7} $\mathrm{erg\,s^{-1}K^{-7/2}cm^{-1}}$ in the absence of magnetic fields. This drives a corresponding mass flux, *in the opposite direction*. With spherical symmetry, this implies a mass flow rate that depends on the sound speed in the hot gas, c_s, as follows,

$$\frac{5}{2}\dot{M} c_\mathrm{s}^2 = 4\,\pi^2 r^2 \kappa(T) \frac{\mathrm{d}T}{\mathrm{d}r}. \tag{2.2}$$

These rates hold only when the mean free path of electrons in the medium is smaller than the scale length of the temperature gradient. If the gradient becomes steep enough, the heat flux (and corresponding mass flux) saturates at a value that depends only on the density, temperature, and thermal velocity of the electrons in the medium (Cowie & McKee, 1977),

$$\mathbf{Q} = \nabla \left(\frac{3}{2} n_e k_B T_e v_e\right). \tag{2.3}$$

This saturation has the convenient numerical side effect of setting the smallest timestep required to resolve this mass flux to $\sim 1/17$ the standard Courant time, $t_C = \Delta x/c_s$.

In situations where the temperature gradient is embedded in a strong magnetic field, the value of κ_0 can be reduced by factors approaching an order of magnitude depending on the strength and configuration of the magnetic fields (Cowie & McKee, 1977).

The edge of a feedback-driven superbubble presents a strong discontinuity in both temperature and density. Interior to the bubble, gas has temperatures of $\sim 10^6$ K and densities of $\sim 10^{-3}$ cm^{-3}, while the shell can have temperatures below 100 K and densities of ~ 10 cm^{-3} (Chevalier, 1974). This generates significant mass and energy flows due to thermal conduction.

2.2.2 Evaporation

The dominant physical process governing mass flux between the hot and cold phases of a feedback bubble is thermal conduction between the dense shell and the hot interior. As this process takes place on length scales far below the resolution limit, we must capture its effects in a subgrid model. For the thin shell surrounding a feedback bubble, thermal conduction causes an evaporative mass flux from the cold shell into the hot bubble. Following Mac Low & McCray (1988), the mass flux into a bubble with interior temperature T is,

$$\frac{\mathrm{d}M_b}{\mathrm{d}t} = \frac{4\,\pi\mu}{25 k_B}\kappa_0\,\frac{\Delta T^{5/2}}{\Delta x}\;A, \tag{2.4}$$

where A is the bubble surface area and Δx is the thickness of the hot layer ($\Delta x = R$ for spherical symmetry). For the Smoothed Particle Hydrodynamics (SPH) method used for our tests, we calculate evaporation using the outer layer of hot particles bordering the cold gas. The members of this layer are those with no other hot particles within 45^o of the vector to the centre of mass of their cold neighbours. As we cannot directly determine the radius of a well-resolved superbubble without expensive non-local calculations, we need a way to allow each particle to estimate the radius and thus its fractional contribution of the shell surface area. The total area estimated by all hot particles in a bubble should approach $\sim 4\pi R^2$ where R is the bubble radius. For a poorly resolved bubble $R \sim 1-2\,h$, where h is a hot particle's SPH smoothing length. For larger bubbles each hot particle contributes an area of $\sim h^2$ and each particle sees a nearly plane-parallel section of the cold shell. We examined a number of bubbles at different stages of growth, as well as a plane-parallel slab, and empirically found that a good per-particle area estimate was $A = \frac{6\,\pi\,h^2}{N_{\mathrm{hot}}}$, where N_{hot} is the number of hot neighbours for that particle and $\Delta x = h$. We stress that this is a fit for our specific SPH neighbour approach (described below) that should be recalibrated for other codes.

The mass evaporation rate can be converted into a probability that a resolution element with cold mass m converts into a hot one over a time period Δt as follows,

$$P_{evap} = \frac{\mathrm{d}M_b}{\mathrm{d}t}\frac{\Delta t}{m}. \tag{2.5}$$

This allows us to stochastically choose full particles to evaporate, and prevent overcooling due to fractional particle evaporation (exactly the same overcooling problem seen in feedback heating). Each hot particle determines how many cold-shell particles N_{evap} will evaporate each timestep, and then chooses the N_{evap} nearest cold particles, and averages the thermal energy of itself and those particles. These particles spontaneously join the hot bubble (demonstrated in the figures in section 2.3.1.3). The thermal conduction rates calculated are capped using the saturation values derived in Cowie & McKee (1977). Within an SPH framework, this is well approximated using,

$$\frac{\mathrm{d}M_{sat}}{\mathrm{d}t} = 17\rho\, c_{\mathrm{s}} h^2. \tag{2.6}$$

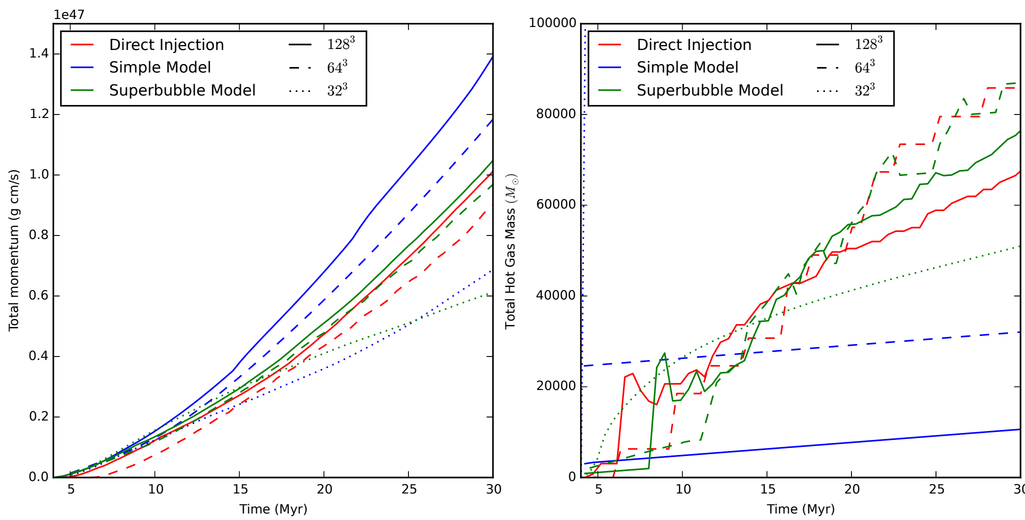

Figure 2.2: Feedback effects as a function of resolution. The above figure shows on the left the total radial momentum imparted to the medium, and on the right the total amount of mass heated to above 10^5 K. The red curves are the direct injection results, the blue corresponds to the simple feedback, while the green shows the results of the superbubble model. Solid lines show the values from simulations run with resolutions of 128^3 particles, dashed for 64^3, and dotted for 32^3. Note that for the 32^3 run, the simple model produces $\sim 2 \times 10^5$ $M_\odot$ of hot gas.

2.2.3 Multiphase Fluid Elements

When feedback energy is deposited in a low-resolution simulation, or is deposited as a luminosity, the temperature and density are certain to be under- and over-estimated respectively. This problem leads to the well-known overcooling problem that has typically been addressed by disabling cooling for some amount of time for feedback-heated gas (e.g. Stinson et al. (2006), Springel & Hernquist (2003), or by stochastic feedback heating, where the temperature change of a fluid element heated by feedback is fixed to a constant value (e.g. Dalla Vecchia & Schaye (2012). We employ a third option: storing feedback energy in a second phase that is in pressure equilibrium with the rest of the fluid inside an element.

Fluid elements (gas cells or particles) enter the multi-phase state if they are given energy from feedback, and if their temperature is below 10^5 K (the 'hot' threshold). Multiphase elements have two values for their mass and energy, related to their total mass m and energy E by:

$$m = m_{\rm hot} + m_{\rm cold} \tag{2.7}$$

$$E = u_{\rm hot} m_{\rm hot} + u_{\rm cold} m_{\rm cold} \tag{2.8}$$

Assuming pressure equilibrium, both phases will have the same pressure P, and their densities are found using this and the total density ρ:

$$\frac{P}{\rho} = \frac{(\gamma - 1)E}{m} \tag{2.9}$$

$$\rho_{\rm cold} = \frac{P}{(\gamma - 1)u_{\rm cold}} \tag{2.10}$$

$$\rho_{\rm hot} = \frac{P}{(\gamma - 1)u_{\rm hot}} \tag{2.11}$$

Both the cold and hot phases are allowed to radiatively cool using their separate temperatures and densities. When PdV work is done to a multiphase particle, it is shared between the two phases weighted by their respective fraction of the total energy E,

$$\dot{u}_{\rm PdV,cold} = m\ \dot{u}_{\rm PdV} \frac{u_{\rm cold}}{E} \tag{2.12}$$

$$\dot{u}_{\rm PdV,hot} = m\ \dot{u}_{\rm PdV} \frac{u_{\rm hot}}{E}. \tag{2.13}$$

In the absence of heating and cooling, this allows each phase to correctly maintain constant entropy as the densities change.

Mass flux between the hot and cold phase is calculated in a continuous manner consistent with the prior evaporation scheme. Each timestep, a multi-phase element evaporates a fraction of its cold phase into the hot phase,

$$\frac{\mathrm{d}M_b}{\mathrm{d}t} = \frac{16\pi\mu}{25k_B}\kappa_0(T_{\mathrm{hot}}^{5/2})\ h. \tag{2.14}$$

Once an element has evaporated all of its mass into the hot phase, or if the hot phase cools below 10^5 K, it is returned to the single-phase state.

2.2.4 SPH Implementation

We implemented this method in the SPH code GASOLINE (Wadsley et al., 2004) with updates described in Shen et al. (2010). These include a sub-grid model for turbulent mixing of metals and energy. The heating and cooling include photoelectric heating of dust grains, UV heating and ionization and cooling due to hydrogen, helium and metals.

The SPH hydrodynamic treatment has had some further, key updates. We currently use a standard SPH density estimator but a geometric density average in the SPH force expression: $(P_i + P_j)/(\rho_i\,\rho_j)$ in place of $P_i/\rho_i^2 + P_j/\rho_j^2$ where P_i and ρ_i are particle pressures and densities respectively. This force expression alleviates numerical surface tension associated with density discontinuities, which is important for correct Kelvin-Hemholtz instabilities and ablation of cold blobs (as in the Agertz et al 2010 'blob' test). A similar force expression was first proposed by Ritchie & Thomas (2001). Geometric density averaged force expressions are now employed in all modern SPH codes (e.g. Hopkins (2013), Saitoh & Makino (2013), Kawata et al. (2013), Hu et al. (2014) and Read et al. (2010)). As stated in Read et al. (2010) and Saitoh & Makino (2013), a key requirement for correct results with the modified force expression is a consistent energy equation that conserves entropy (which we employ). This is important to correctly model strong shocks, such as Sedov blasts. The extreme temperature jumps at strong shocks also require the time-step limiter of Saitoh & Makino (2009). The modern SPH code papers listed above all employ these updates and demonstrate accurate solutions for strong shocks (e.g. Sedov blasts) and shear flows (e.g. Kelvin Helmholz instabilities and the destruction of cold blobs).

For the tests shown here we used the Wendland C_2 kernel detailed in Dehnen & Aly (2012) with 64 neigbours where the SPH smoothing distance is defined so that the kernel weight drops to zero at $2\,h$.

Sharp density contrasts, as seen in highly resolved superbubbles, can require additional checks on the neighbour finding component of the SPH method. For example, hot particles can inadvertently become hydrodynamically decoupled from cold ones for a fixed number of neighbours. A full set of cold neighbours can sit at the edge of the kernel, where their contribution is negligible. The hot particle can thus have a full set of neighbours but feel minimal forces. We increase the number of neighbours until at least 18 neighbours are within $1.41\,h$.

With respect to heating and cooling, for this work we used the Ritchie & Thomas (2001) density when calculating cooling rates to sharpen the density contrast between hot and cold gas. This is particularly useful at lower resolution when the hot bubble is resolved with a small number of particles. This improves the ability of low resolution runs to give similar energy loss rates to high resolution versions.

Feedback can increase gas particle masses substantially in the rare event that a gas particle spends a lot of time within star clusters without forming a star itself. This can degrade the accuracy of the SPH method. We avoid this problem by splitting particles that exceed 4/3 their initial mass into two equal mass particles with the same properties. This affects a very small fraction of the particles.

These modifications, along with detailed testing, will be discussed in a forthcoming paper on GASOLINE2. For reference, the quality of our results on the tests discussed here is similar to the results presented for other modern modified SPH codes (e.g. Hopkins, 2013).

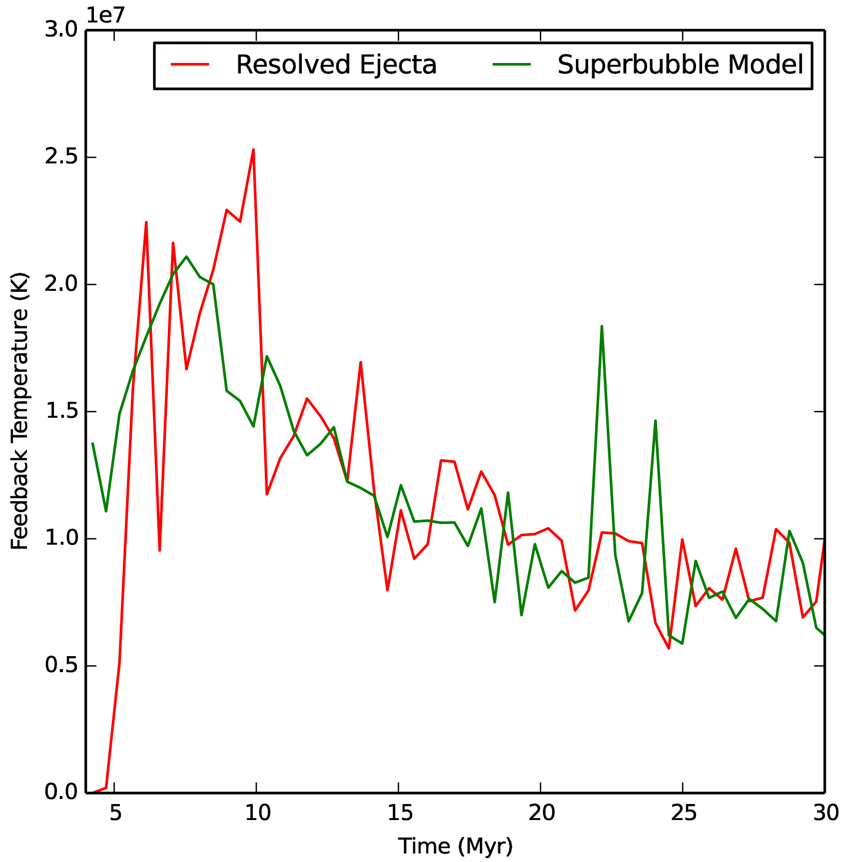

Figure 2.3: Peak temperature of feedback-heated gas inside the isolated star cluster's hot bubble. Evaporation quickly enters the self-regulating regime, and the temperature is roughly constant for the last 15 Myr of feedback.

2.3 Simulations

2.3.1 High-Resolution Star Cluster Test

We began by exploring models of a single, isolated superbubbles at high resolution. For these tests, we employed three physical models. The *Direct injection* approach models as much physics as possible from first principles. Feedback mass and energy is modelled via a stream of new gas particles created from the star cluster. This approach only works when the gas resolution elements are much smaller than the star cluster mass. The only component of this model that is sub-grid is evaporation as this occurs on extremely small length scales. *Superbubble Feedback* refers to our new model. The key addition over the direct approach is the sub-grid multiphase treatment. Feedback energy and mass is injected into existing particles which may split.

We also include a *Simple Feedback Model* modeled after that proposed by Agertz et al. (2013). This model is a stand-in for models typically used to date and does not include conduction or evaporation. Feedback mass and energy is given to the nearest gas particle to the star cluster. This simple model incorporates a two-component energy treatment with radiative cooling disabled for feedback energy. Feedback energy is steadily converted into the regular, cooling form with an e-folding time of 5 Myr.

2.3.1.1 Basic Superbubble

We placed a star cluster with mass 3×10^4 M$_\odot$ in a uniform periodic box $2 \times 2 \times 2$ kpc in size, containing 10^3 K gas with solar metallicity at a density of 1 cm^{-3}. This gives a gas particle mass of 760 $M_\odot$, 6080 $M_\odot$, and 48640 $M_\odot$ for resolutions of 128^3, 64^3, and 32^3 respectively. These tests do not include photoheating.

Figure 2.1 shows the column density projection for the three different feedback models in an isotropic medium. The hot interior of the bubble produced using the simple feedback model contains less mass at 128^3 than the direct injection model and is subsequently too poorly resolved for the instabilities formed in the accelerated shell (Vishniac, 1983) to mix the bubble and shell through turbulence and diffusion.

As figure 2.2 shows, the superbubble feedback model performs much better than the simple model in reproducing the hot mass production rate from the high-resolution direct injection model, and lacks the extreme resolution sensitivity that the simple

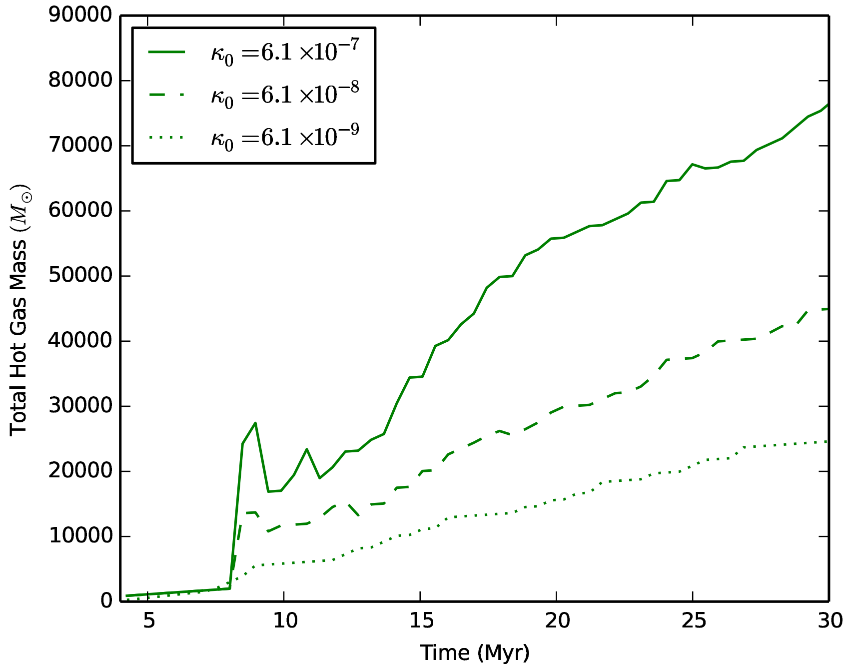

Figure 2.4: Hot mass production as a function of the conduction coefficient κ_0. As this figure shows, reducing κ_0 by a factor of 100 reduces the amount of hot mass generated through conduction by only a factor of ~ 2. All κ_0 values have units of erg $\mathrm{s}^{-1}\mathrm{K}^{-7/2}\mathrm{cm}^{-1}$.

model exhibits for the amount of gas heated. The simple model only heats ~ 4 gas particles. For the 128^3 and 64^3 resolutions, this gives too little hot mass. For 32^3 (extremely poor resolution, in fact with gas particles more massive than the entire cluster), this produces more than twice too much hot mass (more than 2×10^5 $M_\odot$). Meanwhile the simulation with the superbubble feedback model only underestimates the hot mass by roughly a third of the target 128^3 direct injection simulation when used at a resolution 32^3. The decreased momentum in the lower-resolution runs is likely due to particles staying longer in the multiphase state. More massive particles take longer to fully evaporate, and thus some mass that would be part of a pressure-driven cold shell at higher resolution is tied up in the cold part of multiphase particles.

Figure 2.3 shows that the actual peak temperature of the feedback-heated bubble in the isolated star cluster run is roughly 1×10^7K.

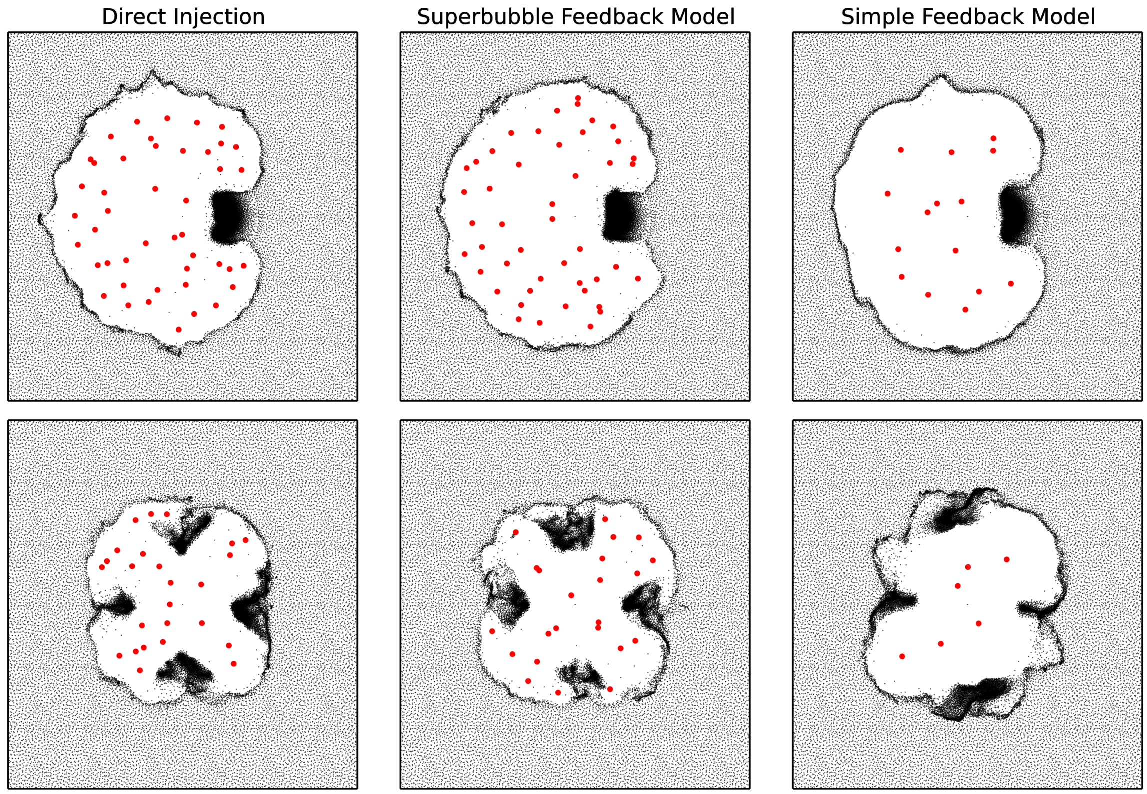

Figure 2.5: 3 kpc wide slices from the same three methods shown in figure 2.1, also at 50 Myr, but applied to a star cluster in an inhomogeneous medium. Particles whose smoothing length intersects z=0 kpc are shown. Particles above 10^5 K are shown in red. The upper row shows simulations with a single clump, while the bottom row shows simulations with 6 clumps.

2.3.1.2 Suppressed conduction

We also ran a set of simulations with the value of κ_0 used in the model reduced by a factor of 10 and a factor of 100. Since there is some uncertainty as to this coefficient in a magnetized ISM, we use this test to show that the self-regulating effect of conduction is insensitive to variation in κ_0.

Figure 2.4 shows the hot mass generated in simulations with 3 different values of κ_0. The dashed curve shows a reasonable lower limit for κ_0 (Cowie & McKee, 1977), while the dotted curve shows a much more extreme conduction reduction than is expected in nature. Both curves illustrate the insensitivity of the method to reductions in the conduction rate. Even reducing κ_0 by 100 only results in a reduction of the hot mass inside the bubble to just around a third.

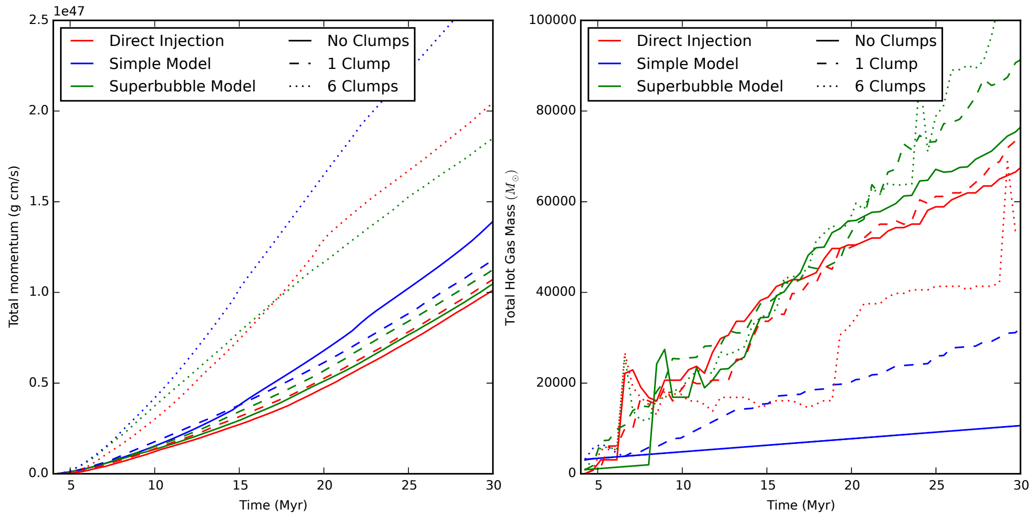

Figure 2.6: Feedback effects as a function of ISM homogeneity. The above figure shows on the left the total radial momentum imparted to the medium, and on the right the total amount of mass heated to above 10^5 K. The red curves are the direct injection results, the blue corresponds to the simple feedback, while the green shows the results of the superbubble model. Solid curves show the results for a homogeneous ISM, dashed for a single dense clump, and dotted for 6 dense clumps.

2.3.1.3 Clumpy Medium

As the real ISM is highly inhomogeneous (and as Silich et al. (1996) showed, cold clumps can also be a source of evaporated cold material), we ran two additional simulations with cold, dense clumps with 100 cm^{-3} density and 10 K gas in an ambient medium of 0.5 cm^{-3} at 1000 K. This gives roughly the same amount of mass enclosed within the hot bubble at 30 Myr. The first contains a single spherical clump with a radius of 0.2 kpc. The second contains the same amount of cold mass spread over 6 clumps arranged at the center of each face of a cube 0.2 kpc surrounding the star. We use this idealized clumpy medium to test the sensitivity of the model to small scale structure that may be unresolved in lower resolution simulations. Figure 2.5 shows a slice showing SPH particles at 50 Myr for the two clumpy cases.

Figure 2.6 shows that the superbubble model is also capable of handling feedback into a clumpy medium. With more than an order of magnitude difference in the total hot mass compared to the simple model, along with less sensitivity to environment or resolution, the superbubble model is better suited for probing galactic outflows in simulations.

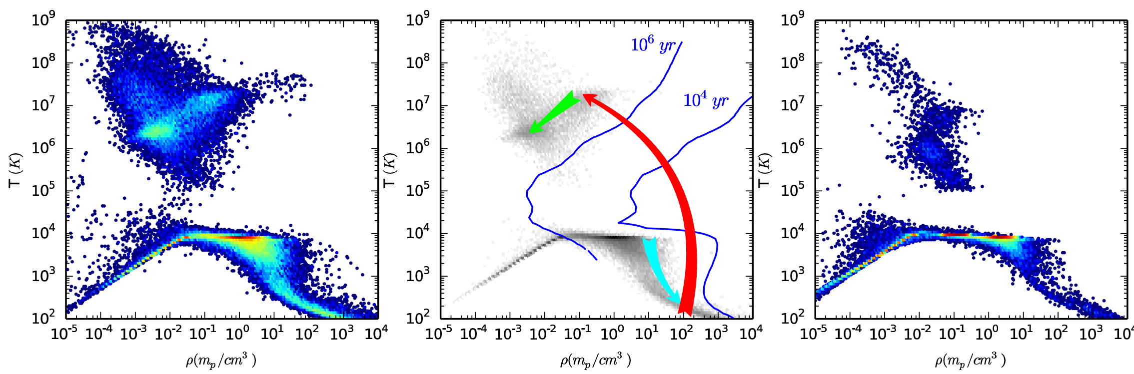

Figure 2.7: Phase diagrams for the Milky Way (left) and dwarf (right) simulations at 200 Myr. The central panel shows a typical path for gas ejected from the Milky Way. First gas cools radiatively (cyan path) to high density, where it becomes multiphase as its hot component is heated to $\sim 10^7$ K by feedback (red path) from nearby stars formed from its neighbouring high density gas. The hot phase cools primarily through adiabatic expansion (green path). This process is often repeated one or more times, with gas that is entirely hot phase being ejected from the disc. Cooling times of 10^4 yr and 10^6 yr are shown in blue. The majority of the hot gas in the upper left quadrant of the phase diagram has cooling times $> 10^8$ yr. The cooling curve for 10^8 yr passes through the green curve. Note that particles in the multiphase state show the temperature and density for each state as separate points. The mean properties of multiphase particles would place them in regions with short cooling times.

2.3.2 Galaxy Simulations

2.3.2.1 Initial Conditions and Parameters

We used the isolated disc galaxy initial condition from the AGORA comparison project (Kim et al., 2013). These initial conditions were generated using the equilibrium disc generating code of Springel et al. (2005). This galaxy is similar to a MW-type spiral galaxy at $z = 0$. For our dwarf simulation, we scaled the masses down by a factor of 100, and the length scales by a factor of $100^{1/3}$, preserving the physical densities in the initial conditions and lowering the surface density. The dwarf is thus similar to a low surface density local dwarf spiral. These initial conditions were intended to be similar to the $G10$ and $G12$ initial conditions used in Dalla Vecchia & Schaye (2012). The properties of these initial conditions are shown in table 1. Both simulations have 312500 total particles and 100000 gas particles, so that the mass resolution is substantially higher in the dwarf. The initial gas metallicity is solar in both cases.

We used the standard GASOLINE star-formation recipe, based on the algorithm proposed by Katz (1992) and detailed further in Stinson et al. (2006). We use a density threshold for star formation n_{SF} shown in table 1 along with a temperature threshold of $T < 10^4$ K. Thus, for a given eligible gas particle($n > n_{SF}$ and $T < T_{SF}$, the probability of forming a star each timestep $P_{SF} = 1 - \exp\frac{-0.05\ \Delta t}{t_{\rm ff}}$, depends only on the free-fall time $t_{\rm ff}$. This corresponds to the effective star formation density rate of $\dot{\rho}_* = 0.05\ \frac{\rho_{gas}}{t_{\rm ff}}$. We also include UV heating for $z = 0$ (as in Shen et al., 2010) and a pressure floor that ensures gas does not collapse beyond the resolvable Jeans length (Machacek et al., 2001).

We also simulated these initial conditions using the established 'blastwave' feedback model from Stinson et al. (2006), which has been a standard feedback model for galaxy simulations in numerous previous studies.

Simulation	$M_{tot}(\mathrm{M}_\odot)$	$M_{gas}(\mathrm{M}_\odot)$	ϵ(pc)	$n_{SF}\mathrm{cm}^{-3}$
Milky Way	1.3×10^{12}	8.6×10^9	20	> 10
Dwarf	1.3×10^{10}	8.6×10^7	4.3	> 50

Table 2.1: Disc galaxy initial conditions. ϵ is the gravitational softening and n_{SF} is the star formation density threshold, above which stars are allowed to form.

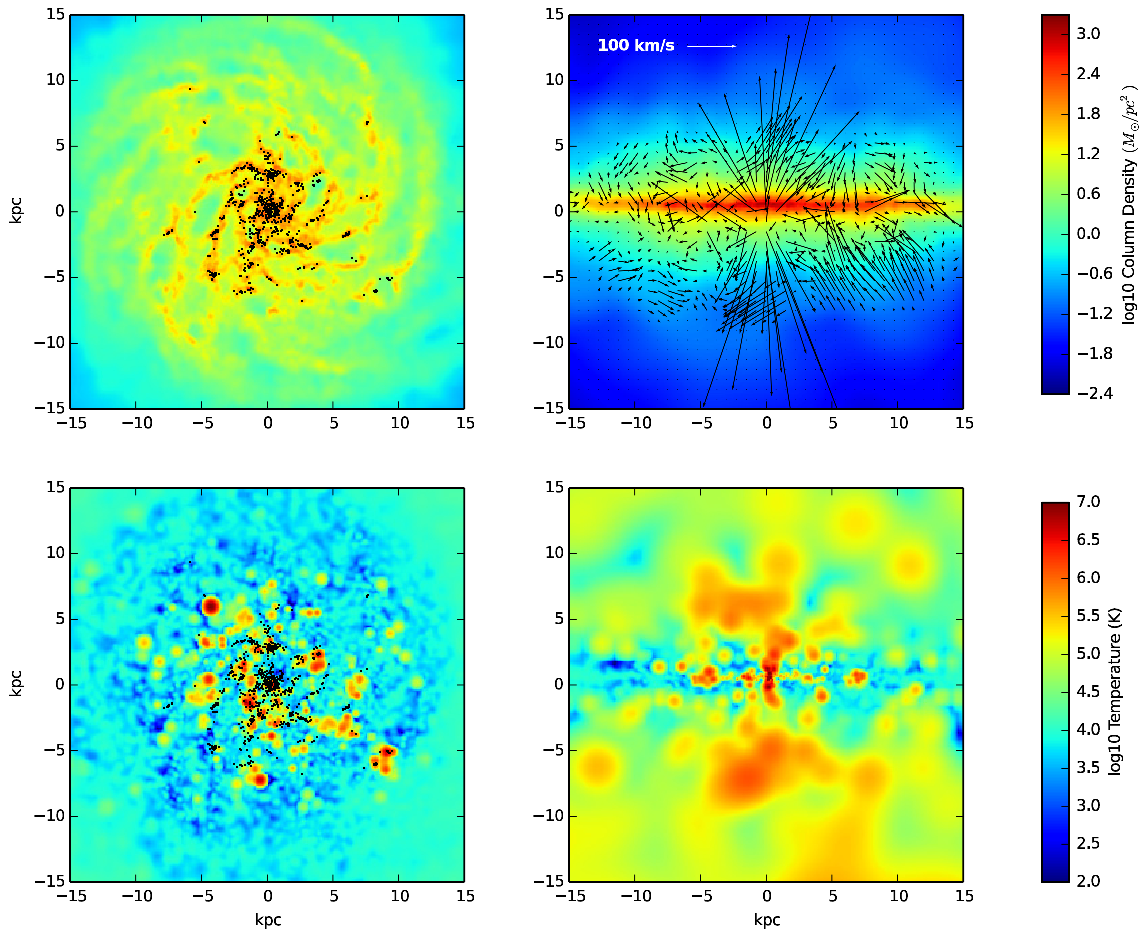

Figure 2.8: Column Density (upper row) and temperature for the Milky Way simulation at 300 Myr. The vectors show the in-plane velocity. Temperatures shown are averages between the two phases for multiphase particles. Black points in the face-on images show stars formed within the last 20 Myr. Note that gas is both leaving the disc near the galactic core, and returning in some places near the edge.

2.3.2.2 ISM properties and Star Formation Rates

Figure 2.7 shows phase diagrams from both Milky Way and dwarf galaxies. Figure 2.8 shows column density and temperature for the Milky Way, and figure 2.9 shows star formation rates and outflow properties. Figures 2.10 and 2.11 show the same for the dwarf galaxy. The Kennicutt-Schmidt relation for both galaxies is shown in figure 2.12. The star formation and outflow properties are discussed in section 2.3.2.3. Finally, we show some properties of the multiphase particles in figure 2.13.

Figure 2.7 shows that phase diagrams for galaxies using superbubble feedback strongly distinguish between pre- and post-feedback gas. Above $\sim 10^5$ K, we see (especially in the Milky Way), a hot medium of including halo gas and low density gas inside superbubbles within the galaxy disc (see the temperature slices in figures 2.8 and 2.10 for images of the gas temperature in these bubbles). The bulk of the gas lies at a roughly 10^4 K equilibrium between cooling and photoheating from the UV background. A cold medium of both dense shells surrounding superbubbles and cooling clouds (soon to form stars) also forms in both the Milky Way and (to a lesser extent) the dwarf. The central panel shows a schematic of how gas migrates between these regions. Radiative cooling (blue arrow), bring gas to high densities. Feedback creates a second hot phase in nearby gas particles. The cold component is relatively unaffected though it can compress due to the increased pressure (staying near the tip of the blue arrow). The hot and cold phases of multiphase particles are plotted separately. The hot component immediately moves to low density and high temperatures, $\gtrsim 10^7$ K (the red arrow). If the particle continues to receive feedback, evaporation rapidly consumes its cold part and the particle can flow out to the halo and remain buoyant and slow cooling. It evolves adiabatically as it does so (green arrow).

This panel is telling in that it shows that no gas is found within the ‘forbidden’ region of short cooling times of $\lesssim 10^4$ yr. Cooling-shutoff methods often produce large quantities of this gas in a high temperature, high density state. If we were to simply take the average temperature and density of the multiphase particles, they would almost entirely lie within this region, on the line connecting the cold and hot phases (which, of course, is exactly the impetus for using multiphase particles, since a particle with the average properties would cool away all of its feedback energy much too rapidly).

The roughly fixed amount of gas heated in the superbubble simulations shown

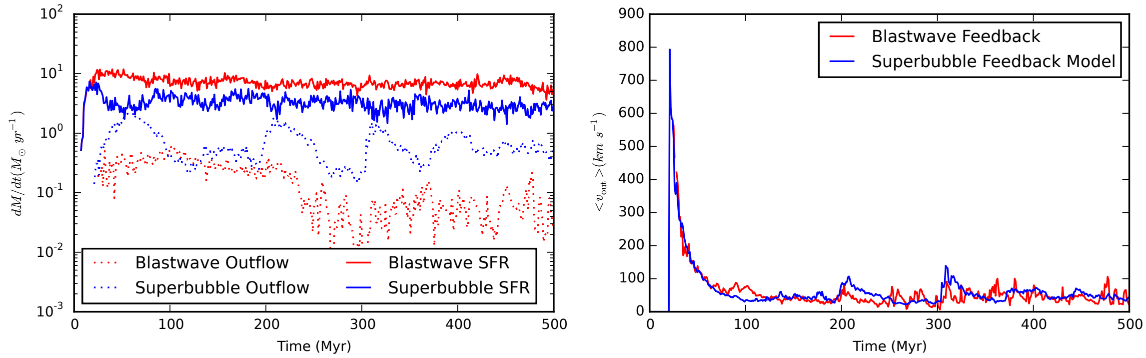

Figure 2.9: Outflow evolution for the Milky Way-like simulation. The left hand plot shows the star formation rate and the outflow rate. The right hand plot shows the average outflow velocity.

previously gives a roughly constant feedback-heated gas temperature of $\sim 2 \times 10^7$ K. Figure 2.3 shows that the actual peak temperature of the feedback-heated bubble in the isolated star cluster run varies between slightly less than this, to $\sim 1 \times 10^7$K, due to some cooling in the hot bubble. This suggests that the model should behave similarly to the stochastic thermal feedback model presented in Dalla Vecchia & Schaye (2012).

As the multiphase fluid particles exist to bridge the gap between when the hot interior of a superbubble contains too little mass to be resolved and the later stage when resolved physics can take over, we should find that particles stay in this phase for only a fraction of the lifetime of a superbubble. From Mac Low & McCray (1988), the cooling time for superbubbles is on the order of a few 10 Myr, with a weak dependence on feedback luminosity and the surrounding ISM density and metallicity.

We should expect that on average, multiphase particles convert back to single phase in less than this time, a few Myr. In addition to their lifetimes, we should expect multiphase particles to cluster in the discs of our galaxy simulations (since they are spatially correlated with the stars that are heating them), and that hot winds leaving the galaxy are composed of fully-resolved, hot gas. These winds are released when superbubbles grow large enough to break out of the denser disc ISM, and thus should be well within the resolved phase for these simulations.

Figure 2.13 shows the duration that all particles stay in the multiphase state as well as the maximum height reached by multiphase particles. The top figure shows that the vast majority of particles in either the dwarf or the Milky Way convert back to single phase within 10 Myr. The mean multiphase lifetime for the Milky Way

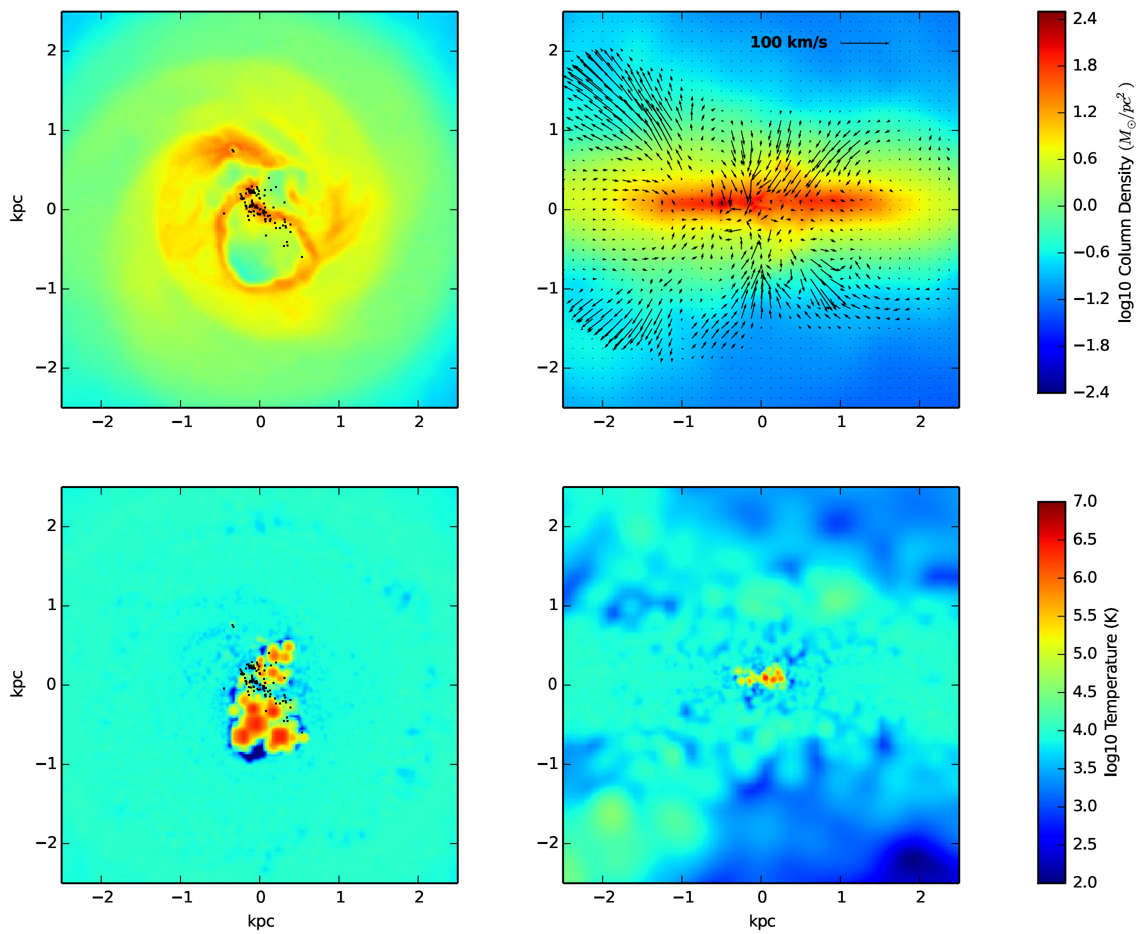

Figure 2.10: Column Density (upper row) and temperature for the dwarf simulation at 300 Myr. The vectors in show the in-plane velocity. Temperatures shown are once again averages between the two phases for multiphase particles. Note the much more 'puffed up' appearance compared to the Milky Way, due to the more mass-loaded winds

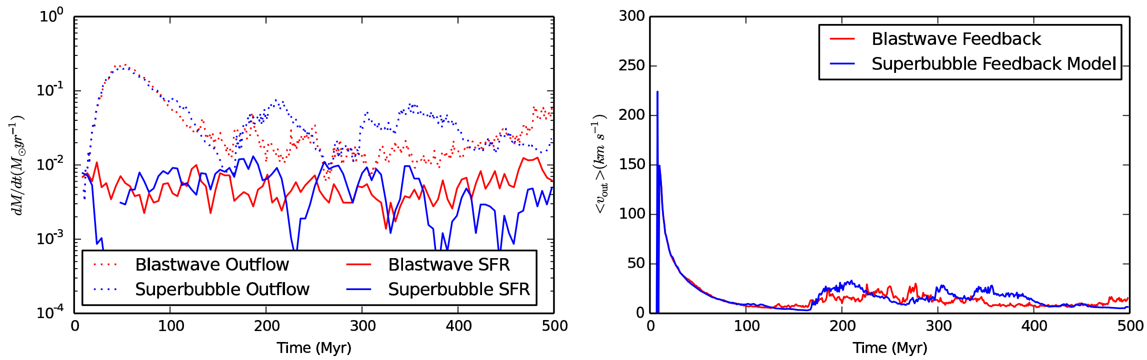

Figure 2.11: Outflow evolution for the dwarf galaxy. Note that the vertical ranges are different than in figure 2.9

was 6.6 Myr, and 2.7 Myr for the dwarf, well within the range we should expect. The reason for the shorter multiphase lifetimes in the dwarf galaxy is simply the better mass resolution: the hot bubble interior becomes resolved earlier in the dwarf than in the Milky Way. Fewer than 0.5 per cent of multiphase particles ever stay in the multiphase state for more than 50 Myr in both the Milky Way and the dwarf. The bottom figure shows, again as we should expect, that most multiphase particles convert back to single phase before they reach 1 scale height. The mean maximum height for multiphase particles was roughly 1/2 a scale height for both simulations, 0.51 kpc and 0.13 kpc for the Milky Way and dwarf respectively. Neither simulation had any multiphase particles reaching heights of more than 10 kpc before converting back to single phase. This shows that multiphase particles are essentially embedded within the thin disc of the ISM: all of the mass outflowing is fully-resolved hot gas, and its behaviour is fully governed by standard hydrodynamics. The winds driven from both galaxies are ejected through nothing more than simple buoyancy.

2.3.2.3 Galaxy Morphology and Outflows

In order to compare superbubble feedback to Dalla Vecchia & Schaye (2012), we selected similar galaxies to the ones shown in their paper and calculated the properties of their outflows using a similar method. We adopt their two primary metrics, mass outflow rate $\dot{M}$ and mean outflow velocity $< v_{\rm out} >$. These two metrics give us an idea as to both how much gas is ejected from the galaxies, and how long that gas will take to return to the disc from the halo (if it does return at all).

We calculated outflows from our galaxy simulations by selecting particles that are

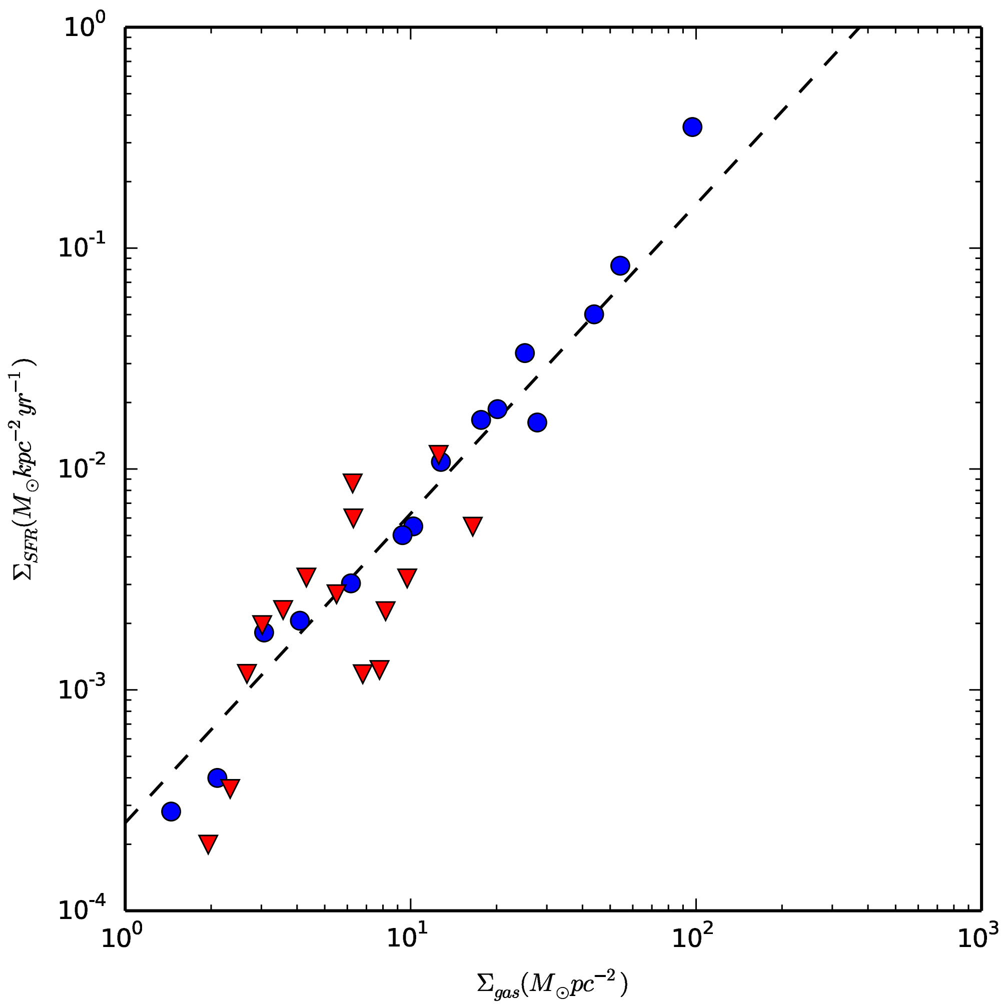

Figure 2.12: Kennicutt-Schmidt law in the Milky Way-like (blue points) and dwarf (red triangles) galaxies at 500 Myr. Surface densities were calculated in radial annuli. The dashed line shows the Kennicutt-Schmidt Law. The superbubble model is easily able to regulate star formation rates to within this range.

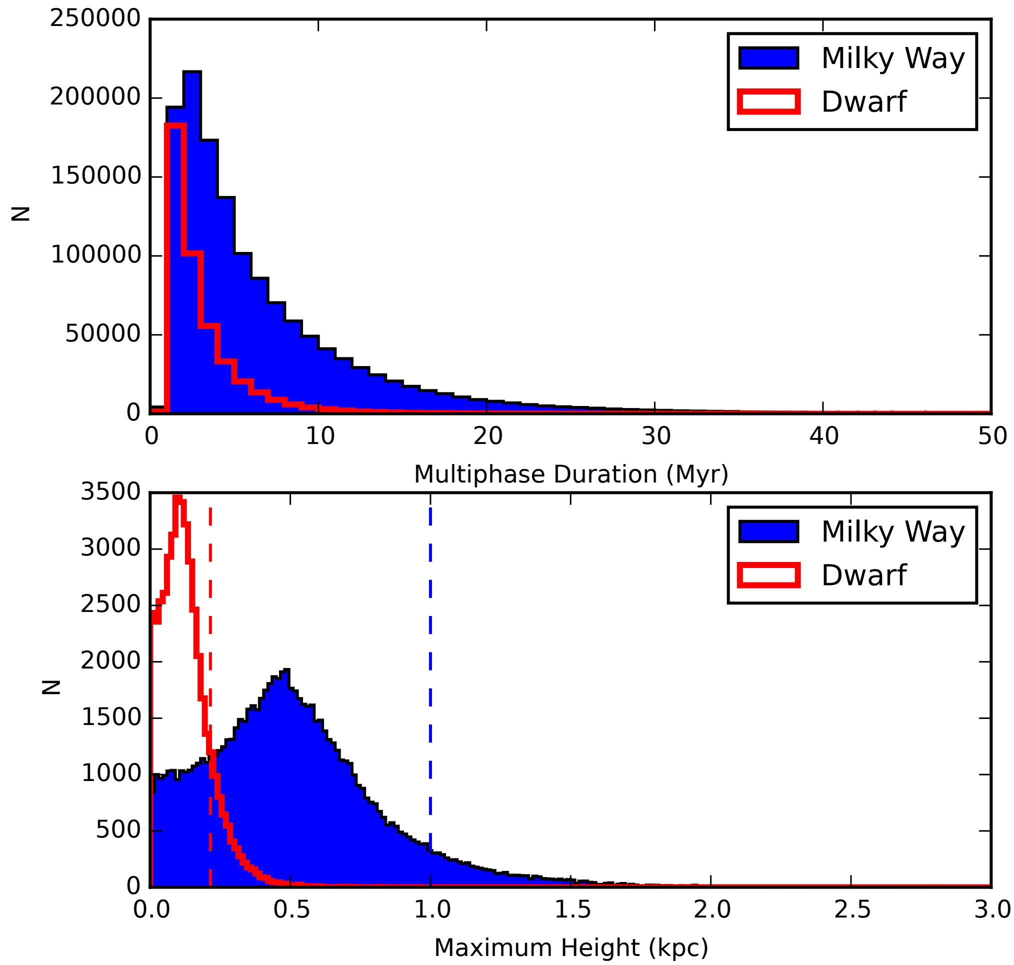

Figure 2.13: Properties of multiphase particles in the galaxy simulations. The top figure shows duration of multiphase state for particles in both galaxy simulations. Particles that are in the multiphase state more than once (convert back to single phase, cool, and then receive feedback again) have each time they are multiphase counted separately. The bottom figure shows maximum heights reached by particles in the multiphase state. For each particle that is ever in the multiphase state, the maximum height it reaches *while still multiphase* is shown above for both galaxy simulations. Dashed lines show scale heights at 10^4 K for each of the two simulations.

moving away from the galaxy between a planar region 5 scale heights (5kpc for the Milky Way, 1.13kpc for the dwarf) above and below the disc, and 0.5 scale heights thick. The outflow rate $\dot{M}$ is simply the total momentum of outflowing particles (particles returning on fountains are excluded) passing through this region divided by the thickness of the region. The average outflow velocity $< v_{\rm out} >$ is just the mean velocity of these same particles.

The superbubble feedback method, as shown in figure 2.12 (and the SFR shown in figures 2.9 and 2.11), also passes the most basic requirement for a useful feedback model: it is capable of regulating star formation to match observed global star formation efficiencies. This result is a typical outcome for effective feedback models with density-based star formation rates (e.g. Springel & Hernquist, 2003). Note that the simple star formation prescription used for these tests does not have a cut-off at lower surface densities. It is clear in figure 2.9 that the average SFR in the Milky Way is roughly twice as high in the simulation using blastwave feedback as compared to the simulation with superbubble feedback. It is also clear from this figure that outflows in the Milky Way simulation with superbubble feedback contain approximately ten times the mass of outflows driven by blastwave feedback.

2.4 Discussion

It is important to heat the right amount of gas through feedback. This is particularly important if one wishes to examine feedback-driven galactic winds. As figures 2.2 and 2.6 show, the simple cooling-shutoff feedback model produces quite different amounts of hot gas as a function of both resolution and ISM homogeneity. If one underestimates the amount of mass heated by feedback, the winds one drives will be hotter, but contain less mass. In other words, outflows will be faster but contain less mass. If one overestimates the amount of mass, outflows may carry a larger fraction of the galaxy's gas mass, but will be less able to actually remove this gas from the galaxy, either permanently or for a long cycling timescale. Either error will have serious implications for predictions of the effects of outflows on both host galaxies and the intergalactic medium. We have constructed our model such that both the momentum and the amount of hot gas within a superbubble are resolution independent. This is confirmed in figure 2.2 over a range of mass resolutions from $\sim 95M_\odot$ to $5 \times 10^4 M_\odot$. Even in the extreme limit of a one particle superbubble, the results are qualitatively correct and vary less than a factor of 2 from the expected solution.

In fact, for any feedback model that omits thermal conduction or other mixing between the hot interior of a feedback bubble and the surrounding cold shell, the amount of hot mass produced will be set by the resolution of the simulation alone. In fact, figure 2.2 shows this quite clearly. For each resolution, the hot mass produced is roughly constant, simply a product of the simulation mass resolution and the number of particles feedback is shared with. Changing either of these will drastically change the amount of hot gas generated by feedback.

In general, the gas driven in outflows from these galaxies does not move fast enough to escape the galactic halos in either the dwarf and the Milky Way. This is reasonable for star formation rates well below the starburst regime. The majority of gas ejected from both simulations instead cycles between the halo and the disc. This helps moderate star formation in the disc. By 300 Myr, only ~ 1.0 per cent, or roughly 8.4×10^7 $M_\odot$, of the Milky Way gas has been lifted to above 5 scale heights while the dwarf cycles more than a third of its total gas mass, 3.3×10^7 $M_\odot$ into a fountain above 5 scale heights. In both simulations, this cycling induces periodic bursts of star formation and disc outflows.

As figures 2.9 and 2.11 show, the superbubble method results in galaxies with stronger star formation regulation, and more mass-loaded outflows than the well-established blastwave model. For example, the simulation of the Milky Way analog, the star formation rate is lower by a roughly a factor of 2 compared to the blastwave (a point in favour of the superbubble model, since Scannapieco et al. (2012) showed that a cosmological simulation of the Milky Way using blastwave feedback in GASOLINE formed stars at roughly twice the rates observed by Guo et al. (2011)). We also see roughly an order of magnitude more gas ejected from the disc with the superbubble model, as we expect from the results of the single star cluster test, since the production of more hot mass should result in more mass-loaded winds. Interestingly, the mean outflow velocity shows only small differences between the superbubble and blastwave models. This means that even though the outflows driven by the blastwave contain less mass, they do not leave the galaxy any faster, and are no more likely to escape the galactic potential than winds produced in the superbubble simulations.

Our superbubble model is comparable to the model of Dalla Vecchia & Schaye (2012) with a $\Delta T \sim 10^7$ K, somewhat smaller than their fiducial value. Both heat of order 300 $M_\odot$ per SNe. Dalla Vecchia & Schaye (2012) simply relied on a stochastic model to deposit enough energy only when a specified temperature can be reached. Their model suffers from overcooling at cosmological resolutions with densities $n_H > 10\ \mathrm{cm}^{-3}$ as their stochastic model requires the heating of fractional gas particles to yield the temperatures they desire. At moderate resolution, some star forming regions thus experience no feedback and others get strong feedback. The multiphase mechanism can handle resolutions where the initial feedback-heated gas mass is less than a single resolution element, without relying on stochastic feedback.

The superbubble method has a number of distinct advantages over previous feedback methods (cooling shutoffs, constant-temperature stochastic feedback, hydrodynamic decoupling, etc.). The superbubble model introduces no additional free parameters, requiring only the total stellar feedback energy to be specified. The superbubble paradigm can incorporate multiple sources of mechanical luminosity, primarily stellar winds and supernovae, within a single framework. Unlike other methods, the amount of mass heated by feedback is physically motivated: it is the amount of mass evaporated into the hot bubble through thermal conduction. Radiative cooling is suppressed not by simply disabling it (which at best only approximates the long cooling times desired), but by injecting energy into a distinct low density, hot phase. This allows the model to handle high-resolution isolated galaxy simulations as well as lower-resolution cosmological ones.

Another distinct advantage of this method is that it is *local*. Feedback-heated gas needs no knowledge of its environment save the information it has already through hydrodynamic interactions with its neighbours. This allows the method to handle feedback from clustered star formation without any additional changes; gas particles need not know the *total* energy inside a feedback-heated superbubble, which can be difficult to determine in a bubble that is heated by multiple stars and contains many gas particles or cells. Clustered star formation is an important aspect of galactic evolution, and can amplify the effects of feedback by concentrating it on a single region (something done by hand in stochastic, constant temperature feedback models). As resolution in galaxy simulations has been steadily improving, well-resolved clustered star formation is beginning to become a reasonable goal and object of study. The superbubble model will allow feedback from these clusters to behave in a physically correct manner that is insensitive to resolution.

2.4.1 Summary

Stars preferentially form in clusters. Clustered stellar feedback generates superbubbles which are qualitatively different to isolated supernovae. Correctly evolving superbubbles requires the inclusion of thermal conduction. Thermal conduction, acting on very small length scales, evaporates cold material into hot feedback bubbles which must be captured via a sub-grid evaporation model such as the one presented here. At the typical resolutions achievable in galaxy simulations, a sub-grid multiphase treatment is required to accurately follow the evolution of the hot phase. Combining these elements results in a feedback model with several attractive features:

1. Separate hot and cold phases within an unresolved superbubble prevent overcooling without relying on ad-hoc cooling shutoffs
2. Feedback from multiple sources (e.g. star clusters) is combined correctly
3. Feedback gas doesn't unphysically persist in phases with extremely short cooling times
4. Star formation is strongly regulated: at least as effectively as current models with the same feedback energy
5. The feedback can effectively drive outflows
6. Evaporation due to thermal conduction generates the correct amount of hot gas which subsequently determines galactic wind mass-loading
7. For well resolved bubbles, the model no longer relies on its multiphase component and naturally produces superbubbles that behave as predicted
8. The model is insensitive to resolution

Acknowledgements

The analysis was performed using the pynbody package (`https://github.com/pynbody/pynbody`, (Pontzen et al., 2013)) We thank Mordecai-Mark Mac Low for useful conversations regarding this paper. The simulations were performed on the clusters hosted on SHARCNET, part of ComputeCanada. We greatly appreciate the contributions of these computing allocations. James Wadsley and Hugh Couchman thank NSERC for funding support.

Bibliography

Agertz O., Kravtsov A. V., Leitner S. N., Gnedin N. Y., 2013, ApJ, 770, 25

Chabrier G., 2003, PASP, 115, 763

Chevalier R. A., 1974, ApJ, 188, 501

Cowie L. L., McKee C. F., 1977, ApJ, 211, 135

Dalla Vecchia C., Schaye J., 2012, MNRAS, 426, 140

Davé R., Hellsten U., Hernquist L., Katz N., Weinberg D. H., 1998, ApJ, 509, 661

Dehnen W., Aly H., 2012, MNRAS, 425, 1068

Dubois Y., Teyssier R., 2008, A&A, 477, 79

Durier F., Dalla Vecchia C., 2012, MNRAS, 419, 465

Gerritsen J. P. E., 1997, PhD thesis, , Groningen University, the Netherlands, (1997)

Guo Q., et al., 2011, MNRAS, 413, 101

Hopkins P. F., 2013, MNRAS, 428, 2840

Hopkins P. F., Quataert E., Murray N., 2012, MNRAS, 421, 3522

Hu C.-Y., Naab T., Walch S., Moster B. P., Oser L., 2014, preprint, (arXiv:1402.1788)

Katz N., 1992, ApJ, 391, 502

Kawata D., Okamoto T., Gibson B. K., Barnes D. J., Cen R., 2013, MNRAS, 428, 1968

Kim J.-h., Abel T., Agertz O., for the AGORA Collaboration 2013, preprint, (arXiv:1308.2669)

Leitherer C., et al., 1999, ApJS, 123, 3

Mac Low M.-M., McCray R., 1988, ApJ, 324, 776

Machacek M. E., Bryan G. L., Abel T., 2001, ApJ, 548, 509

Marri S., White S. D. M., 2003, MNRAS, 345, 561

McKee C. F., Ostriker J. P., 1977, ApJ, 218, 148

Mihos J. C., Hernquist L., 1994, ApJ, 425, L13

Nath B. B., Shchekinov Y., 2013, ApJ, 777, L12

Navarro J. F., White S. D. M., 1993, MNRAS, 265, 271

Pontzen A., Roškar R., Stinson G., Woods R., 2013, pynbody: N-Body/SPH analysis for python, Astrophysics Source Code Library (ascl:1305.002)

Read J. I., Hayfield T., Agertz O., 2010, MNRAS, 405, 1513

Ritchie B. W., Thomas P. A., 2001, MNRAS, 323, 743

Saitoh T. R., Makino J., 2009, ApJ, 697, L99

Saitoh T. R., Makino J., 2013, ApJ, 768, 44

Scannapieco C., Tissera P. B., White S. D. M., Springel V., 2006, MNRAS, 371, 1125

Scannapieco C., et al., 2012, MNRAS, 423, 1726

Sharma P., Roy A., Nath B. B., Shchekinov Y., 2014, preprint, (arXiv:1402.6695)

Shen S., Wadsley J., Stinson G., 2010, MNRAS, 407, 1581

Silich S. A., Franco J., Palous J., Tenorio-Tagle G., 1996, ApJ, 468, 722

Songaila A., Cowie L. L., 1996, AJ, 112, 335

Springel V., Hernquist L., 2003, MNRAS, 339, 289

Springel V., Di Matteo T., Hernquist L., 2005, MNRAS, 361, 776

Stinson G., Seth A., Katz N., Wadsley J., Governato F., Quinn T., 2006, MNRAS, 373, 1074

Thacker R. J., Couchman H. M. P., 2000, ApJ, 545, 728

Vishniac E. T., 1983, ApJ, 274, 152

Wadsley J. W., Stadel J., Quinn T., 2004, New Astronomy, 9, 137

Weaver R., McCray R., Castor J., Shapiro P., Moore R., 1977, ApJ, 218, 377

Chapter 3

Cosmological Galaxy Evolution with Superbubble Feedback I: Realistic Galaxies with Moderate Feedback

Reprinted from B.W. Keller, J. Wadsley, & H.M.P. Couchman 2015,
MONTHLY NOTICES OF THE ROYAL ASTRONOMICAL SOCIETY *Volume 453, Issue 4, pp. 3499-3509, DOI: 10.1093/mnras/stv1789 Published by Oxford University Press on behalf of the Royal Astronomical Society.*

Abstract

We present the first cosmological galaxy evolved using the modern smoothed particle hydrodynamics (SPH) code GASOLINE2 with superbubble feedback. We show that superbubble-driven galactic outflows powered by Type II supernovae alone can produce L^* galaxies with flat rotation curves with circular velocities ~ 200 km/s, low bulge-to-disc ratios, and stellar mass fractions that match observed values from high redshift to the present. These features are made possible by the high mass loadings generated by the evaporative growth of superbubbles. Outflows are driven extremely effectively at high redshift, expelling gas at early times and preventing overproduction of stars before $z = 2$. Centrally concentrated gas in previous simulations has often led to unrealistically high bulge to total ratios and strongly peaked rotation curves. We show that supernova-powered superbubbles alone can produce galaxies that agree well with observed properties without the need for additional feedback mechanisms or increased feedback energy. We present additional results arising from properly modelled hot feedback.

3.1 Introduction

The theory of galaxy formation is a cornerstone of modern cosmology. ΛCDM accurately predicts the detailed properties of the Cosmic Microwave Background, and the formation of large-scale cosmic structure. Understanding how this yields the small-scale properties of the galaxies we see today and at high redshift requires a good understanding of the physics at play within these individual galaxies: star formation, feedback, gas accretion, etc.

The basic theoretical picture of galaxy formation is now well-established (Rees & Ostriker, 1977; White & Rees, 1978). The complex details are typically probed through both simulation and semi-analytic techniques (Kauffmann et al., 1999; Bower et al., 2006). Simulators typically employ large-scale cosmological boxes and zoomed in simulations, in which regions sliced out of those larger volumes are re-simulated at higher resolution (Katz & White, 1993; Governato et al., 2004; Stinson et al., 2010; Brooks et al., 2011). Recent studies (Dekel & Birnboim, 2006; Woods et al., 2014) have shown that the picture of how gas is fed to galaxies is not simple: cold flows can be funneled along filaments in the cosmic web, bypassing the virial shock and directly supplying gas to the inner galaxy. Gas accretion and expulsion by stellar feedback is fundamental to how galaxies evolve over time, determining not only when and how many stars form, but the kinematic properties of those stars as well.

Stellar feedback has a greater impact than merely regulating star formation by heating the ISM or increasing its turbulence. It has long been understood that the cumulative effects of multiple supernovae can eject gas from the galaxy, powering a galactic outflow or wind (Mathews & Baker, 1971; Larson, 1974). Galactic winds are common in high-redshift galaxies, and can be seen in the nearby Universe in starburst galaxies (See review by Veilleux et al. 2005). The detection of both blue-shifted rest-frame UV absorption in observations of high redshift galaxies (Weiner et al., 2009; Steidel et al., 2010; Martin et al., 2012) along with broadened $H\alpha$ emission lines (Heckman et al., 1987; Genzel et al., 2011; Newman et al., 2012) strongly suggests the presence of hot, outflowing material surrounding these galaxies. Galactic winds appear to be ubiquitous at high-redshift, and are likely a key factor in the evolution of galaxies in the early Universe. Muratov et al. (2015) estimated that mass loadings for winds peaked at roughly $\eta = \frac{\dot{M}_{wind}}{\dot{M}_*} \sim 10$ at high redshift and that a significant fraction of ejected material can escape beyond the virial radius. By ejecting material from a galaxy's disc, and storing it in the hot, gravitationally bound circumgalactic medium (CGM), star formation at high redshift can be strongly regulated, while at the same time providing a reservoir of gas that can be accreted at late times, ensuring that star formation at low redshift can continue (Marasco et al., 2012). How this CGM is created is complex, as it is potentially pierced by cold flows of infalling material, outflows from the central galaxy, and the accretion of dwarf satellites.

The first generations of cosmological simulations including baryonic physics (hydrodynamics, star formation, etc.) suffered from a number of serious problems. Nearly every simulation, regardless of halo mass, produced far too many stars, and tended to form these stars too early (Abadi et al., 2003; Governato et al., 2009; Stinson et al., 2010; Brooks et al., 2011). Simulations of disc galaxies produced bulge dominated galaxies rather than the thin discs we observe. Together with the discrepancies seen between large dark-matter only simulations and observations, it appeared that the standard dark energy + cold dark matter cosmology ΛCDM might need to be modified to adequately explain the properties of both individuals galaxies and populations of galaxies that we see. Scannapieco et al. (2012) showed these problems were ubiquitous among codes, leading simulators to consider a role for stronger feedback. Early feedback models (e.g. Katz & White 1993) tended to deposit the energy of feedback into a poorly-resolved region of the interstellar medium, subjecting it to over-cooling. Stronger feedback can be achieved by limiting cooling or increasing the total energy. It must also ensure that feedback energy couples strongly to the gas. This strong coupling doesn't just heat the ISM, or disrupt only the densest regions, but drives outflows that actively remove gas from the disc of the galaxy. The Aquila comparison of 13 different simulation codes and subgrid physics models (Scannapieco et al., 2012) showed that only those cases with strong outflows could produce galaxies with realistic star formation histories. The outflow models used were somewhat ad hoc and extremely aggressive. The cases that were capable of ejecting sufficient gas from the galaxy disc to moderate the stellar mass of the halo still failed to produce stellar discs and largely shut down low redshift star formation.

Galactic winds have been a part of cosmological galaxy simulations for some time (Springel & Hernquist, 2003), and recent simulations have investigated these winds in detail. Anglés-Alcázar et al. (2014) showed that these winds can dramatically alter the star formation history, kinematics, and morphology of galaxies at redshift 2. By explicitly creating galactic winds with a variety of mass-loadings and wind velocities, they showed that strong winds are essential to producing the gas-rich, extended, and turbulent discs that are typically observed in high redshift star forming galaxies. Unfortunately, without simulations to $z = 0$, interpreting exactly how these high-redshift winds impact present-day galaxies is difficult. If outflowing material falls back onto the galactic disc within a Hubble time, the effects of high-redshift winds may be seen in the form of increased star formation and inflows at low redshift.

A key question remains: What processes set the mass loading and velocity of these winds? Early work tied galactic outflows to the SNe energy (Springel & Hernquist, 2003). Some studies (e.g. Murray et al. 2005; Krumholz & Thompson 2013) have suggested that radiation pressure is needed to drive sufficient galaxy-scale winds. Others argue that galactic winds could be powered by cosmic ray buoyancy (Ipavich, 1975; Breitschwerdt et al., 1991; Socrates et al., 2008).

Today, multiple different models of strong feedback have begun to produce galaxies with the correct number of stars (Aumer et al., 2013), reasonable star formation histories (Stinson et al., 2013; Agertz & Kravtsov, 2015; Munshi et al., 2013), and correct morphologies (Guedes et al., 2011; Brook et al., 2012; Christensen et al., 2014). Unfortunately, many of these successes have come at the cost of increasing complexity in star formation and feedback methods, crude assumptions regarding the physics of the feedback-heated gas and somewhat arbitrary increases in the feedback energy per unit mass in stars.

In many cases, strong feedback simply means more energy. Many modern feedback models augment the energy input from Type II supernovae ($\sim 10^{51}$ erg per star above 8 $M_\odot$), with that arising from stellar winds, UV ionization, supermassive black holes (SMBH), or radiation pressure (Vogelsberger et al., 2013; Agertz & Kravtsov, 2015). Feedback models such as Stinson et al. (2013) group these sources of energy as early stellar feedback. Since the first supernovae occur ~ 4 Myr after star formation, these feedback mechanisms begin depositing feedback before SN-only methods would. Unfortunately, how much energy from these early feedback effects actually couples to the surrounding ISM rather than radiating away is highly uncertain. In fact, even the coupling of comparatively simpler SN feedback still is a matter of some debate. Many new feedback models (Agertz et al., 2013; Aumer et al., 2013; Hopkins, 2013) treat each of these feedback mechanisms explicitly, modelling the input of energy and momentum from each component separately.

In addition to increasing the total amount of energy deposited by stellar feedback, these models often also include components designed to prevent energy from feedback radiating away (a problem discussed thoroughly in Thacker & Couchman 2000). The energy can be prevented from cooling completely for a while (Stinson et al., 2013) or it can be initially placed into a non-cooling reservoir that leaks back into regular thermal energy (Agertz et al., 2013). Alternately, depositing thermal feedback into a sufficiently small mass, allows it to always heat gas to the same high temperature where cooling times are long (Dalla Vecchia & Schaye, 2012). Depositing feedback as kinetic energy avoids initial radiative losses Springel & Hernquist (2003); Agertz et al. (2013); Hopkins (2013).

While these techniques do help solve the overcooling problem, they all come with some drawbacks. Fixed-temperature thermal feedback is stochastic, and requires the additional free parameter of the feedback temperature. Cooling shutoffs completely disable radiative losses, where in nature these losses are suppressed in some regions but can remain strong in others, depending on the structure of the ISM and the clustering of stars. Kinetic feedback is almost always paired with a temporary decoupling of hydrodynamic forces on feedback-accelerated gas. This is necessary to prevent this gas from shock-heating and potentially reintroducing the overcooling problem (as shown by Creasey et al. 2011; Durier & Dalla Vecchia 2012). Decoupling allows winds to escape. However, this makes it impossible to study the detailed behavior of these winds, and how they interact with the ISM. This makes the mass loading an imposed parameter.

Of these methods, Dalla Vecchia & Schaye (2012) showed the interesting result that, for supernovae alone, depositing feedback energy into a pre-specified amount of mass, without any cooling shutoffs, can give reasonable star formation rates and strong galactic outflows in isolated galaxies. Keller et al. (2014) argued that what sets this mass is thermal conduction in superbubbles, and used that mechanism to build a new way of simulating supernovae feedback that lacked the resolution dependence, additional complexity, and ad-hoc additions of many current feedback models. By focusing on superbubbles, and the evaporation of cold gas to determine mass loading, superbubble feedback gives realistic gas behavior, and is effective at both regulating star formation and driving galactic outflows without introducing free parameters.

The original McMaster Unbiased Galaxy Simulations (MUGS; Stinson et al. 2010) showed that with stellar feedback, the observed color-magnitude relationship and Tully-Fisher relation could be produced in simulated L^* galaxies. It failed, however, to produce galaxies with the correct stellar mass fraction and star formation history, overproducing stars over the entire cosmic history, and grossly overproducing them at high redshift. It also produced galaxies with bulge-to-disc fractions larger than those seen in nature, and with sharply peaked rotation curves. Stinson et al. (2013) showed that the addition of early stellar feedback could alleviate most of these problems. That model does not take into account the potentially complex coupling of stellar winds or radiation pressure to the surrounding ISM. Instead, a substantial (fixed) fraction of the stellar bolometric luminosity was applied as feedback heating.

In this paper, we begin first with an overview of the simulation methods used, both gas microphysics and the star formation and feedback techniques. We then present the results of a suite of 4 simulations using an initial condition from the MUGS sample, each generated with different stellar feedback models or energetics. The resulting galaxy properties, as well as the halo evolution are examined over the lifetime of the galaxy. Finally, we discuss how the superbubble-driven outflows change with time, and how they ultimately result in a realistic galaxy at the present epoch.

3.2 Methods

These simulations were run using a modern update to the SPH code GASOLINE (Wadsley et al., 2004), GASOLINE2. The changes in this new code include a subgrid model for turbulent mixing of metals and energy (Shen et al., 2010), and a modified pressure force form similar to that proposed by Ritchie & Thomas (2001) which is functionally equivalent to Hopkins (2013). These changes solve the problems seen in Kelvin-Helmholtz and blob destruction tests with SPH (Agertz et al., 2007). These and other features are discussed in Keller et al. (2014). Accurately modelling mixing in multiphase gas is essential for accurately simulating the ISM and CGM.

3.2.1 Simulations

For this initial study, we have selected the initial conditions from one of the original MUGS galaxies. We selected an intermediate-mass halo, g1536, allowing us to compare to a number of other studies that have examined this particular halo (e.g. Stinson et al. 2013; Woods et al. 2014). At $z = 0$ this halo has a virial mass of 8×10^{11} $M_\odot$ and a spin parameter of 0.017. It had its last major merger at $z = 2.9$. We have a gas mass resolution of $M_{gas} = 2.2 \times 10^5$ M$_\odot$, and use a gravitational softening length of $\epsilon = 312.5$ pc. The details of how this IC was created can be found in Stinson et al. (2010). We choose to focus on a single galaxy for this paper as it allows us to make a direct comparison of the impact feedback physics makes with relatively little expense. Naturally, this limits our ability to comment on population-wide effects. We leave this discussion for a forthcoming paper in which we introduce 17 additional L^* galaxies.

We compare four test cases using the same initial conditions: no stellar feedback (an absolute lower bound for looking at the effects of feedback); superbubble feedback (our fiducial case); blastwave feedback (a cooling-shutoff based method, and the feedback method used in Stinson et al. (2010), first described in Stinson et al. 2006); and superbubble feedback with double the standard feedback energy (2×10^{51} erg per SN). The high feedback energy case uses more feedback than is predicted by Leitherer et al. (1999), but is within the range of feedback energies currently being used in cosmological simulations (Schaye et al., 2015; Agertz & Kravtsov, 2015; Vogelsberger et al., 2013).

Halos were found in each of the cosmological simulations using the Amiga Halo Finder (AHF; Knollmann & Knebe, 2009).

3.2.2 Star Formation and Feedback

Our suite of simulations use a range of different feedback processes. For all of the simulations shown in this paper, we use a common star formation prescription. Stars are formed at a rate proportional to the local free-fall time of gas, such that

$$\dot{\rho}_* = c_* \frac{\rho_{gas}}{t_{ff}} \tag{3.1}$$

For each of these simulations, we used an efficiency parameter $c_* = 0.1$, the value used by Stinson et al. (2013). Stars are allowed to form in a converging flow when gas is cooler than 1.5×10^4 K, and with a density set to that allowed by the gravity resolution, $\rho = M_{gas}/\epsilon^3 = 9.3$ cm^{-3}.

The amount of supernova feedback per unit stellar mass is determined using a Chabrier (2003) IMF. With $\sim 10^{51}$ erg per supernova this gives $\sim 10^{49}$ erg M$_\odot^{-1}$. A notable difference between this simulation and those of Stinson et al. (2013) and others is that we do not include early feedback, processes such as stellar winds and radiation that can inject energy before supernovae occur ~ 4 Myr after the first massive stars form. A primary role for early stellar feedback is to disrupt the densest molecular gas. In these simulations, this dense molecular gas cannot be resolved, never being formed (and thus it does not form or need to be destroyed).

The feedback recipe used in our main simulations is the superbubble method presented in Keller et al. (2014). This method deposits feedback into resolution elements in a brief multi-phase state. These particles each have separate specific energies, masses and densities, for the hot bubble and surrounding cold ISM, which includes the swept up shell. This allows the method to calculate a separate density and cooling time with the respective densities for each phase, rather than the average density of both phases. Multiphase particles are also prevented from forming stars: the average temperature of the two phases is essentially always above our temperature threshold for star formation, and they also rapidly become too diffuse to form stars as well. More details on this method can be found in Keller et al. (2014).

The addition of thermal conduction and evaporation introduces some additional time step constraints in order to ensure the stability of integration. However, since the thermal conduction rate is capped by the saturation imposed by the electron soundspeed, this time step is at worst 1/17 the Courant time step. In fact, we see an overall speedup when using superbubble vs. blastwave feedback, as gas can no longer exist in the regime of high density and temperature (and thus small Courant times). The average computation time per step was $\sim 25\%$ faster using superbubble feedback compared to blastwave feedback. These benefits are dominant late in the run, as the total amount of dense gas becomes larger. We do see some slight increased cost early in the run, with a slowdown of $\sim 50\%$ before z=4. The additional time-step constraints here are similar to the time-step constraints required for other methods as well, such as decoupled kinetic winds (Springel & Hernquist, 2003).

3.2.3 Gas Cooling and Physics

We adopt the same gas cooling physics as a number of past simulations using GASOLINE (Stinson et al., 2013; Keller et al., 2014). The method for cooling we use here was originally presented in Shen et al. (2010). Our simulations use cooling rates from CLOUDY (Ferland et al., 2013), and include a redshift-dependent UV background, Compton cooling, and primordial and metal cooling from 10 to 10^9 K. This sets these simulations apart from many past simulations (Governato et al., 2009; Brook et al.,

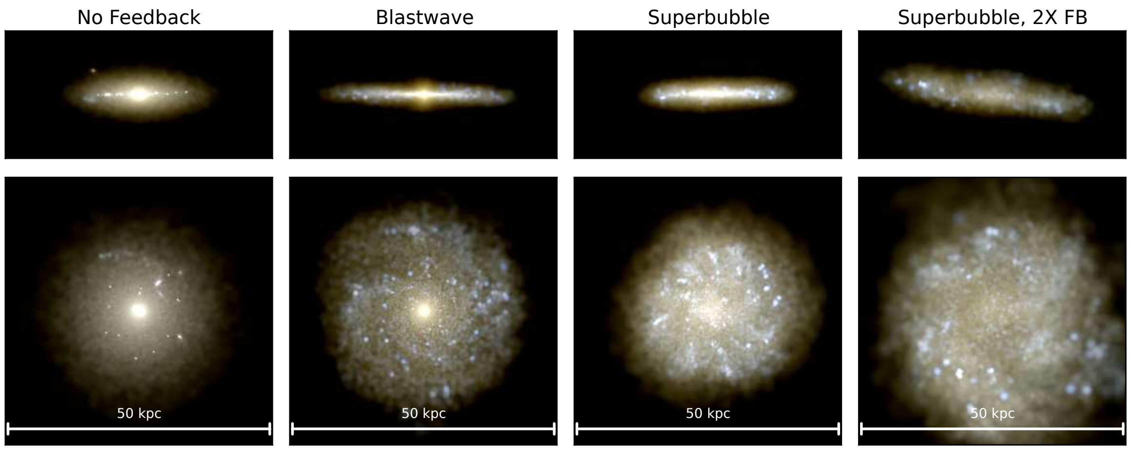

Figure 3.1: Mock stellar image of each galaxy at $z = 0$. The top row shows the galaxies edge-on, while the bottom shows them face-on. The no-feedback case shows very little disc, while the blastwave feedback case has a thin disc with a prominent bulge. The superbubble galaxy appears nearly bulgeless, composed only of a truncated disc. Note also that the superbubble galaxy is bluer than the blastwave or no-feedback galaxies, evidence of a younger stellar population.

2011; Guedes et al., 2011), which did not include high temperature metal cooling. We impose an artificial pressure floor, using a method described by Robertson & Kravtsov (2008) to prevent spurious Jeans fragmentation (as cold, dense gas has both Jeans length and Jeans mass below the resolution limit of our simulation). We also enforce that the minimum SPH smoothing length a particle may have is $\epsilon/4$. This is equivalent to a density floor of 400 cm^{-3} (note that for two-phase superbubble particles, this is the maximum *mean* density). These are comparable to the parameter choices in another recent re-simulation of the MUGS initial conditions, Stinson et al. (2013).

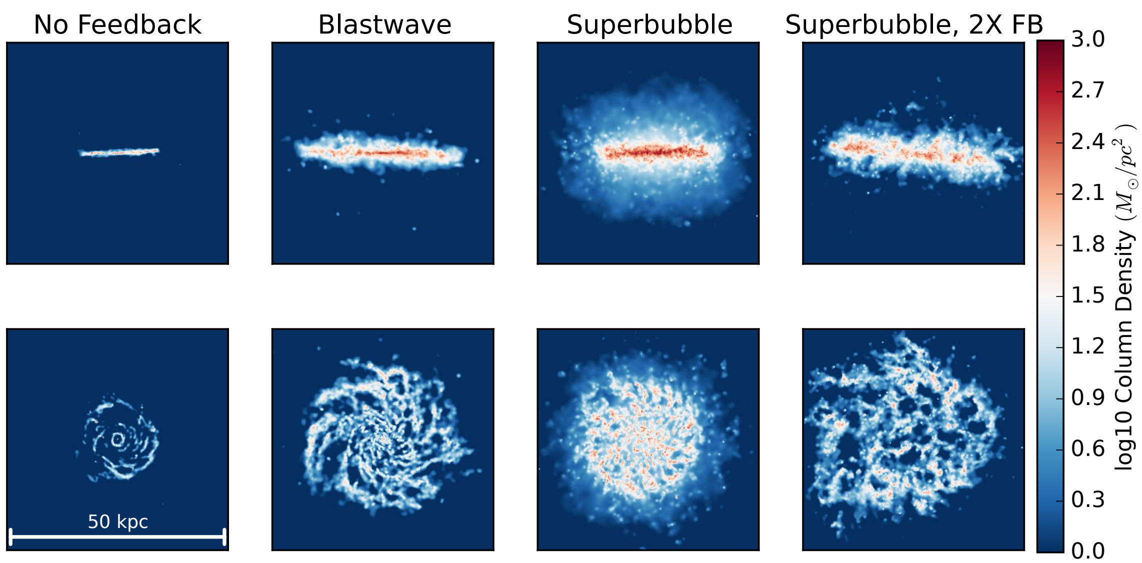

Figure 3.2: HI column density for the four test cases at z=0. The no feedback case has exhausted nearly all of the gas within the disc, leaving only diffuse wisps. The two superbubble cases (especially with doubled supernova energy) have lofted a large amount of gas out of the disc, and some entrained dense clumps can be seen in this outflowing material. The superbubble gas discs are much more flocculent than the blastwave disc, and where the feedback energy is doubled, the disc is strongly disrupted.

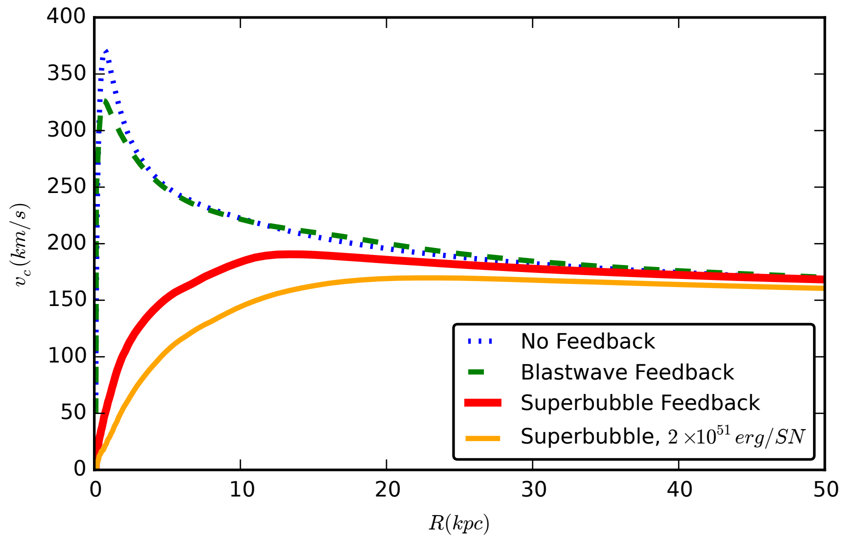

Figure 3.3: Rotation curves for each of our test cases. As is clear, the superbubble cases have much lower central concentrations, giving a a rotation curve that rises to a flat 200 km/s. The peaked rotation curves in the cases with blastwave or no feedback are a result of their failure to remove low angular momentum gas at high redshift, giving bulge-dominated, centrally concentrated galaxies.

3.3 Results

3.3.1 Redshift zero Disc Properties

As can be seen in Figure 3.1, the galaxy produced with superbubble feedback is disc-dominated and blue. The stellar disc in the case without feedback is nearly non-existent, with an ellipsoidal morphology. The superbubble disc appears somewhat thicker and truncated compared to the disc produced with blastwave feedback. The truncation can be seen in the reduced stellar scale length of the superbubble galaxy, 2.9 kpc vs. 3.8 kpc for the superbubble vs. blastwave galaxies. The thickening appears to be quantitatively insignificant, however, as both discs have stellar scale heights of

Simulation	M_{vir}	M_{gas}	M_{star}	$M_{bary,0.1vir}$	M_{bulge}	M_{disc}
No Feedback	7.94×10^{11}	6.21×10^{10}	7.42×10^{10}	8.09×10^{10}	9.34×10^{9}	2.88×10^{10}
Blastwave Feedback	7.99×10^{11}	8.05×10^{10}	5.11×10^{10}	7.94×10^{10}	8.09×10^{9}	1.75×10^{10}
Superbubble Feedback	8.02×10^{11}	1.19×10^{11}	1.84×10^{10}	6.25×10^{10}	1.14×10^{9}	1.15×10^{10}
Superbubble, $2\times10^{51}erg/SN$	7.96×10^{11}	1.20×10^{11}	1.09×10^{10}	4.92×10^{10}	5.96×10^{8}	6.98×10^{9}

Table 3.1: Halo components at $z = 0$. M_{disc} and M_{bulge} are the determined by the angular momentum of the stars (as detailed below). All masses are in $M_\odot$.

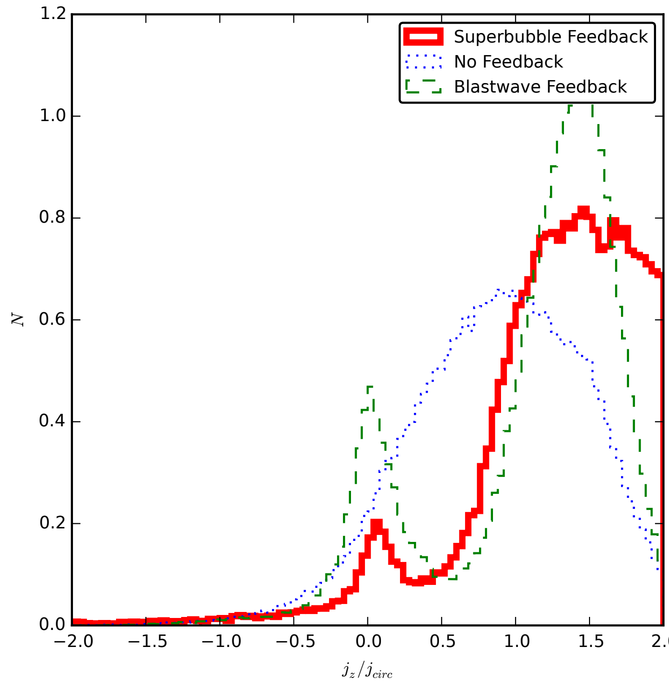

Figure 3.4: Histogram of stellar orbit circularity. The bimodal distribution shows the bulge component, with a circularity near 0, and the disc component, with a circularity near 1. Note that without feedback, this bimodality disappears, as the galaxy morphology becomes spheroidal. The values here are normalized so that each curve has a total integral of unity. As is clear, very few stars produced in a galaxy with superbubble feedback have low angular momentum, giving us a disc-dominated galaxy.

0.9 kpc This may be due to the the disc being disrupted at large radii, where the surface densities are lower, allowing superbubbles to grow larger and escape more easily. The increased feedback case is interestingly somewhat tilted compared to the rotation of the halo as a whole.

The gas component of this galaxy can be seen in Figure 3.2. The superbubble feedback is clearly much more effective at ejecting gas from the disc, creating a halo of clumpy HI gas. In the doubled feedback case, the disc is heavily disrupted, with no spiral structure visible in either the stellar or gas density images. Thus the larger stellar disc is directly related to a more extended gaseous disk.

The rotation curve in Figure 3.3 shows that this ejection also gives a flattened rotation curve without the central peak seen in simulations with blastwave or no feedback. This tells us that the mass distribution is much less centrally concentrated when

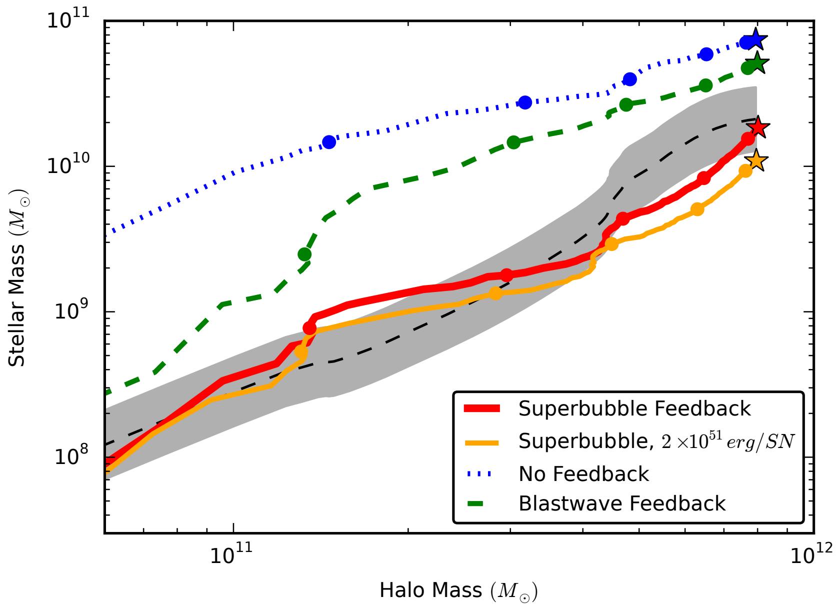

Figure 3.5: Stellar mass growth as a function of the total halo mass. The grey band and black dashed curve show mean values and uncertainties from the abundance matching results of Behroozi et al. (2013). The points show values at redshifts 3,2,1,0.5, and 0.1. The stars show the final values at redshift 0. For essentially the entire evolution of the halo, both the no feedback galaxy and the blastwave galaxy overproduce stars.

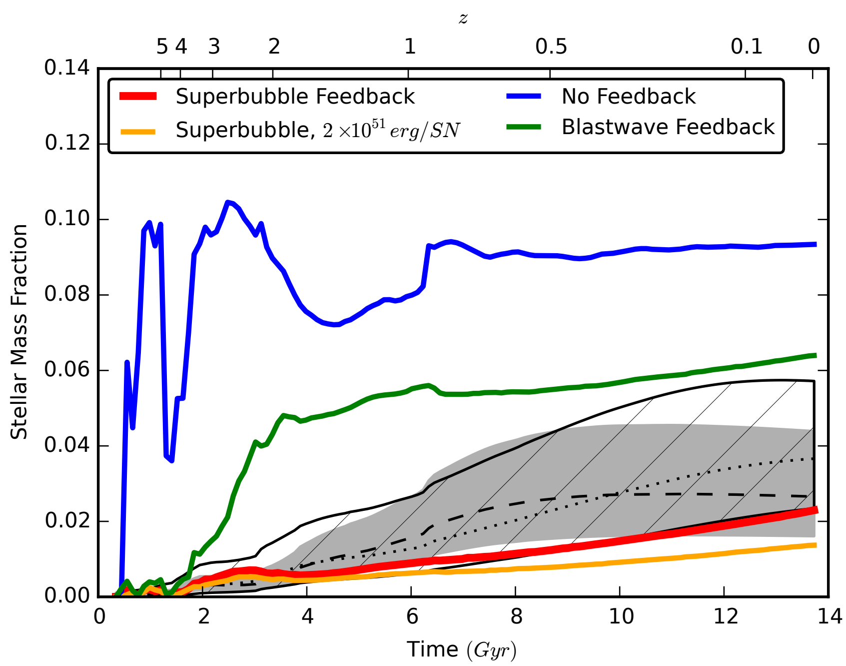

Figure 3.6: Stellar mass fraction as a function of time/redshift. As in figure 3.5, only the fiducial superbubble run produces stellar mass fractions within observed uncertainties for the entire history of the halo. The grey band is as in figure 3.5, and here we also show, in the hatched region with the dotted curve, values and uncertainties from Moster et al. (2013). The dip that can be observed in the no feedback case at high redshift come from the growth of the halo, as it accretes dark matter dominated dwarves.

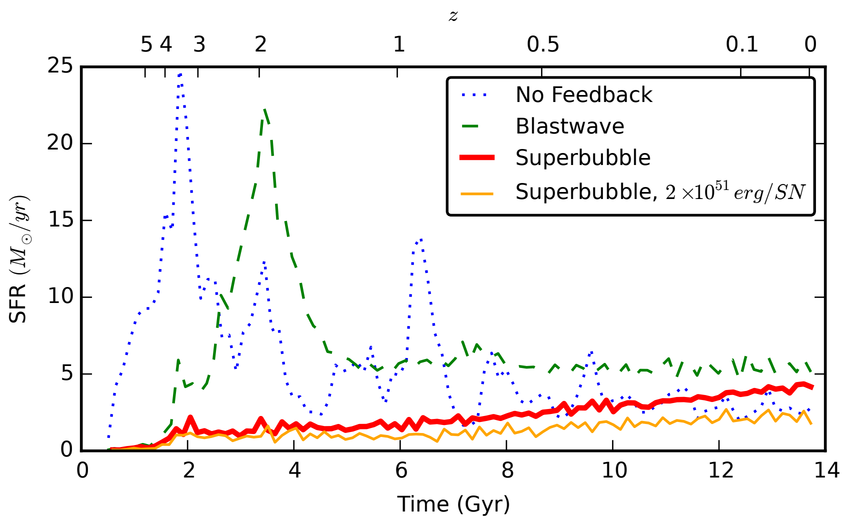

Figure 3.7: Star formation rates for all 4 simulations. The low star formation rate seen after $z = 1$ in the no feedback case is due simply to the high z star formation consuming most of the available gas.

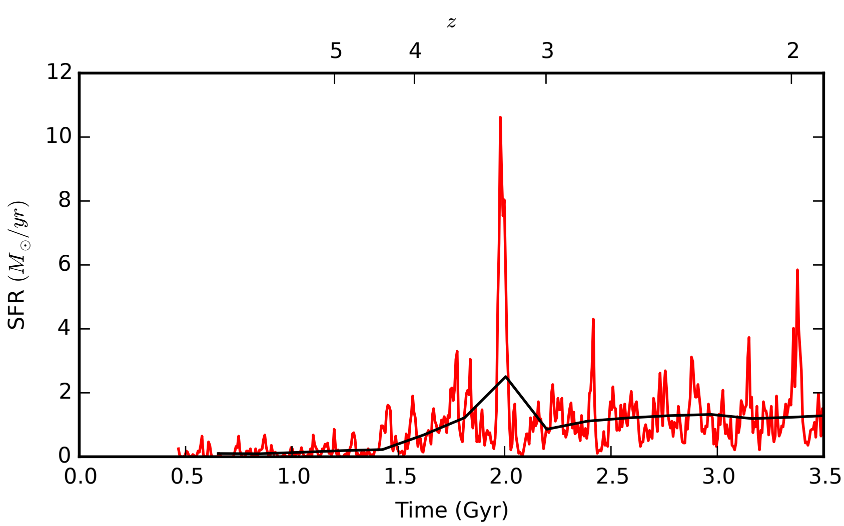

Figure 3.8: Star formation rate up to $z = 2$ for our superbubble galaxy. As is clear, when sampled on short (7 Myr) timescales, the star formation rate in the superbubble galaxy is characterized by strong bursts, despite its quiescent behavior averaged over longer timescales.

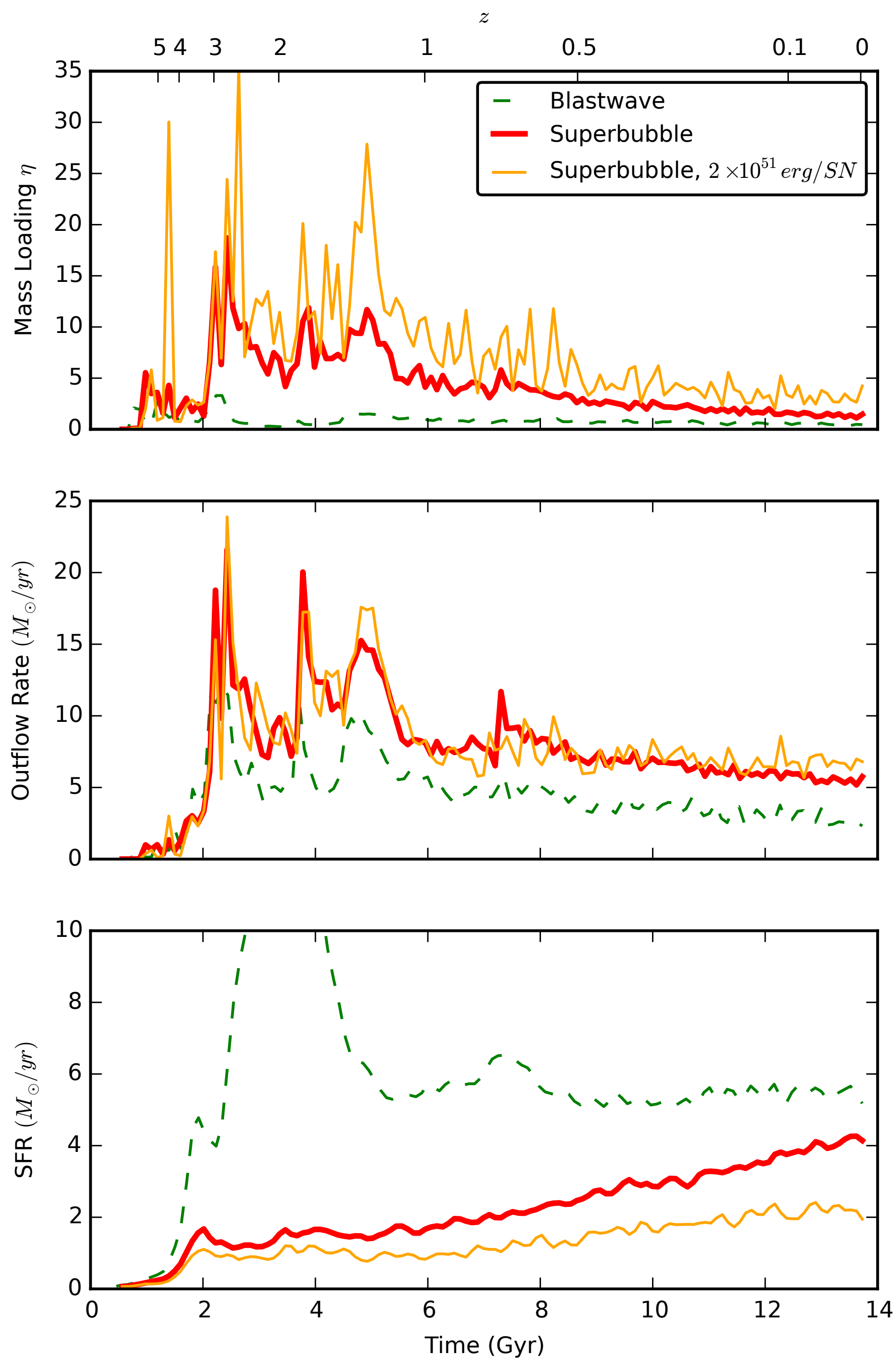

Figure 3.9: Galactic wind mass-loading and outflow rates for each feedback model. As is clear, superbubble feedback powers winds with significantly higher mass-loadings, and, despite forming less than half as many stars the blastwave galaxy, results in more total outflowing gas. This is key to the regulatory power of superbubbles. Despite the peak in outflow rate in the blastwave case between $z = 4-1.5$, the massively increased star formation rate seen in the the smoothed SFR during this time (bottom plot) means that the mass-loadings never go above 5, and baryon expulsion is inefficient.

superbubble feedback is used, more evidence that superbubble feedback is effective in preventing bulge formation.

One of the primary problems in older simulations was a much larger bulge-to-total fraction based on a kinematic decomposition. We adopt the same kinematic decomposition as the original MUGS study. We calculate, for each star within the halo, a circularity parameter, which is simply the ratio of the specific angular momentum component perpendicular to the disc (j_z) and the specific angular momentum for a perfect circular orbit in the same potential that the star sees j_{circ}. As in the original MUGS study, we identify bulge stars as having $j_z/j_{circ} < 0.7$ and orbital radii of < 5 kpc. We find, using these criteria, that our fiducial B/T ratio at $z = 0$ is 0.09, slightly smaller than the Milky Way's ~ 0.14, and greatly reduced compared to the 0.55 found in the original MUGS paper, and well within the observational constraints from Allen et al. (2006). As these numbers, and the distribution of this circularity parameter found in Figure 3.4 show, the vigorous expulsion of central gas with superbubble feedback is a powerful bulge prevention and destruction mechanism. Each of the 13 samples from the Aquila project (Scannapieco et al., 2012) suffered from either from a bulge-dominated stellar circularity profile, or from a massively peaked (or in some cases simply too high) rotation curve. Even the three cases that managed to produce a reasonable stellar mass fraction (each of these generated strong outflows, either through SMBH feedback or wind decoupling) still failed to produce disc-dominated galaxies. Of their sample, only four cases had more than 40% of the stellar mass in disc stars, but all of these cases massively overproduced stars.

The ejection of gas is evident if we look at the baryon content of the interior part of the halo, where the disc resides, in this case, simply material within $0.1R_{vir},$. With superbubble feedback, the baryon fraction of this inner region is 0.30, reduced from 0.37 without feedback, and 0.35 with blastwave feedback. This means that nearly 20% of the baryons that would be available to form stars have been blown out of the galaxy disc, roughly twice the amount that was removed by the older feedback model. The baryon deficit in the superbubble is comparable to the total stellar mass of the galaxy (the fiducial case has a $1.5 \times 10^{10} M_\odot$ deficit in baryons (compared to the no-feedback case), and a total stellar mass of $1.8 \times 10^{10} M_\odot$).

Of what remain, only 29% of the baryonic mass in the superbubble galaxy disc is in stars, compared to 63% in the blastwave galaxy, and 89% in the no feedback galaxy. The basic properties of each halo can be found in table 3.1.

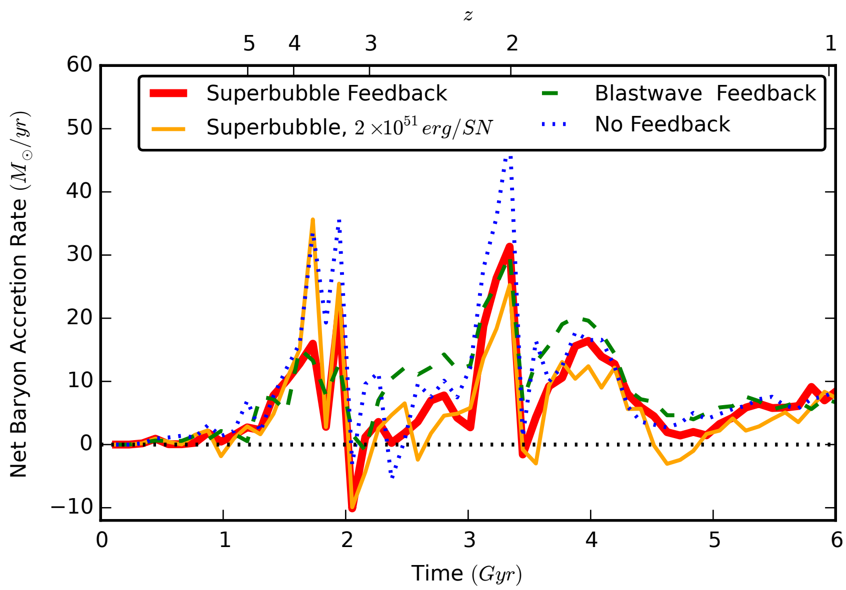

Figure 3.10: Net baryonic accretion (inflow minus outflow of stars and gas) for each test case. It is clear that superbubble feedback expels baryons much more effectively than the blastwave feedback model (although even weak feedback does help somewhat compared to no feedback whatsoever).

3.3.2 Halo Evolution and Star Formation

Ejecting baryons from the disc is essential to producing galaxies that fit the M_*/M_{halo} relationship predicted by Behroozi et al. (2013), Moster et al. (2013) and others. As Figures 3.5 and 3.6 show, the galaxies either lacking feedback or using blastwave feedback alone fail to regulate star formation, diverging from the expected abundance matching stellar mass to halo mass relation at $z \sim 3$ for the blastwave, and before $z = 5$ without feedback, giving galaxies that lie above the abundance-matching relationships over nearly their entire history and mass evolution. With superbubble feedback, this galaxy lies within the range of observed stellar masses over its entire evolution, although on the low side of this range at low redshift. Arbitrarily increasing feedback energies, despite having reasonable star formation rates near $z = 0$, under produces stars for most cosmic history, giving stellar masses *lower* than predicted by abundance matching. Stellar and total masses were calculated for the region inside R_{vir}. As the halo grows over time, brief reductions in the stellar mass fraction can be seen for the no-feedback and blastwave feedback halos in Figure 3.6, simply by the accretion of gas and dark matter that has not yet made it to the galaxy disc. Once

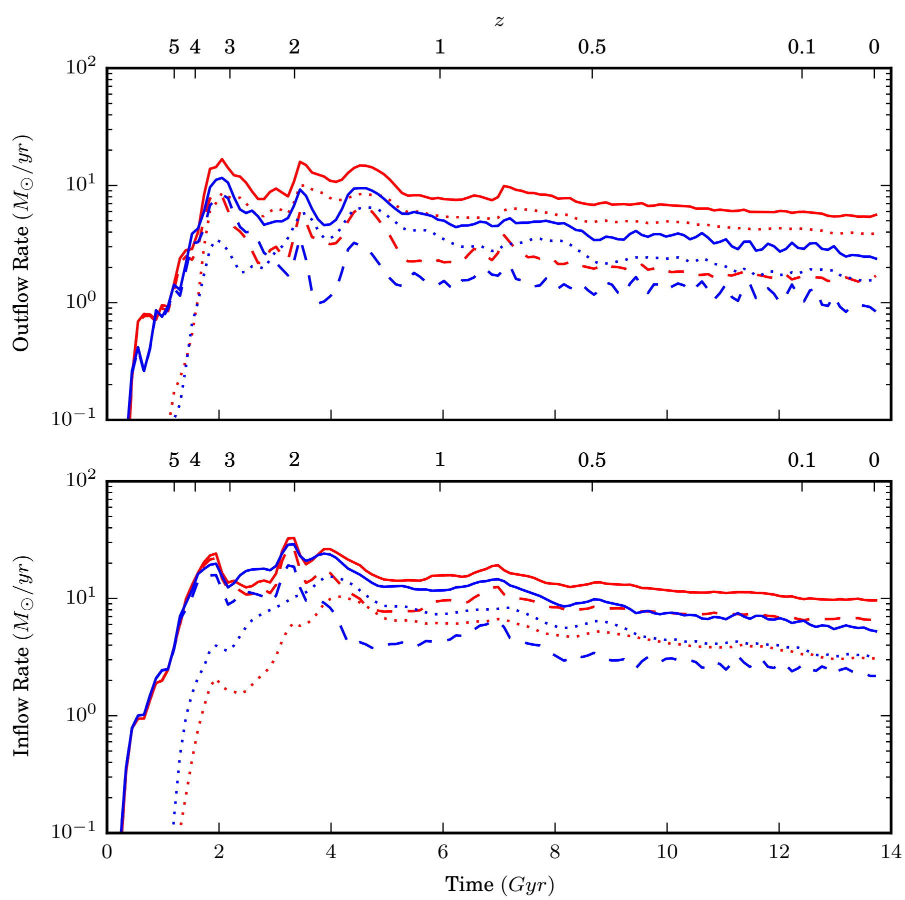

Figure 3.11: Inflow and outflow rates for superbubble (red) and blastwave (blue) run. The solid lines show the total inflow rate, while the dashed and dotted lines show rates for cold and hot gas (above/below 10^5 K) respectively.

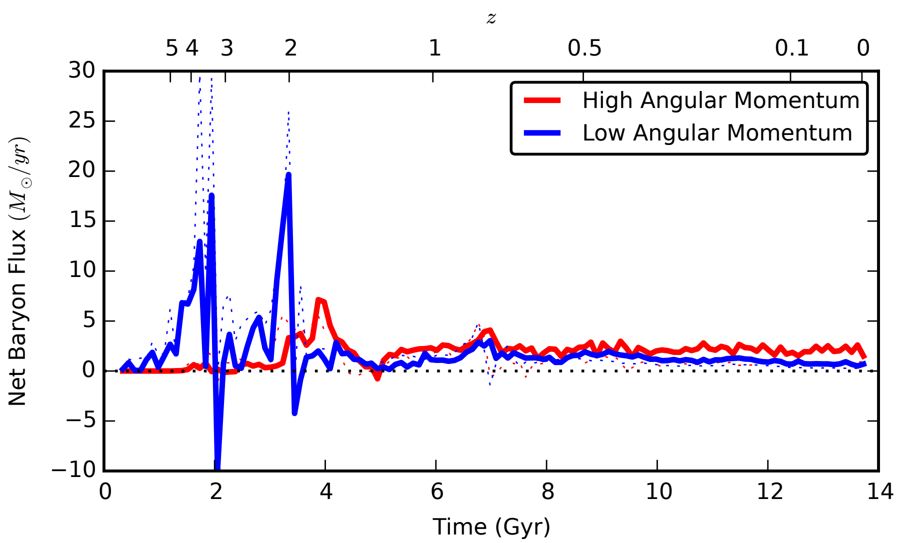

Figure 3.12: In all four test cases, including the fiducial superbubble run shown above by the solid curve, and the no-feedback case shown by the dotted curve, the vast majority of low angular momentum material, with specific angular momentum $j_z < 500$ kpc km/s, is accreted by $z = 2$. The accretion of high angular momentum material, with $j_z > 1500$ kpc km/s rises to peak at $z = 2$, and continues to accrete ~ 2 $\mathrm{M}_\odot$/yr at $z = 0$. As can be seen here, the net flux of low angular momentum material at high redshift is suppressed, while the accretion of high angular momentum material at low redshift is actually *enhanced* by superbubble feedback.

these mergers complete, the stellar fraction rate leaps up once again because of the new supply of gas. The relative flatness in this figure at low redshift is reflected in the relative flatness in the star formation rate, shown in figure 3.7. This is simply a side effect of the massive star formation rates at high redshift: the bulk of star forming gas has been consumed, and thus star formation has slowed.

The star formation rate, in bins of 150 Myr, is shown in Figure 3.7. With no feedback, or blastwave feedback, star formation is extremely vigorous before $z = 2$, slowing at low redshift as gas available for star formation is exhausted. With superbubble feedback, star formation is relatively constant over nearly the entire history of the halo, with only a gradual increase towards $z = 0$. This apparent quiescence is a function of the large time window over which we are averaging our star formation rate. In Figure 3.8, you can see clearly that despite having an average star formation rate of ~ 1 $M_\odot yr^{-1}$, this is punctuated by bursts of star formation of as much as ~ 10 $M_\odot yr^{-1}$. Very similar results were seen in Muratov et al. (2015), where bursts of star formation are followed by peaks in the outflow rates. This burstiness is a important if stellar feedback is to drive galactic winds: to generate large superbubbles, star formation must be clustered in both space and time. Whether these bursts of star formation are able to effectively remove baryons from the disc ultimately depends on the mass loading of the winds that they drive.

3.3.3 Outflow Analysis

Star formation in the disc drives hot, fast-moving outflows from the central star forming regions. These outflows have temperatures of $\sim 2 \times 10^7$ K as they leave the disc, and also entrain some cold material with them. Typically outflow velocities are a few hundred km/s, less than the escape velocity of the halo, but sufficient to propel gas to large radii before it begins to fall in again.

We calculated inflow and outflow rates and velocities by examining particles within a spherical shell, with inner radius $0.1R_{vir}$ and outer radius R_{vir} (giving a shell of thickness $0.9R_{vir}$). We use the $\bar{\rho} = 200\rho_{crit}$ definition for R_{vir}. Particles with $v_r < 0$ are inflowing, while those with $v_r > 0$ are outflowing. Within this shell, the mass flux is determined simply as:

$$\dot{M} = \sum_{r_i \in \mathrm{shell}} \frac{M_i v_i}{0.9R_{vir}} \tag{3.2}$$

As figure 3.9 shows, the outflow behavior of this galaxy is fundamentally different

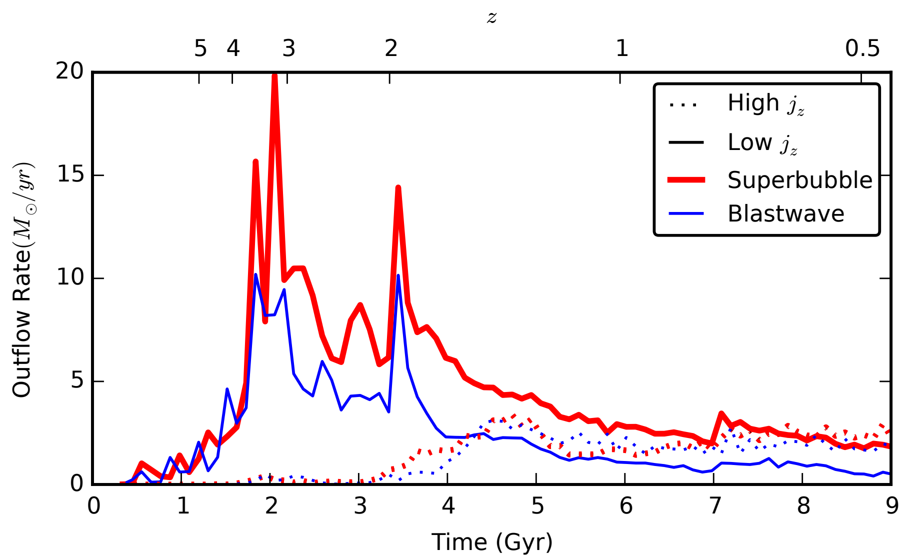

Figure 3.13: High-redshift winds preferentially remove low angular momentum material. As can be seen here, significantly more low angular momentum material is removed by superbubble feedback than by the weaker blastwave feedback, but the amount of ejected high-angular momentum material is roughly equal.

when superbubble feedback is used. The wind mass loading factor $\eta = \dot{M}_{outflow}/\dot{M}_{*}$, a measure of how efficiently feedback is generating outflows, is roughly an order of magnitude larger during the bursts of star formation from $z = 4 - 2$, expelling a large amount of gas from the disc early on. The resulting suppression of high-redshift star formation is key to obtaining the correct stellar mass relation as the halo grows, which is unmistakable in figure 3.5 and 3.6. Evidence of these outflows can be seen in the $z = 0$ column density images in figure 3.2. High-latitude neutral hydrogen from both ejected and infalling material can be seen in the two superbubble cases, but is totally absent otherwise. The smaller amount seen around the high feedback energy case is simply due to this gas being expelled further. The reason superbubbles are so effective at removing mass from the galaxy and thus regulating the stellar mass depends both on the higher outflow rates as well as the lower star formation rates needed to drive these outflows, leading to much larger mass loading factors than the blastwave model can achieve. This is clearly shown in figure 3.9, as the top panel is essentially the middle panel divided by the bottom panel. The outflow rates driven by superbubbles is at most ~ 2 times greater than the blastwave model, but since this is driven by a comparatively tiny amount of star formation, the massloading, η, is

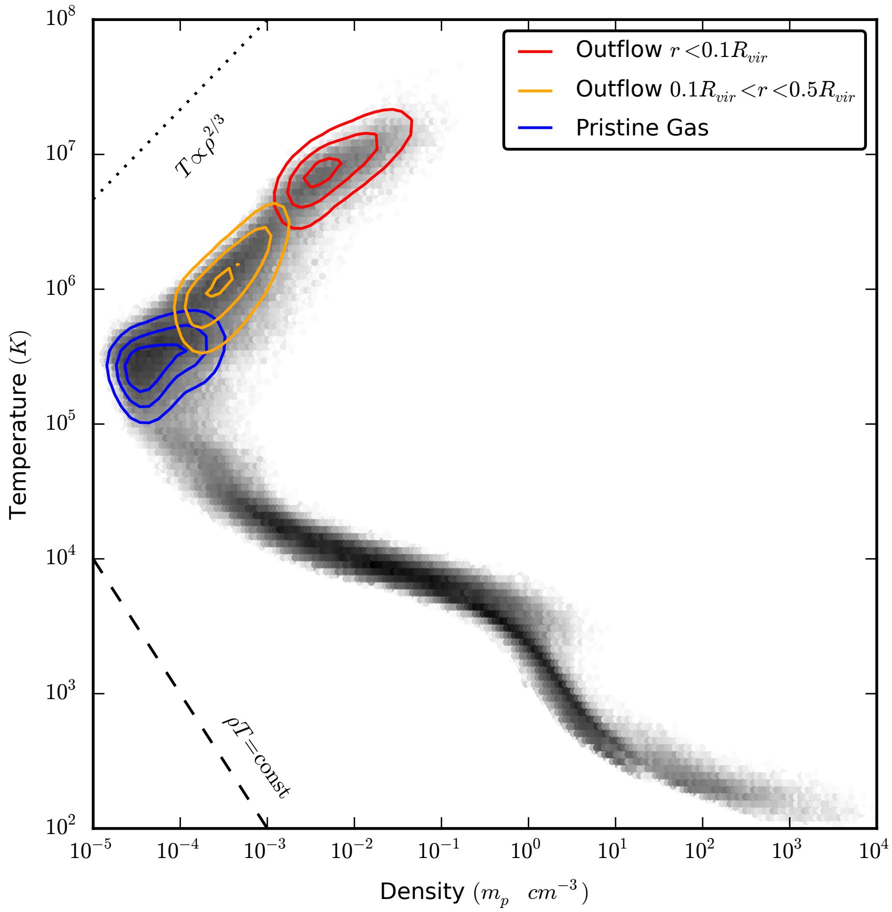

Figure 3.14: Phase diagram of gas in the halo at $z = 0$. The hot, coronal gas with temperatures above 10^5 K contains roughly 40% of the gas mass in the halo. This gas is a mixture of virial-shocked pristine gas, which has never been within the interior $0.1R_{vir}$, and outflowing material ejected from the galaxy. This buoyant, high-entropy gas exits the galaxy at high temperature, and cools adiabatically as it rises through the CGM. The three colored contours show the major components of this hot coronal gas. Pristine gas, never falling within the interior, is shown in blue. Young superbubbles, not yet having broken out of the galaxy, are shown in red. Outflowing material that was once inside the galaxy but is now cooling adiabatically as it rises through the CGM can be seen in orange. The contours show the 1.5%, 1%, and 0.5% levels for the total mass in each cut.

nearly 10 times greater at high redshift. The factor of ~ 2 higher outflow rate is what we would expect from the roughly ~ 2 larger baryon depletion from the superbubble vs. blastwave cases.

The effectiveness of the superbubble-driven galactic winds can be clearly seen in figure 3.10, where the net accretion of stars and gas is greatly reduced by the use of superbubble feedback, resulting at $z = 1$ in a net reduction in the total baryonic mass inside $0.5R_{vir}$ of $\sim 14\%$ vs. blastwave feedback, and $\sim 30\%$ vs. no feedback whatsoever (along with the removal of baryons from the disc discussed earlier). As the outflow rate drops towards $z = 0$, much of this ejected material falls back onto the disc, and the outflows transition to a fountain mode, actually increasing the inflow rate seen compared to the blastwave feedback case in figure 3.11. This increase in the accretion of gas fuels an equivalent increase in star formation, as is seen in figures 3.7 and 3.9.

Figure 3.12 shows that the total accreted gas switches from being dominated by low angular momentum material to being primarily high angular momentum material at $z \approx 2$. Because η is high (~ 10) during this period, low-angular momentum material is preferentially ejected from the galaxy without forming a significant number of stars. These results agree quite well with the results of Muratov et al. (2015), which also found L^* progenitors at $z > 2$ had wind mass loadings $\eta \sim 10$. The preferential ejection of low angular momentum gas is clear in figure 3.13. The small amount of high angular momentum material accreted before $z = 1$ is ejected at an essentially equal rate with or without superbubble-driven winds, but low angular momentum material is propelled into winds at roughly twice the rate when superbubble feedback is taken into account.

The phase diagram in figure 3.14 shows that, as expected, the galaxy contains both a hot halo (in which nearly half of the gas mass can be found), and contains no gas in regions of short cooling time. This behavior was shown previously in the isolated galaxy simulations of Keller et al. (2014). The hot halo gas can be divided into three major components. The coolest component is pristine, virial shocked material that has not ever been accreted (never passed within $0.1R_{vir}$ of the halo center). The hottest gas is actually not yet in the corona, but is the interior of young superbubbles still within the galaxy disc. As this material leaves the disc, it cools adiabatically in the lower pressure environment of the halo, as can be seen in from the $\rho^{2/3}$ adiabatic path it takes through the phase diagram. Detailed analysis of this halo gas, especially in comparison to observations like those of Steidel et al. (2010), will be explored in a future study of a larger sample of L* galaxies.

3.4 Discussion

Past work, especially the Aquila comparison (Scannapieco et al., 2012), has shown that feedback mechanisms which do not remove a large fraction of baryons from galaxy discs fail to produce realistic spiral galaxies. Galaxies simulated without such feedback show more spheroidal stellar distributions, older stellar populations, and more total stellar mass than is observed in nature. Those cases that do manage to expel enough gas to produce reasonable stellar mass fractions still fail to produce the correct stellar kinematics, failing to produce the small bulges characteristic of so many spiral galaxies. These models also rely on mechanisms other than stellar feedback (SMBH heating) or on major numerical contrivances (hydrodynamic decoupling, etc.).

Superbubbles offer a way out of this bind. As was shown in (Keller et al., 2014), evaporation in superbubbles naturally mass load winds with temperatures of $\sim 10^7\ K$, a process that is set by self-regulating thermal conduction. This means that an optimal amount of material is heated above the virial temperature ($1.3 \times 10^6\ K$ for a $8 \times 10^{11}\ M_\odot$ halo). This feedback-heated and highly buoyant hot gas migrates out of the disc, cooling adiabatically while it rises, as is clearly seen in figure 3.14. In fact, as figure 3.6 shows, there may even be room to *reduce* the feedback energy below the fiducial 10^{51} erg/SNe, while still producing reasonable stellar mass fractions. On top of yielding physically-realistic galaxies, superbubble feedback is in fact slightly *less* computationally expensive than blastwave feedback for these simulations, due in part to its elimination of unphysical high density, high temperature gas.

3.4.1 High-Redshift Outflows Determine Galaxy Properties

A major failure of other feedback models is the production of too many stars, too early. Superbubble feedback prevents this by efficiently removing gas from the star forming disc at high redshifts. The high mass loadings from $z = 2 - 4$ means more mass is being expelled by significantly fewer stars. Mass loadings much larger than unity have been observed in both Lyman Break Galaxies at high redshift (Pettini et al., 2002) and in local dwarf starburts (Martin et al., 2002).

Even if a galaxy has the correct stellar mass fraction at $z = 0$, forming too much of your stellar mass at high redshift is problematic for a number of reasons. First, it is known from abundance matching as well as the observations of stellar ages that most stars in L^* galaxies are formed fairly late (e.g. van Dokkum et al. (2013) found $\sim 90\%$ of stars in Milky Way like galaxies formed at $z < 2.5$). Secondly, forming these stars early on means they will be formed primarily in smaller halos that are subsequently accreted, as well as in main halo at small radii (as low angular momentum material is accreted first, as seen in figure 3.12). This results in a stellar distribution too spheroidal and centrally concentrated, as was seen in many older simulations, and here in the rotation curves in figure 3.3 for the blastwave and no feedback test cases.

Because superbubbles drive strong outflows at high redshift, the galaxy is able to preferentially remove low angular momentum gas, as indicated by figure 3.13. This same mechanism was seen in simulations of dwarf galaxies by Brook et al. (2011, 2012). We would suggest that this is a universal requirement for producing galaxies with low central concentrations and small bulges. As Binney et al. (2001) argued, if this gas were to remain within the disc, it would be ultimately form the massive bulge that is seen in our blastwave and no feedback cases, and in numerous other past simulations. If only a third of the baryons removed in the disc of our fiducial case were to instead form bulge stars, it would raise the B/T ratio of the disc to 0.3, making our disc much more bulge dominated than the Milky Way, and putting our results in conflict with Allen et al. (2006). This mechanism (strong, high-redshift outflows), and the fact that it produces strong suppression of star formation at high redshift as well as a small stellar bulge, agrees well with the results of Sales et al. (2012). That study of ~ 100 GIMIC (Crain et al., 2009) galaxies found that those with the smallest B/T ratio also had the largest fraction of stars formed late in the galaxy's history. Strong outflows acting to regulate high redshift star-formation while preserving fuel for late star formation naturally leads to this situation.

The effectiveness of superbubble feedback may help to prevent the growth of a massive stellar bulge via a second mechanism as well. Fall & Efstathiou (1980) showed that the dissipational collapse of hot gas within an extended dark halo can produce galaxies with thin discs. However, Cole et al. (2000) showed that the collisionless processes involved in galaxy mergers can cancel out the net rotation of a galaxy disc and lead to a spheroidal stellar distribution. With superbubble feedback, small dwarves convert very little of their baryonic mass into stars, allowing them to contribute their gas to the primary halo, which then collapses dissipationally.

The heavily mass loaded winds driven by superbubble feedback are not only key to suppressing high-z star formation, but also to providing enough gas at low redshift to continue star formation. The outflows produced by superbubble feedback can easily escape from the lower-mass progenitors of L^* galaxies. Thus it is able to naturally transition from the violent, wind-driving high redshift mode to a more quiescent phase as the galactic gravitational potential and gas surface densities in the disc increase (see the increase in inflow in figure 3.11. These factors suppress outflows, and allow star formation to increase slowly towards $z = 0$.

As the disc is assembled, the disc surface density above the superbubble increases. Thus the hot gas must push past more material and will also entrain more material along with it as shown by the clumps seen in figure 3.2). This slows the outflows compared to those seen at high redshift and moving the galaxy towards a fountain mode. The gas is kicked to relatively low altitudes and then rains back down onto the galactic disc. This effect is probably sensitive to resolution. Our small-scale experiments show that venting of superbubbles is enhanced by a more porous ISM (see Keller et al. 2014 and also Nath & Shchekinov 2013). Poor resolution suppresses this porosity and increases numerical dissipation. Thus better resolution might reduce the puffy appearance in the HI column density and allow strong galactic outflows towards $z = 0$.

3.4.2 Additional Feedback Mechanisms

We have shown that, even at moderate resolution, thermal supernova feedback is sufficient to build a realistic L* galaxy, provided a complete physical feedback model like that of Keller et al. (2014) is used. Thus this work firmly establishes what supernovae and superbubbles can do.

It is still likely that for higher-mass halos ($> 10^{12}$ $M_\odot$), supernovae alone will not be sufffficent to regulate star formation and produce the drop in star formation efficiency seen in Moster et al. (2013); Behroozi et al. (2013). We do not include feedback from SMBH, which is likely to be important for higher-mass galaxies.

Our resolution limits the formation of dense structures in the ISM. The lack of resolved dense gas means that feedback processes involved in disrupting molecular clouds (UV photodissociation, radiation pressure, etc.) are largely irrelevant for these simulations. In fact, since much of the energy from early stellar feedback is consumed in the disruption of the densest clouds in simulations such as this, the addition of this energy may be unrealistic, effectively double counting energy that would have been used to disrupt clouds. Furthermore, high-resolution studies of individual molecular clouds have found that ionizing radiation, despite disrupting these clouds, ultimately only imparts $\lesssim 0.1\%$ of the total radiative luminosity to the gas in the cloud and the surrounding medium in the form of additional thermal and kinetic energy (Dale et al., 2005; Gendelev & Krumholz, 2012; Walch et al., 2012)). Thus, applying even as little as 1% of the radiative luminosity as a source of feedback in a simulation that does not resolve structure within molecular clouds is likely massively overestimating the impact on disc scales.

In sufficiently high-resolution simulations it may be necessary to include small scale feedback mechanisms in order to disrupt clouds before the first SN, allowing the to explode in a lower density environment since, as Mac Low & McCray (1988) showed, the cooling time for superbubbles scales sub-linearly with the inverse density, $t_R \propto n_0^{-8/11}$. Rogers & Pittard (2013) showed that the disruption of high-density clouds by stellar winds prior to the first supernovae can allow as much as 99% of the hot SN ejecta to escape into the surrounding warm ISM, helping to promote the growth of superbubbles that then vent from the galactic disc. In the current work, the densities near the superbubbles are modest and this preprocessing is not required.

3.5 Conclusion

We have shown that supernova feedback alone, with a complete physical superbubble model, is capable of producing an L* galaxy that falls within observational constraints. Superbubbles are a physical mechanism for producing ab initio galactic winds, that ultimately allow for the formation of a galaxy with a realistic star formation history and a negligible stellar bulge.

The key results with respect to galaxy formation are as follows:

- Strong outflows at high redshift are essential to regulating star formation over the total halo history. The vast majority of stars in L* galaxies form after $z \sim 2$. Unless gas is removed from galaxies at high redshift by feedback processes, it will rapidly form stars, yielding discs that are too massive and red at $z = 0$.

- Outflows are important for producing the correct disc kinematics and preventing the formation of excessive bulges. Low angular momentum gas is accreted first as galaxies form, and the pooling of this gas at the center of galaxies can lead to galaxies with sharply peaked rotation curves and unrealistically large bulges, often containing the majority of stars within the galaxy.

- Galaxies simulated without feedback, or with disabled cooling feedback models fail to expel enough of this gas early on, and result in bulge-dominated galaxies with unrealistic stellar mass fractions. The superbubble model, on the other hand, produces strong outflows that ultimately yield realistic galaxies.

- Superbubble feedback naturally yields the sort of outflows that are required for L^* galaxies. The mass-loading & velocity of the winds are set by the hydrodynamics and evaporative mixing, unlike other methods where these values are free parameters.

- Superbubble feedback produces high-redshift outflows that preferentially remove low angular momentum gas, and in so doing, prevents the formation of massive bulges and the associated strongly peaked rotation curves. It does this without also expelling additional high-angular momentum gas, allowing the stellar disc to form while arresting the formation of a bulge.

- These advantages come without any significant additional computational expense, and may in fact be less costly than alternative feedback models.

Superbubbles are effective up to at least L^*. Beyond L^*, we anticipate important roles for SMBH feedback or potentially radiation pressure (see e.g. Hopkins 2013). In the subsequent MUGS2 series of papers, we will show how these effects extend to larger and smaller halos forming in a range of environments.

Acknowledgements

The analysis was performed using the pynbody package (`http://pynbody.github.io/`, (Pontzen et al., 2013)), which was written by Andrew Pontzen in addition to the authors. We thank Fabio Governato, Tom Quinn, Sijing Shen, Greg Stinson, & Rob Thacker for useful conversations regarding this paper. The simulations were performed on the clusters hosted on SCINET, part of ComputeCanada. We greatly appreciate the contributions of these computing allocations. We also thank NSERC for funding supporting this research.

Bibliography

Abadi M. G., Navarro J. F., Steinmetz M., Eke V. R., 2003, ApJ, 591, 499

Agertz O., Kravtsov A. V., 2015, ApJ, 804, 18

Agertz O., et al., 2007, MNRAS, 380, 963

Agertz O., Kravtsov A. V., Leitner S. N., Gnedin N. Y., 2013, ApJ, 770, 25

Allen P. D., Driver S. P., Graham A. W., Cameron E., Liske J., de Propris R., 2006, MNRAS, 371, 2

Anglés-Alcázar D., Davé R., Özel F., Oppenheimer B. D., 2014, ApJ, 782, 84

Aumer M., White S. D. M., Naab T., Scannapieco C., 2013, MNRAS, 434, 3142

Behroozi P. S., Wechsler R. H., Conroy C., 2013, ApJ, 770, 57

Binney J., Gerhard O., Silk J., 2001, MNRAS, 321, 471

Bower R. G., Benson A. J., Malbon R., Helly J. C., Frenk C. S., Baugh C. M., Cole S., Lacey C. G., 2006, MNRAS, 370, 645

Breitschwerdt D., McKenzie J. F., Voelk H. J., 1991, A&A, 245, 79

Brook C. B., et al., 2011, MNRAS, 415, 1051

Brook C. B., Stinson G., Gibson B. K., Roškar R., Wadsley J., Quinn T., 2012, MNRAS, 419, 771

Brooks A. M., et al., 2011, ApJ, 728, 51

Chabrier G., 2003, PASP, 115, 763

Christensen C. R., Brooks A. M., Fisher D. B., Governato F., McCleary J., Quinn T. R., Shen S., Wadsley J., 2014, MNRAS, 440, L51

Cole S., Lacey C. G., Baugh C. M., Frenk C. S., 2000, MNRAS, 319, 168

Crain R. A., et al., 2009, MNRAS, 399, 1773

Creasey P., Theuns T., Bower R. G., Lacey C. G., 2011, MNRAS, 415, 3706

Dale J. E., Bonnell I. A., Clarke C. J., Bate M. R., 2005, MNRAS, 358, 291

Dalla Vecchia C., Schaye J., 2012, MNRAS, 426, 140

Dekel A., Birnboim Y., 2006, MNRAS, 368, 2

Durier F., Dalla Vecchia C., 2012, MNRAS, 419, 465

Fall S. M., Efstathiou G., 1980, MNRAS, 193, 189

Ferland G. J., et al., 2013, RMxAA, 49, 137

Gendelev L., Krumholz M. R., 2012, ApJ, 745, 158

Genzel R., et al., 2011, ApJ, 733, 101

Governato F., et al., 2004, ApJ, 607, 688

Governato F., et al., 2009, MNRAS, 398, 312

Guedes J., Callegari S., Madau P., Mayer L., 2011, ApJ, 742, 76

Heckman T. M., Armus L., Miley G. K., 1987, AJ, 93, 276

Hopkins P. F., 2013, MNRAS, 428, 2840

Ipavich F. M., 1975, ApJ, 196, 107

Katz N., White S. D. M., 1993, ApJ, 412, 455

Kauffmann G., Colberg J. M., Diaferio A., White S. D. M., 1999, MNRAS, 303, 188

Keller B. W., Wadsley J., Benincasa S. M., Couchman H. M. P., 2014, MNRAS, 442, 3013

Knollmann S. R., Knebe A., 2009, ApJS, 182, 608

Krumholz M. R., Thompson T. A., 2013, MNRAS, 434, 2329

Larson R. B., 1974, MNRAS, 169, 229

Leitherer C., et al., 1999, ApJS, 123, 3

Mac Low M.-M., McCray R., 1988, ApJ, 324, 776

Marasco A., Fraternali F., Binney J. J., 2012, MNRAS, 419, 1107

Martin C. L., Kobulnicky H. A., Heckman T. M., 2002, ApJ, 574, 663

Martin C. L., Shapley A. E., Coil A. L., Kornei K. A., Bundy K., Weiner B. J., Noeske K. G., Schiminovich D., 2012, ApJ, 760, 127

Mathews W. G., Baker J. C., 1971, ApJ, 170, 241

Moster B. P., Naab T., White S. D. M., 2013, MNRAS, 428, 3121

Munshi F., et al., 2013, ApJ, 766, 56

Muratov A. L., Kereš D., Faucher-Giguère C.-A., Hopkins P. F., Quataert E., Murray N., 2015, MNRAS, 454, 2691

Murray N., Quataert E., Thompson T. A., 2005, ApJ, 618, 569

Nath B. B., Shchekinov Y., 2013, ApJ, 777, L12

Newman S. F., et al., 2012, ApJ, 761, 43

Pettini M., Rix S. A., Steidel C. C., Adelberger K. L., Hunt M. P., Shapley A. E., 2002, ApJ, 569, 742

Pontzen A., Roškar R., Stinson G., Woods R., 2013, pynbody: N-Body/SPH analysis for python, Astrophysics Source Code Library (ascl:1305.002)

Rees M. J., Ostriker J. P., 1977, MNRAS, 179, 541

Ritchie B. W., Thomas P. A., 2001, MNRAS, 323, 743

Robertson B. E., Kravtsov A. V., 2008, ApJ, 680, 1083

Rogers H., Pittard J. M., 2013, MNRAS, 431, 1337

Sales L. V., Navarro J. F., Theuns T., Schaye J., White S. D. M., Frenk C. S., Crain R. A., Dalla Vecchia C., 2012, MNRAS, 423, 1544

Scannapieco C., et al., 2012, MNRAS, 423, 1726

Schaye J., et al., 2015, MNRAS, 446, 521

Shen S., Wadsley J., Stinson G., 2010, MNRAS, 407, 1581

Socrates A., Davis S. W., Ramirez-Ruiz E., 2008, ApJ, 687, 202

Springel V., Hernquist L., 2003, MNRAS, 339, 289

Steidel C. C., Erb D. K., Shapley A. E., Pettini M., Reddy N., Bogosavljević M., Rudie G. C., Rakic O., 2010, ApJ, 717, 289

Stinson G., Seth A., Katz N., Wadsley J., Governato F., Quinn T., 2006, MNRAS, 373, 1074

Stinson G. S., Bailin J., Couchman H., Wadsley J., Shen S., Nickerson S., Brook C., Quinn T., 2010, MNRAS, 408, 812

Stinson G. S., Brook C., Macciò A. V., Wadsley J., Quinn T. R., Couchman H. M. P., 2013, MNRAS, 428, 129

Thacker R. J., Couchman H. M. P., 2000, ApJ, 545, 728

Veilleux S., Cecil G., Bland-Hawthorn J., 2005, ARAA, 43, 769

Vogelsberger M., Genel S., Sijacki D., Torrey P., Springel V., Hernquist L., 2013, MNRAS, 436, 3031

Wadsley J. W., Stadel J., Quinn T., 2004, New Astronomy, 9, 137

Walch S. K., Whitworth A. P., Bisbas T., Wünsch R., Hubber D., 2012, MNRAS, 427, 625

Weiner B. J., et al., 2009, ApJ, 692, 187

White S. D. M., Rees M. J., 1978, MNRAS, 183, 341

Woods R. M., Wadsley J., Couchman H. M. P., Stinson G., Shen S., 2014, MNRAS, 442, 732

van Dokkum P. G., et al., 2013, ApJ, 771, L35

Chapter 4

Cosmological Galaxy Evolution with Superbubble Feedback II: The Limits of Supernovae

Reprinted from B.W. Keller, J. Wadsley, & H.M.P. Couchman 2016,
MONTHLY NOTICES OF THE ROYAL ASTRONOMICAL SOCIETY *Volume 463, Issue 2, pp. 1431-1445, DOI: 10.1093/mnras/stw2029 Published by Oxford University Press on behalf of the Royal Astronomical Society.*

Abstract

We explore when supernovae can (and cannot) regulate the star formation and bulge growth in galaxies based on a sample of 18 simulated galaxies. The simulations are the first to model feedback superbubbles including evaporation and conduction. These processes determine the mass loadings and wind speeds of galactic outflows. We show that for galaxies with virial masses $> 10^{12}\ \mathrm{M}_{\odot}$, supernovae alone cannot prevent excessive star formation. This occurs due to a shutdown of galactic winds, with wind mass loadings falling from $\eta \sim 10$ to $\eta < 1$. In more massive systems, the ejection of baryons to the circumgalactic medium falters earlier on and the galaxies diverge significantly from observed galaxy scaling relations and morphologies. The decreasing efficiency is due to a deepening potential well preventing gas escape, and is unavoidable if mass-loaded outflows regulate star formation on galactic scales. This implies that non-supernova feedback mechanisms must become dominant for galaxies with stellar masses greater than $\sim 4 \times 10^{10}\ \mathrm{M}_{\odot}$. The runaway growth of the central stellar bulge, strongly linked to black hole growth, suggests that feedback from active galactic nuclei is the likely mechanism. Below this mass, supernovae alone are able to produce a realistic stellar mass fraction, star formation history and disc morphology.

4.1 Introduction

Stellar feedback plays many roles in galaxies. Simply regulating the star formation rate (SFR) within the interstellar medium (ISM) is not enough to produce a realistic galaxy population. The reduced baryon fractions seen in galaxies requires the expulsion of that gas (Mathews & Baker, 1971; Larson, 1974). Matching observed scaling relations, cosmic star formation histories, the stellar mass–metallicity regulation, and the stellar mass function all require the ejection of gas from a galaxy in large-scale outflows (Dekel & Silk, 1986; Erb, 2008; Finlator & Davé, 2008; Peeples & Shankar, 2011; Marasco et al., 2012). Both abundance matching (Behroozi et al., 2013; Moster et al., 2013) and gravitational lensing studies (Hudson et al., 2015) find that no galaxies convert more than $\sim 25\%$ of their initial baryonic mass into stars. The most straight forward explanation for this is the ejection of a significant fraction of the baryons from the galaxy disc.

The observational evidence of galactic outflows is impossible to ignore (a review of both the theory and observations of galactic winds can be found in Veilleux et al. 2005). From intergalactic metals seen in quasar absorption lines (Songaila & Cowie, 1996; Davé et al., 1998; Weiner et al., 2009), to the detection of neutral (Kunth et al., 1998; Morganti et al., 2003), ionized (Heckman et al., 1987; Martin et al., 2012), and molecular (Stark & Carlson, 1984) outflowing gas with outflow velocities $\gg 100\ \mathrm{km\,s^{-1}}$ (Leroy et al., 2015), we can see that galaxies do not merely accrete gas: they eject it as well (a detailed study of gas inflows and outflows can be found in Woods et al. (2014)). In our own Milky Way, X-ray observations have detected $\sim 6 \times 10^{10}\ \mathrm{M_\odot}$ in the $\sim 10^6\ \mathrm{K}$ circumgalactic medium (CGM) (Gupta et al., 2012), comparable in mass to total baryonic mass of the galactic disc.

In Keller et al. (2015), we showed that a correct treatment of superbubbles driven by supernovae (SNe) directly generates strong galactic winds without requiring extra wind models. This was the first time the complete physics of thermal conduction and evaporation required to model superbubbles (see Keller et al. 2014) was employed in galaxy formation simulations. This removes the need for cooling shutoffs, hydrodynamic decoupling, or other purely numerical boosts to the feedback effectiveness and the associated free parameters. These first principles outflows give a stellar mass evolution that matches the abundance matching results (Behroozi et al., 2013). By removing preferentially low-angular momentum gas, these outflows can prevent the growth of a large bulge, producing bulgeless discs like those that are seen in the nearby Universe.

Prior work (Stinson et al., 2013; Hopkins et al., 2014; Agertz & Kravtsov, 2015) has examined the role of outflows in enabling galaxies to regulate their baryon content and match observed relations as a function of their mass. A common outcome is that stellar feedbacks are insufficient for higher mass galaxies. Typically, these works relied on multiple feedbacks and detailed subgrid models with associated free parameters. These additional feedbacks are discussed in more detail in section 2. They did not however, include necessary physics to accurately model superbubbles. Thus the question, what SNe driven outflows can do, has yet to be fully answered. For example, Hopkins et al. (2014) has argued that SNe alone cannot regulate the stellar content of intermediate mass galaxies, let alone the more massive ones.

The primary goal of this work is to examine galaxies and their outflows via a suite of simulated field $L*$ galaxies, the McMaster Unbiased Galaxy Simulations 2 (MUGS2). We begin with an overview of stellar feedback and galactic outflows in section 2. We examine which forms of feedback are most likely to contribute outflows and also discuss alternatives to SNe. In section 3, we describe the MUGS2 sample and simulation methods. We then examine the evolution and final state of the galaxy sample in section 4. As in other work, we find that galaxies more massive than 10^{12} $\mathrm{M}_{\odot}$ deviate from observed relations. In our case, this is where SN-driven winds begin to fail. We find a universal relation between the halo/disc mass and outflow mass loadings. Finally, in section 5, we discuss how stellar mass regulation through SNe fails, how this manifests in the galaxy properties and how this provides strong clues that active galactic nuclei (AGN), powered by accretion on to supermassive black holes (SMBH), must take over the regulation.

4.2 What Launches Galactic Outflows?

The question of what ultimately powers galactic winds has been debated for over half a century, since the first outflows were discovered in M82 (Lynds & Sandage, 1963). Unfortunately, neither AGN nor stellar processes have unambiguous observational signatures in the outflows they produce (Veilleux et al., 2005). To complicate matters further, stellar feedback comes in multiple forms. Disentangling these adds to the uncertainty of how galactic outflows are actually generated. Massive stars deposit energy and momentum in the ISM through ionizing radiation, radiation pressure on dust grains, stellar winds, and ultimately explode as SN. Each of these processes, in principle, has sufficient energy to drive a galactic outflow. Radiation, in particular, has orders of magnitude more energy available than the others (Leitherer et al., 1999). Driving effective galactic winds requires strong coupling to the ISM gas and limited cooling losses so that the terminal velocities are high relative to the escape velocity. We examine the feedback processes individually below.

4.2.1 Stellar feedback

4.2.1.1 Ultraviolet radiation and HII regions

The characteristic temperature of gas photoionized by UV radiation is $\sim 10^4$ K (Krumholz & Matzner, 2009), far lower than the virial temperature of all but the smallest galaxies. For galaxies with halo masses below 10^9 $M_\odot$, photoheating and photoionization by UV radiation strongly limits star formation (Efstathiou, 1992). The characteristic sound speed for gas in HII regions is ~ 10 km/s, similar to characteristic turbulent velocities and escape speeds in molecular clouds. Even large HII regions, such as 30 Doradus, have been observed to have expansion rates of only 25 km/s (Chu & Kennicutt, 1994), significantly less than what is needed to drive even a weak galactic fountain. Thus it is doubtful that UV radiation plays much role in launching galactic-scale outflows.

Simulations by Dale et al. (2012) have shown that HII regions alone are unable to effectively remove gas from their birth clouds, let alone their galaxies but can alter their structure. Thus UV can play a local role in simulations that resolve molecular clouds.

4.2.1.2 Radiation pressure

Radiation pressure on the dust grains in galaxies is a potential driver for galactic outflows. Murray et al. (2011) showed that, assuming spherical symmetry, the most massive star clusters can drive reasonably fast ($v \sim$ hundreds of km/s) outflows. Agertz & Kravtsov (2015) and Hopkins et al. (2014) also found that a combination of SN, stellar winds, and radiation pressure produced a galaxy which matched the abundance-matched stellar mass fractions of Behroozi et al. (2013). However, as Agertz & Kravtsov (2015) noted, and Roškar et al. (2014) examined in detail, these simulated galaxies often displayed unrealistic morphologies, with much thicker discs than would be expected for a normal Milky Way like disc. Roškar et al. (2014) found the addition of radiation pressure using a local 'UV escape probability' model for dust absorption, with a single parameter for the IR dust opacity $\kappa_{\rm IR}$ was able to reduce the stellar mass fraction of a cosmological galaxy with mass comparable to the lighter members of our well-regulated population. However, this required large values of $\kappa_{\rm IR}$, such that the UV radiation coupled to the ISM so strongly that the entire disc was completely disrupted, and the resulting galaxy was completely spheroidal, with stellar scale heights above 3 kpc.

The porosity of the ISM can significantly reduce the mean optical depth of the galaxy, giving photons an escape valve to leave unimpeded (Krumholz & Thompson, 2013). The importance of radiation pressure remains an open question.

4.2.1.3 SNe and stellar winds

Based on energetics alone, it might seem that SN alone could eject gas from even the most massive haloes. A Type II SN releases $\sim 10^{51}$ erg in an ejecta of ~ 10 $\mathrm{M}_\odot$ (Leitherer et al., 1999). This results in a maximum ejecta temperature of $\sim 2\times10^8$ K. This corresponds to the virial temperature for haloes with a mass of $\sim 10^{15}$ $\mathrm{M}_\odot$. This fails to take into account the mixing of SN ejecta with the surrounding ISM. Additionally, if SN ejecta left a galaxy without any mixing or entrainment of additional gas, the largest wind mass loadings seen would be $\eta \sim 0.1$. Such winds would remove metals from the ISM but have little effect on the total baryon content. In order to moderate both star formation and bulge growth, mass loadings of > 10 are necessary. Mixing in cooler ISM material reduces the effective wind temperature to $\sim 10^6$ K if cooling losses are small.

While it is well known that individual SNe experience strong cooling, clustered star formation allows SNe and stellar winds to combine into a superbubble that retains 65 % of its initial injected energy even after the formation of cold shell which then breaks out of the ISM into the halo (Mac Low & McCray, 1988). With low density channels up to 99 % of the energy can escape (Rogers & Pittard, 2013). An important function of the early stellar feedbacks discussed earlier is to clear dense gas around the star cluster to enable the superbubble to escape. However, as discussed previously, this is only valid in a simulation if dense gas is resolved. Thus superbubble feedback can be much more efficient than SN feedback. The physics of evaporation also leads to specific predictions with respect to mass loading and outflow temperatures of order $\sim 10^6$ K (Keller et al., 2014).

The virial temperature of haloes with masses of a few 10^{12} $M_\odot$ is $\sim 10^6$ K. If the wind fluid is cooler than the virial temperature, it will not rise buoyantly out of the disc into the CGM. This suggests SN driven winds become less effective, and may fail to launch altogether somewhere in the mass range of $\sim 10^{12}$ $M_\odot$. The existence of a peak in the star formation efficiency at this same mass, as seen in Behroozi et al. (2013) is strong evidence that this indeed occurring in nature, and that some other feedback mechanism begins to dominate at higher masses. Finding out the if, when and how of this transition is important if we want to know how larger galaxies quench their star formation, and if SN alone can explain the low star formation efficiency in galaxies below this mass.

4.2.2 Other Feedback Mechanisms

4.2.2.1 AGN

The primary non-stellar energy source available for driving galactic outflows is AGN feedback from the growth of SMBHs. The Milky Way's own SMBH has a mass of $M_\bullet \sim 4 \times 10^6$ $M_\odot$ (Meyer et al., 2012). The energy released by its formation is $M_\bullet c^2 \sim 7 \times 10^{60}$ erg. This is significantly greater than the binding energy of the galactic halo ($\sim 10^{59}$ erg). If even a small fraction of this energy couples to the ISM as it is released, it can have a significant disruptive effect. SMBHs are ubiquitous and larger ones are strongly linked to the presence of massive bulges (Magorrian et al., 1998).

Much effort has gone into developing sub-grid models for AGN feedback and SMBH growth, and now AGN feedback is a major component of many large box simulations (e.g., Illustris Sijacki et al. (2015); EAGLE Crain et al. (2015); Rhapsody-G Hahn et al. (2015); Horizon-AGN Dubois et al. (2014)).

4.2.2.2 Cosmic rays

Cosmic rays (CRs) have been proposed as another potential engine for driving outflows (Ipavich, 1975; Breitschwerdt et al., 1991; Everett et al., 2008; Socrates et al., 2008). CRs could be directly linked to SN shocks or shocks within the ISM. CRs may contain as much energy as the thermal and magnetic components of a galaxy (Zweibel & McKee, 1995).

Jubelgas et al. (2008) found CR had little impact on higher mass galaxies. Girichidis et al. (2016) showed that CRs can launch winds with mass loadings of order unity for gas surface densities comparable to the Milky Way. Salem & Bryan (2014) and Booth et al. (2013) found CR driven outflows had even lower mass loadings for Milky Way mass haloes. These results make it doubtful that CRs are centrally important for galactic outflows.

4.3 Methods: MUGS2

The simulations presented here are the new MUGS2 simulations. The original MUGS sample, presented in Stinson et al. (2010), followed the evolution of isolated, Milky Way like disc galaxies using low temperature metal cooling, UV background radiation, and stellar feedback. The new MUGS2 sample includes all of this, plus a number of improvements to the hydrodynamic method, along with the new superbubble feedback model (Keller et al., 2014). This has resulted in significantly different evolution in the MUGS2 sample compared to the original MUGS set, most notably greatly reduced star formation in nearly every galaxy (the original MUGS sample greatly overproduced stars).

These simulations were run using the modern smoothed particle hydrodynamics (SPH) code GASOLINE2, as in Keller et al. (2015, 2014). The changes in this new code include a sub-grid model for turbulent mixing of metals and energy (Shen et al., 2010), and a modified pressure force form similar to that proposed by Ritchie & Thomas (2001), which is functionally equivalent to Hopkins (2013). Details of the star formation and gas physics model can be found in Keller et al. (2014).

4.3.1 Simulation ICs

We adopt the same initial conditions (ICs) that were used in the original Stinson et al. (2010) MUGS sample. These cosmological zoom-in ICs were selected from a $50h^{-1}$ Mpc cube, run (with dark matter only) to $z = 0$. The simulations use a *WMAP3* ΛCDM cosmology, with $H_0 = 73$ km/s/Mpc, $\Omega_M = 0.24$, $\Omega_{\rm bary} = 0.04$, $\Omega_\Lambda = 0.76$, and $\sigma_8 = 0.76$. Galaxies that had halo mass from $5\times10^{11}\,{\rm M}_\odot$ to $2\times10^{12}\,{\rm M}_\odot$

were then selected from the dark matter only run. Isolated galaxies were then selected by choosing only ones which had no neighbours in this mass range within 2.7 Mpc. As galaxies with massive neighbours may be affected by their hot haloes, or radio-mode AGN feedback, we exclude those galaxies to avoid the need to simulate a much larger volume, and to focus on the effects of stellar feedback processes. This resulted in a sample of 276 candidate haloes, of which the final MUGS sample was simply selected at random from this pool. While only nine of these were presented in Stinson et al. (2010), subsequent papers presented the remaining galaxies (Bailin et al., 2010; Nickerson et al., 2011, 2013), and what we present here is the full set of galaxies that were produced for MUGS.

Each of these simulations has a gas mass resolution of $M_{\rm gas} = 2.2 \times 10^5$ M$_\odot$, and uses a gravitational softening length of $\epsilon = 312.5$ pc, and a minimum SPH smoothing length set to 1/4 of this. The total sample presented here consists 18 galaxies, with $z = 0$ virial masses in a range from 3.7×10^{11} M$_\odot$ to 2.1×10^{12} M$_\odot$.

4.3.2 Star Formation

We use a standard Schmidt-law star formation recipe, where the rate is set by the freefall time of gas and an efficiency c_*:

$$\dot{\rho}_* = \frac{c_* \rho}{t_{\rm ff}} = c_* \sqrt{\frac{32G}{3\pi}} \rho^{3/2} \tag{4.1}$$

We used an efficiency of $c_* = 0.05$, as was used for the original MUGS simulations (Stinson et al., 2010) and in Keller et al. (2015). Star formation is only allowed to take place in gas which satisfies three criteria: it has a temperature below 1.5×10^4 K, density above 9.6 cm^{-3} (the density where gravitational softening becomes important), and is in a converging flow ($\nabla \cdot \boldsymbol{v} < 0$). This density threshold is larger than that used in Stinson et al. (2010) (which used 0.1 cm^{-3}), but identical to that used in Stinson et al. (2013). We have used this larger threshold (as Governato et al. 2010 recommends) to better capture the effects of clustered star formation. Aside from this higher star formation threshold, our star formation recipe remains unchanged from the original MUGS sample.

Galaxy ID	M_{vir}	λ'	f_b	$z_{1/2}$	z_{lmm}	M_* (masses	M_{gas} in	M_{central} 10^{10} $M_\odot$)	$SFR_{\mathrm{z=0}}$ ($M_\odot$ yr^{-1})
g7124	36.6	0.039	0.150	0.8	2.1	0.5	5.0	1.8	0.6
g5664	47.7	0.028	0.173	0.8	3.0	0.9	7.3	3.0	1.7
g8893	58.0	0.065	0.170	1.0	0.8	0.7	9.1	2.6	1.0
g1536	64.9	0.029	0.189	1.0	4.0	1.9	10.4	5.2	3.9
g21647	74.4	0.069	0.152	0.2	0.5	1.2	10.1	3.1	2.7
g422	76.2	0.033	0.183	0.8	0.7	1.5	12.4	5.1	3.2
g22437	85.2	0.013	0.192	0.7	2.6	9.0	7.3	11.2	17.9
g22795	85.2	0.009	0.178	1.1	3.8	10.6	4.6	11.7	6.2
g3021	97.8	0.040	0.192	0.6	1.7	3.6	15.1	9.9	15.7
g28547	98.5	0.106	0.186	0.4	0.1	1.6	16.7	4.5	2.7
g19195	101.6	0.039	0.162	0.7	0.7	7.1	9.3	9.7	20.3
g24334	102.2	0.052	0.174	0.5	1.6	2.6	15.3	7.2	6.8
g4720	102.5	0.015	0.192	0.8	1.8	14.2	5.5	14.4	8.3
g4145	119.5	0.033	0.193	0.9	1.4	15.0	8.1	16.9	20.9
g25271	125.5	0.016	0.187	1.1	4.0	15.6	7.9	17.0	9.7
g15784	131.2	0.037	0.186	1.3	7.3	13.0	11.4	17.7	9.6
g15807	203.2	0.026	0.191	1.0	2.5	21.4	17.5	25.4	11.9
g27491	214.7	0.039	0.184	0.7	1.1	18.8	20.8	26.6	17.6

Table 4.1: Redshift 0 properties of the full MUGS2 sample. All masses and particle counts are measured within a R_{vir} sphere centred on the halo, except for M_{central}, which is measured within a 0.1 R_{vir} sphere.

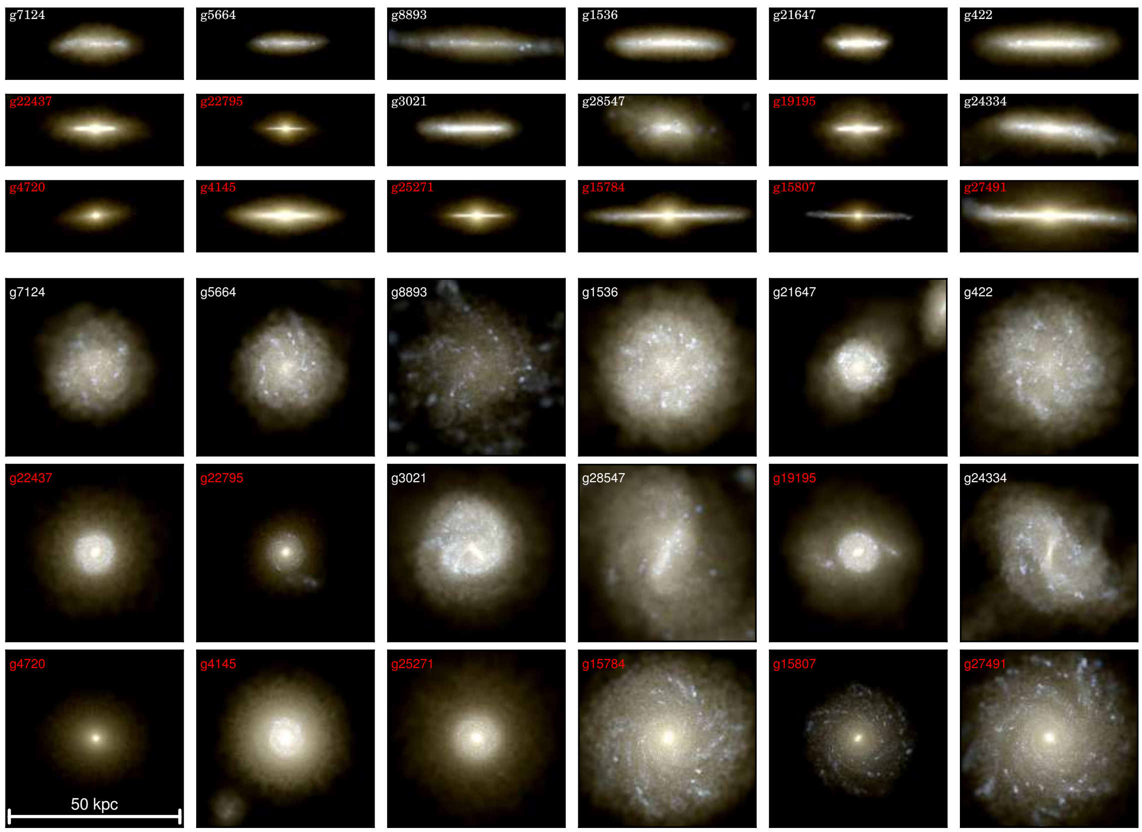

Figure 4.1: Mock optical stellar observations of each MUGS2 galaxy. RGB channels are calculated using Marigo et al. (2008) stellar populations. The top three rows show the galaxies edge on, while the bottom three show the galaxies face on. The galaxies are sorted in order of halo mass, and galaxies that overproduce stars are labelled with red. These images do not include the effects of dust extinction

4.3.3 Superbubble Feedback

We use the superbubble feedback model described in Keller et al. (2014). We briefly summarize the important details below. The model deposits thermal energy and mass into resolution elements in a brief multi-phase state. These particles each have separate specific energies and masses for the hot bubble and cold ISM components, including the swept up shell. This allows the method to calculate a separate density, temperature, and cooling rate for each phase, rather than using the average density and temperature of both phases. Multiphase particles are also prevented from forming stars if the average temperature of the two phases is above our temperature threshold for star formation. The amount of SN feedback per unit stellar mass is determined using a Chabrier (2003) IMF.

In Keller et al. (2014), we demonstrated that superbubble feedback could produce significantly more mass-loaded outflows and reduced star formation in simulations of isolated disc galaxies, compared to the older (Stinson et al., 2006) blastwave model. The effectiveness of this older model is highly dependent on numerical parameter choices. In Keller et al. (2015) (which examined the first simulation of the full MUGS2 sample we present here) we chose parameters to match the original MUGS, and the MAGICC runs of Stinson et al. (2013). We also showed how the ISM phase behaviour in superbubble-regulated galaxy behaved in a much more physically reasonable way than in a galaxy regulated with single phases. Keller et al. (2015) showed that in a cosmological galaxy (one of the same galaxies presented here in the MUGS2 sample, g1536) superbubble feedback resulted in high mass loadings $\eta \sim 10$ for galactic outflows from $z \sim 4$-2, which then fell to $\eta \sim 1$ at low redshift, producing a galaxy with a realistic star formation history and no significant bulge component, without the need for additional feedback mechanisms, or greater feedback energies than what are provided for simply by SN alone. We also showed that this comes without additional computational cost, or the addition of any new free parameters/tuning.

Aside from a different star formation density and temperature threshold, the star formation and feedback recipes used here are identical to those used in Keller et al. (2014). One of our sample, g1536, was presented earlier in Keller et al. (2015).

4.3.4 Comparison to Other Feedback Models

With $\sim 10^{51}$ erg coupled to the ISM per SN this gives 1.08×10^{49} erg $\mathrm{M_\odot}^{-1}$ for the full stellar population. Comparing this injection rate to other 'modern' feedback methods, we typically are injecting much less energy (and no momentum, which is generated for us simply through pressure work and the hydrodynamic solver). For example, the Illustris simulations (Vogelsberger et al., 2014b) use the Springel & Hernquist (2003) ISM model, with a Chabrier (2003) IMF, giving a total heating rate of 1.73×10^{49} erg $\mathrm{M_\odot}^{-1}$, which along with the 1.09×10^{51} erg per SN injected for the kinetic wind model, gives a total heating rate from SNII of 3.6×10^{49} erg $\mathrm{M_\odot}^{-1}$. The kinetic winds have their hydrodynamics decoupled from the surrounding ISM, ensuring no losses from shock-heating and radiative cooling (see Vogelsberger et al. 2013, 2014a for more details on the Illustris feedback model).

The EAGLE simulations (Crain et al., 2015) use a purely thermal injection for SNII feedback. The energy per SN depends on both the local density and metallicity of the gas that feedback is deposited in, determined using equation 4.2.

$$E_{\mathrm{SN}} = 0.3 + \frac{2.7}{1 + \left(\frac{Z}{0.1\,\mathrm{Z_\odot}}\right)^{0.87} \left(\frac{n_H}{0.67\mathrm{cm}^{-3}}\right)^{-0.87}} \tag{4.2}$$

This gives a total SNII energy of 3×10^{50} erg in the limit of infinite metallicity or zero density, and 3×10^{51} erg in the limit of zero metallicity or infinite density. The injection rate is thus 5.2×10^{48} erg $\mathrm{M_\odot}^{-1}$ to 5.2×10^{49} erg $\mathrm{M_\odot}^{-1}$, depending on the local gas properties. Both the EAGLE and Illustris simulations also include feedback from AGN.

The FIRE Simulations (Hopkins et al., 2014) use a number of mechanisms for stellar feedback, described in Hopkins et al. (2011), Hopkins et al. (2012a), and Hopkins et al. (2012b). This includes radiation pressure, SNe, stellar winds, photoionization, and photoelectric heating. The FIRE simulations assume a slightly less top-heavy (Kroupa & Weidner, 2003) IMF. Radiation pressure is calculated both as a local deposition of momentum, along with a treatment for long-range radiation pressure from escaped photons. The local momentum deposition is calculated simply using the optical/UV luminosity and an estimated optical depth for IR scattering: $\dot{\boldsymbol{P}}_{\boldsymbol{rad}} = (1 + \tau_{\mathrm{IR}})L/c$. For this IMF, this gives a total optical/UV energy, integrated over the 1 Gyr, of 2.25×10^{51} erg$\mathrm{M_\odot}^{-1}$. Naturally, the more mass this is deposited into the lower the total kinetic energy. This is, though, the absolute upper limit of energy available for radiation pressure. SNe energy and stellar winds are deposited either as thermal energy, with a total energy of 2.2×10^{49} erg ${\rm M_\odot}^{-1}$, or as momentum in the case when the cooling radius is unresolved. The photoionization model in FIRE, described in Hopkins et al. (2012a) uses the ionizing photon rate from Leitherer et al. (1999) to ionize an equivalent number of neutral hydrogen atoms. This gas is heated to, and disallowed to cool below, $T_{HI} = 10^4\ K$ in the current timestep if the ionization rate is greater than the recombination rate. The total integrated ionizing photon number is $N_{\rm ion} = 6.6 \times 10^{61}\ {\rm M_\odot}^{-1}$. We can estimate the maximum energy injected by this photoionization model as $E_{\rm ion} = \frac{3}{2} N_{\rm ion} k_B T_{HI} = 1.4 \times 10^{50}$ erg ${\rm M_\odot}^{-1}$. Summed, the total feedback energy available in the FIRE simulations is 2.41×10^{51} erg ${\rm M_\odot}^{-1}$. It should be noted that this is of course an upper limit, and the algorithms used for FIRE have both local physical and numerical dependencies that can make the actual values significantly lower than this. Determining the exact amount of energy typically deposited is difficult given these complexities.

High-resolution simulations of molecular cloud disruption by radiation pressure (Dale et al., 2005; Gendelev & Krumholz, 2012; Walch et al., 2012) have found that $\lesssim 0.1\%$ of the radiative luminosity couples to the ISM around the cloud in the form of momentum or thermal energy. Instead, as the simulations of Rogers & Pittard (2013) showed, the energy release by stellar winds prior to the first SN instead disrupt the densest gas, producing channels that allow SN to detonate in a less dense environment, where cooling times are longer. Thus, in simulations such as these which do not resolve dense molecular gas, including the effects of radiation pressure and stellar winds likely overestimate their effect, as the dense gas whose disruption absorbs their energies is not present in the simulation.

4.4 Results

4.4.1 Redshift zero properties

The general properties of each galaxy at $z = 0$ can be found in Table 4.1. λ' is the dimensionless spin parameter of the halo, defined by Bullock et al. (2001) as $\lambda' = J/\sqrt{2GM_{\rm vir}^3 R_{\rm vir}}$. f_b is the baryon fraction of the halo. $z_{1/2}$ and $z_{\rm lmm}$ are the redshifts at which the halo reaches half of its final mass, and the redshift of last major

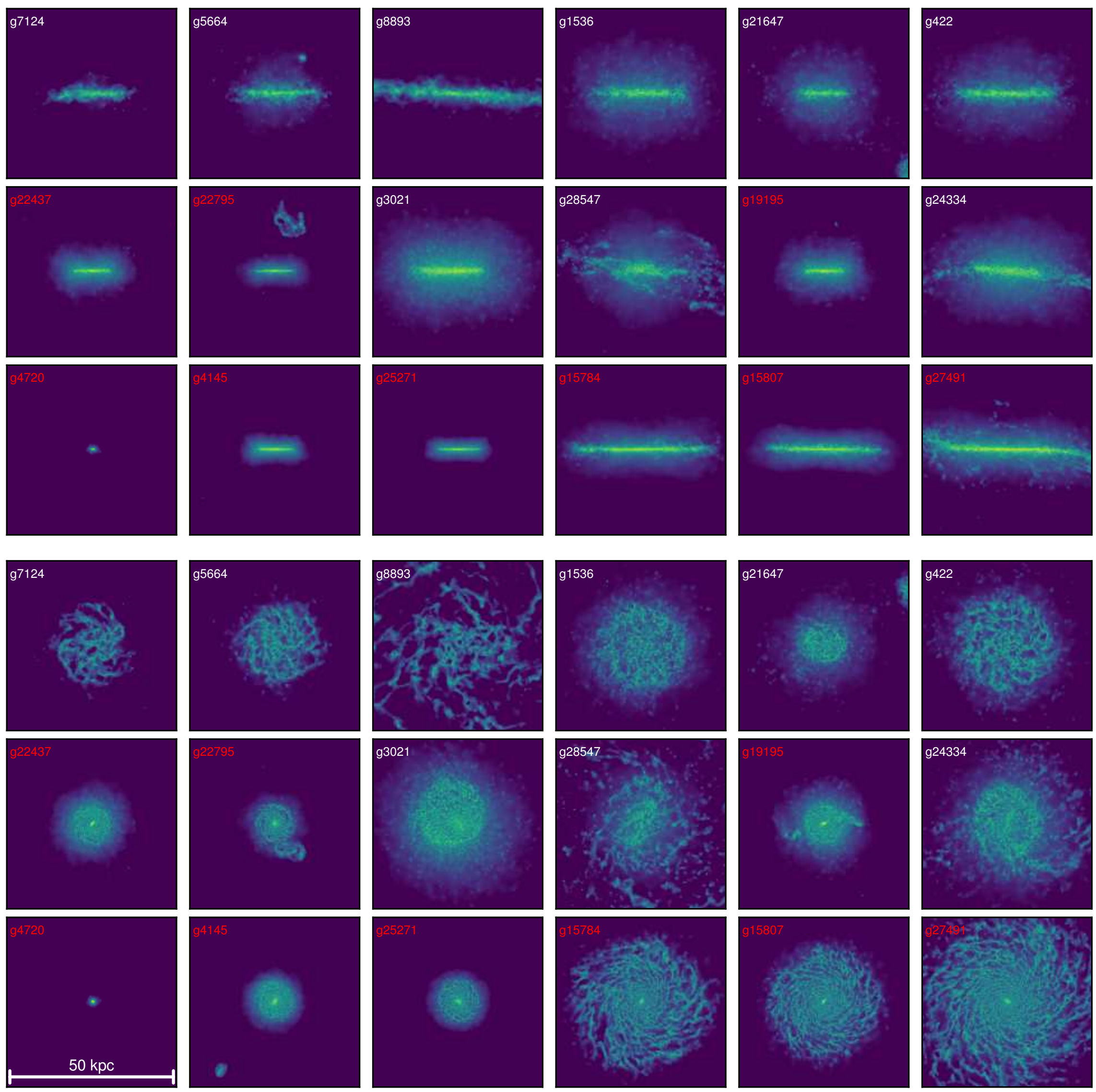

Figure 4.2: HI column density in each of the MUGS2 galaxies. As in Fig. 4.1, the top three rows show the galaxy edge on.

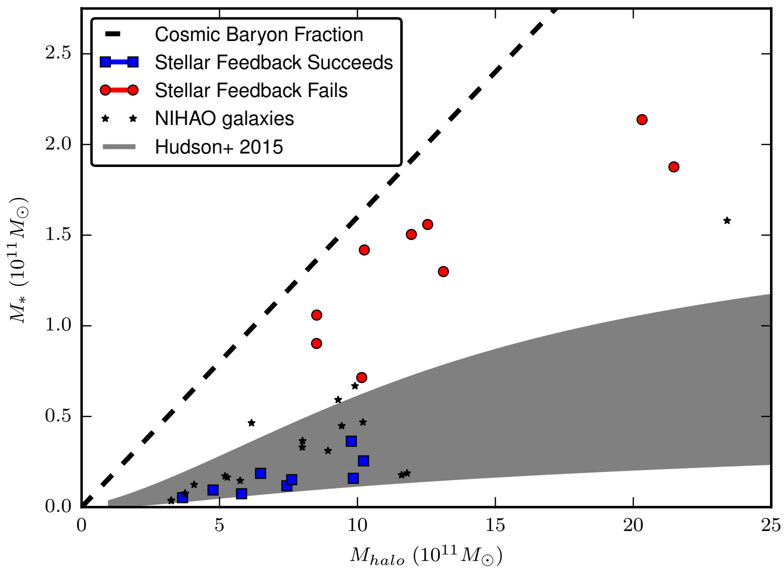

Figure 4.3: Stellar mass versus halo mass at $z = 0$. The observed stellar mass to halo mass relation is from Hudson et al. (2015)'s weak lensing study of galaxies to $z = 0.8$. Galaxies that fall within this range are shown as blue squares, while galaxies above the curve (those which form too many stars) are shown as red circles. For comparison, the black stars show galaxies from the NIHAO sample (Wang et al., 2015).

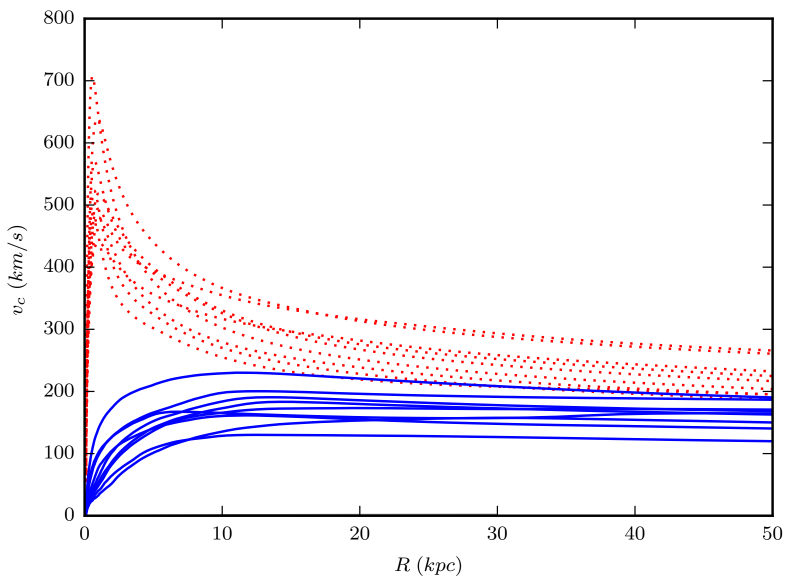

Figure 4.4: As is clear from the above rotation curves, galaxies which overproduce stars (shown in dotted red) also have large central concentrations, giving steeply peaked rotation curves inconsistent with those seen in local $L*$ galaxies. Galaxies with well-regulated star formation have flat rotation curves (shown in solid blue).

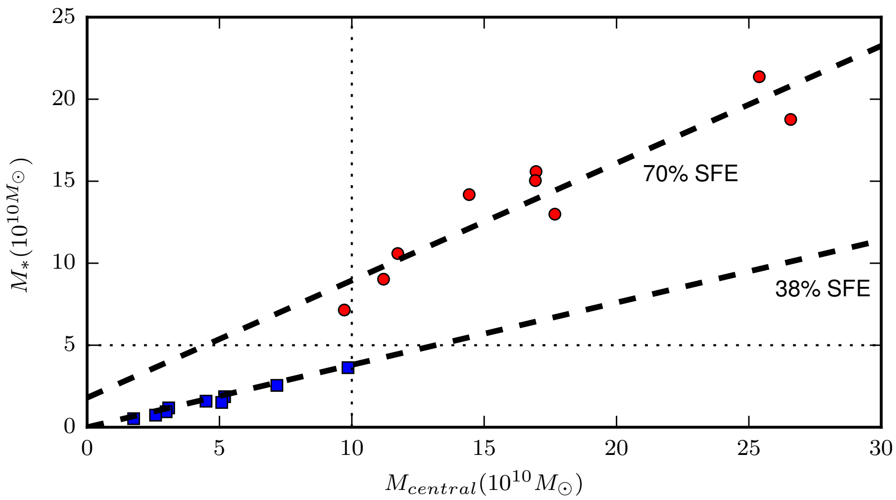

Figure 4.5: The stellar mass and the central baryonic mass show a tight correlation. For the well-regulated population, roughly 40% of the central baryons are stars, while for the unregulated population has converted $\sim 70\%$ of the central baryon mass into stars.

merger respectively. Major mergers are defined to match Stinson et al. (2010), as a merger with a halo containing at least 1/3 the stellar mass of the main progenitor. M_{vir}, M_*, and M_{gas} are the masses of the full halo, the stellar component, and the gas component respectively within the virial radius. $\mathrm{SFR}_{\mathrm{z=0}}$ is the redshift 0 SFR, averaged over the previous 100 Myr. The virial radius is defined as the radius around the halo such that the enclosed density is 200 times the critical density ($\rho = 200\rho_{\mathrm{crit}}$). While we used the same definitions for quantities reported in Stinson et al. (2010), every value reported here is derived from the new MUGS2 simulations. We also define a *central* region of the halo, which contains the disc and the majority of the stars within the halo. The baryon mass within this region is given as M_{central}. This central region is simply a sphere of radius $0.1R_{\mathrm{vir}}$.

Mock stellar observations and HI column images of these galaxies can be seen in Figs 4.1 and 4.2. The labels on each of these images are coloured red if they are in the 'unregulated' population discussed in the next section. The varied merger history of these galaxies is evident in these images: companions can be seen in three galaxies (g21647, g22795, g4145), tidal tails are evident in another (g19195), and strong bars exist in another two (g28547, g24334).

The HI column density shown in Fig. 4.2 shows, as was seen in Keller et al. (2015),

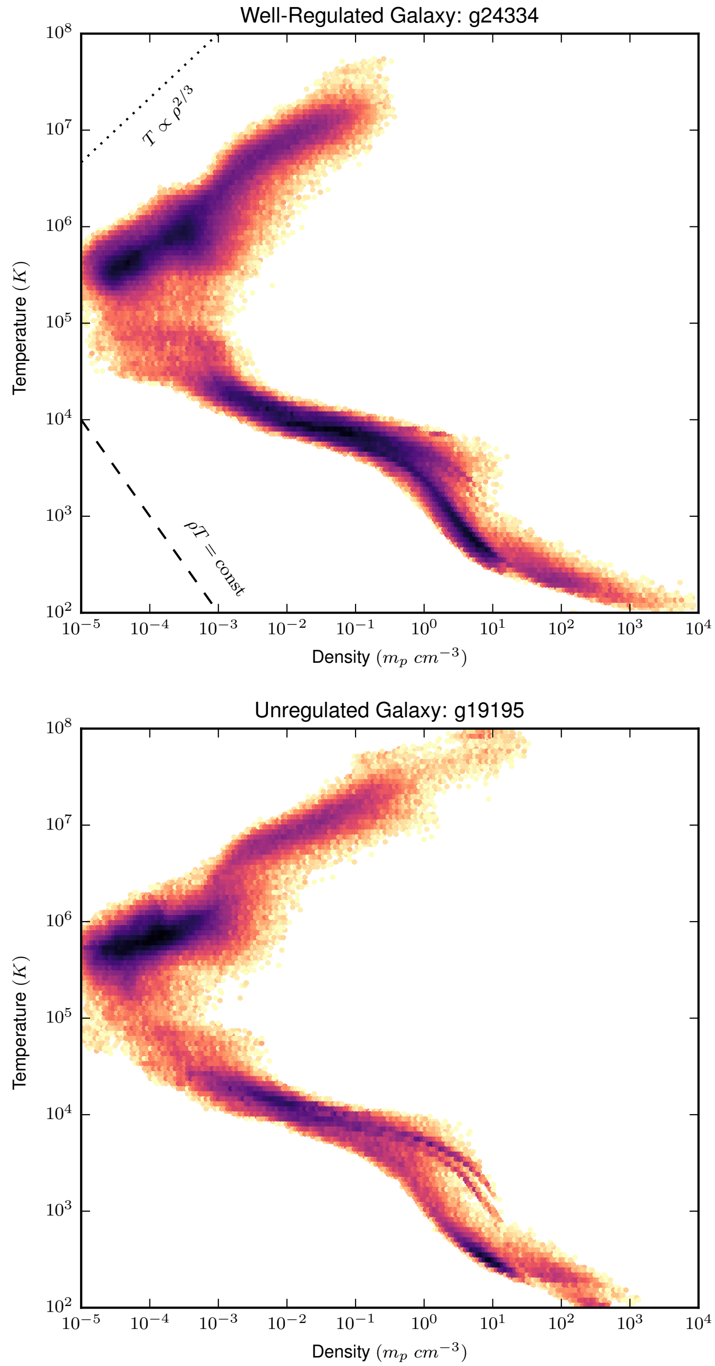

Figure 4.6: Gas phase diagrams for a well-regulated galaxy (g24334) and an unregulated galaxy (g19195). Colour shows the amount of mass at a given $\rho - T$ point. The top phase diagram shows the characteristic slope for adiabatic (dashed line) and isobaric (dotted line) processes. As can be seen, both galaxies are qualitatively the same. Both show the equilibrium cooling curve below 10^4 K, and both show the adiabatic evolution of superbubble-heated gas as it leaves the disc.

large quantities of extraplanar HI gas, driven up by outflows from the galaxy disc. HI gas above the galactic plane has been seen since Muller et al. (1963). Lockman (1984) found similar column densities to what is seen here to heights of 1.5 kpc. High-velocity clouds of relatively dense (~ 0.1 cm^{-3}) gas have also been seen both leaving and returning to the galaxy (Wakker & van Woerden, 1997). Diffuse HI gas has been observed out to ~ 300 kpc in absorption features of numerous nearby galaxies (Wakker & Savage, 2009; Prochaska et al., 2011). Werk et al. (2014) surveyed a number of galaxies in the COS-haloes survey, and found that typical $L*$ galaxies contain $\sim 5 \times 10^{10}$ M$_\odot$ of cool gas in their CGM. The face-on HI distribution for all but a handful of the unregulated (see the following section) follow the Broeils & Rhee (1997) HI mass-size relation, with HI column densities falling below 1 M$_\odot$ pc^{-2} at radii of $10 - 20$ kpc. This is well within the intrinsic scatter found in the recent observational study of Wang et al. (2016).

4.4.2 Stellar Mass Runaway

As can be seen in Fig. 4.3, roughly half of these galaxies fall within the expected $z = 0$ stellar mass to halo mass relation (SMHMR). The grey band shown in the figure is the 2σ confidence region in the observed SMHMR from Hudson et al. (2015), which used the CFHTLens weak lensing survey to produce a fully-observational SMHMR, without the uncertainties from using the dark matter-only simulations that are needed for abundance matching techniques (the Hudson et al. (2015) SMHMR is consistent with past abundance matching estimates such as Behroozi et al. (2013) and Moster et al. (2013)). For the rest of this paper, we will refer to the galaxies that fall within the 2σ confidence interval for the observed SMHMR (i.e. galaxies where stellar feedback prevents overproduction of stars) as *well-regulated*, and the galaxies where stellar feedback fails to produce the correct SMHMR as *unregulated*. No other criterion is used for determining which population a galaxy falls into. In addition to overproducing stars, these unregulated galaxies are qualitatively redder and more bulge dominated, as can be seen in the mock stellar images of Fig. 4.1. There appears to be no significant difference in the redshift of the last major merger between the two populations, strongly suggesting that the failure of stellar feedback to regulate the galaxies is not simply a matter of recent or violent merging. The rotation curves in Fig. 4.4 also show the distinct signature of massive bulges formed by catastrophic angular momentum loss in the unregulated population. van den Bosch (2001) showed that this can arise when

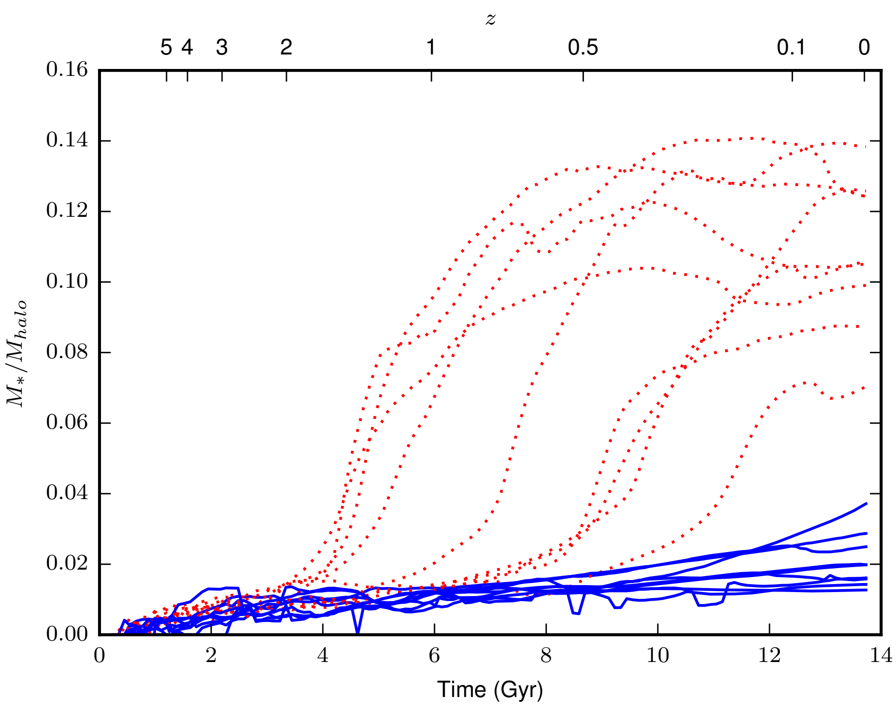

Figure 4.7: Stellar mass fraction versus time. As is clear, for the unregulated population the buildup of stellar mass above $\sim 3\%$ of the halo mass happens very rapidly, often on time-scales of ~ 1 Gyr. The runaway in the unregulated population stops simply when the disc has been sufficiently depleted of gas that little remains to form new stars.

gas simply traces the dark matter distribution, without redistribution or ejection by feedback. The strong peaks (as high as $700\,\mathrm{km\,s^{-1}}$ for g4720) come about from the central concentration of baryons in the galaxy bulge. Without exception, each of the well-regulated galaxies shows a flat rotation curve, with no evidence of a significant bulge component. This matches the qualitative morphology seen in Fig. 4.1.

Fig. 4.5 shows that for the well-regulated population, the stellar mass and central baryonic mass follow an extremely tight linear relation, with a mean star formation efficiency (simply defined here as the fraction of central baryons that are in stars) of $38 \pm 2\%$ over a Hubble time. For the galaxies that fail to self-regulate, they exhibit a total star formation efficiency of $70 \pm 10\%$, converting the majority of the baryons that collapse onto their disc into stars. Interestingly, the two populations can be divided cleanly along the $M_{\mathrm{central}} = 10^{11}$ $\mathrm{M_\odot}$ or the $M_* = 5 \times 10^{10}$ $\mathrm{M_\odot}$ axis. This is clear evidence that what explains the dichotomy here must involve the accretion (or the failure to remove!) baryons from the central region of the halo, where the disc resides and stars are formed. These relations also help to explain some of the correlations seen observationally, such as the critical mass of $3 \times 10^{10}\,\mathrm{M_\odot}$ that Kauffmann et al. (2003a) found dividing star forming and quenched galaxies in the SDSS at low redshift.

The gas phase diagram of galaxies in the two populations is remarkably similar, as can be seen in Fig. 4.6. For a representative pair from each population, of nearly equal halo mass, gas follows essentially the same evolutionary path, characteristic of a superbubble-regulated ISM, as was shown in Keller et al. (2015). Gas accretes from the halo, building up a warm ISM at $T \sim 10^4$ K. Where that gas reaches densities of ~ 1 cm^{-3}, it begins to cool quickly and form stars. Those stars begin to explode as SN, and a hot superbubble is formed, with $T > 10^7$ K. As the bubble grows, its temperature falls as it both expands adiabatically and evaporates the cold shell surrounding it. This hot, buoyant gas leaves the disc, rising through the CGM and cooling adiabatically as it goes. What is remarkable here is just how similar the phase diagrams of these two galaxies are. The slight differences are what we would expect from Table 4.1. g19195 has $\sim 50\%$ less gas than g24334, and more than 3 times the SFR at $z = 0$. Thus, there is less total material, especially in the warm and cold phases, and slightly more of the very hot ($T > 5 \times 10^7$ K) gas (the interiors of very young superbubbles) as a consequence of the higher SFR. What is important to take away from these phase diagrams is that a well-regulated and unregulated galaxy do not have any real difference in the phase behaviour of their gas. There is no runaway cooling, or failure of SN to generate hot gas: what causes the unregulated population to runaway is purely an effect of the outflow effectiveness, which is set by the depth of the potential well.

4.4.3 Time Evolution

The obvious question that arises from the presence of these two (well-regulated versus unregulated) populations at $z = 0$ is whether they are distinct through their entire evolution, and if not, why/how do they diverge? Previous work suggests that a characteristic (halo or stellar) mass exists above which AGN feedback is needed. There is much uncertainty, however, about where this mass exactly is, and how the transition from SN to AGN regulation actually works. We should thus expect galaxies to begin diverging once this characteristic mass is exceeded. As Fig. 4.7 shows, the stellar mass fraction for the two populations appear to follow similar evolutionary tracks for some time (until past $z = 0.5$ in the case of g19195, the galaxy which diverges the latest). However, once a galaxy begins to overproduce stars, it appears to do so in a runaway, doubling or even tripling its stellar mass fraction in less than a Gyr.

The similar early star formation history of the two populations is even more clear if we look at the SMHMR's time evolution in Fig. 4.8. Here we can see, that for galaxies with halo masses below a few 10^{11} $\mathrm{M_\odot}$, the stellar mass falls well within the expected SMHMR distribution, and the two populations are indistinguishable. The mass at which the populations begin to diverge ($M_* \sim 10^{10}$ $\mathrm{M_\odot}$ and $M_{\rm vir} \sim$ 3-5 $\times 10^{11}$ $\mathrm{M_\odot}$) are quite close to the expected transition range from Shankar et al. (2006) ($M_* \sim 1.2 \times 10^{10}$ $\mathrm{M_\odot}$ and $M_{\rm vir} \sim 3 \times 10^{11}$ $\mathrm{M_\odot}$).

The relatively smooth change in the $M_* - M_{\rm central}$ relation, shown in Fig. 4.9, shows that it is in fact the central baryon mass that is more tightly correlated with the stellar mass than the total halo mass (in galaxies regulated by SN feedback alone). In fact, it is likely that some of the more massive galaxies in the well-regulated sample are on their way to failing, but simply have not yet had enough time by $z = 0$ to diverge significantly from the observed SMHMR. Once more than $\sim 10^{11}$ $\mathrm{M_\odot}$ of baryons have accreted to the disc of a galaxy, SN alone appear to be unable to halt the growth of stellar mass. At this point, star formation efficiency of the central disc begins to increase, from $\sim$ 40 to $\sim$ 70 per cent, resulting in the differences seen in the two populations at $z = 0$. This accretion crisis, as it continues to smaller scales, also explains the rotation profiles of the unregulated population. The overcollapse that

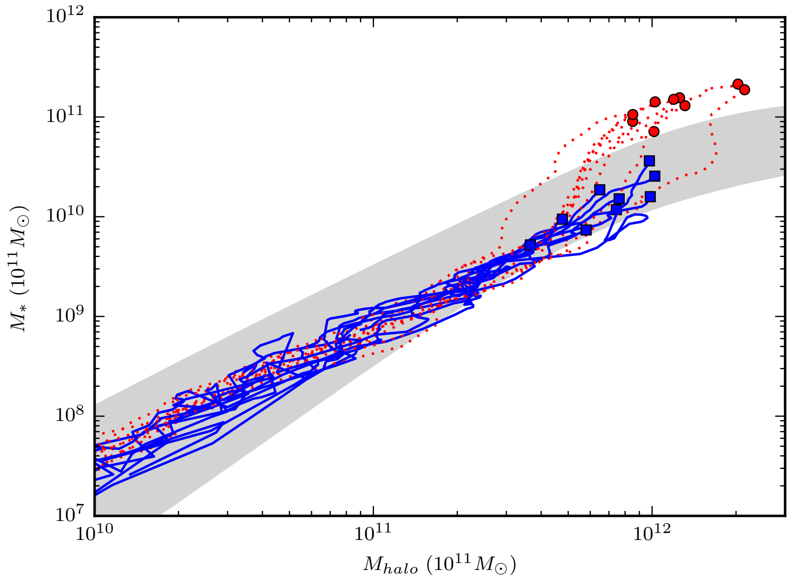

Figure 4.8: Stellar mass versus halo mass, as shown in Fig. 4.3, but with trails added to show time evolution. For halo masses below $\sim$ a few $\times\ 10^{11}$, the evolution of the regulated and unregulated populations are indistinguishable. The grey bar shows the $z = 0$ SMHMR, as in Fig. 4.3

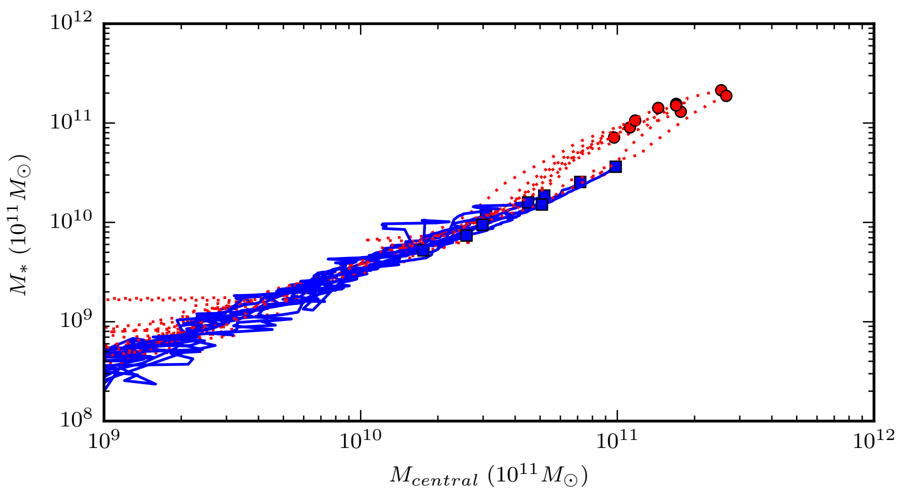

Figure 4.9: Stellar mass versus central baryon mass. The stellar mass here can be seen to vary much more smoothly over the evolution, without the slight 'jump' seen in Fig. 4.7. This indicates that both stellar mass and central baryonic masses are rapidly increasing together.

results in runaway star formation also builds a massive bulge, producing the peaked rotation curves seen in Fig. 4.4.

4.4.4 Galactic Outflows

A key metric for both observational and simulation studies of galactic outflows is the mass loading ($\eta = \dot{M}_{\rm out}/\dot{M}_*$) of these outflows. This scaling is usually written as a power-law scaling between mass loading η and the circular velocity of the halo or halo mass (Murray et al., 2005; Peeples & Shankar, 2011):

$$\eta \propto v_c^{-\alpha} = (GM_{\rm halo}/R_{\rm vir})^{-\alpha/2} \propto M_{\rm halo}^{-\alpha/3} \tag{4.3}$$

The normalization of this relation characterizes how generally effective stellar feedback is at driving galactic winds and outflows. The index α is a measure of how this effectiveness decreases for larger haloes, and ultimately results in a shutdown of large-scale outflows at high enough mass. This makes this scaling relation a key parameter to most semi-analytic galaxy formation models (e.g Cole et al. (2000)), and an attractive target for both theorists and observers alike. Two primary modes for driving galactic winds have been proposed. Energy-driven winds (such as those investigated by Mac Low & McCray (1988); Tegmark et al. (1993), etc.) assume the cooling times for outflowing material are shorter than the time required for a superbubble to break out of the galactic disc. These adiabatically expanding bubbles result in galactic winds with mass loadings that scale as $\eta \propto v_c^{-2}$. A recent study by Christensen et al. (2016) showed that SN driven winds follow this scaling, using mock observations of a sample of seven simulated galaxies. If the cooling times are instead much shorter than the break out time, then outflows become momentum driven (Murray et al., 2005), and the mass loadings instead are expected to scale as $\eta \propto v_c^{-1}$. Peeples & Shankar (2011) used a semi-empirical model to fit the mass–metallicity relationship in low redshift galaxies to predict that the mass loading index must be $\alpha = 3$ or steeper in order to produce a mass–metallicity relation as steep as is observed.

As in Keller et al. (2015), we define our outflow rate using the simple formula below, for gas particles that have $v_r > 0$, and are found between $0.1R_{\rm vir}$ and $R_{\rm vir}$:

$$\dot{M}_{\rm out} = \sum_{r_i \in {\rm shell}} \frac{M_i \boldsymbol{v_i} \cdot \hat{r}}{0.9R_{\rm vir}} \tag{4.4}$$

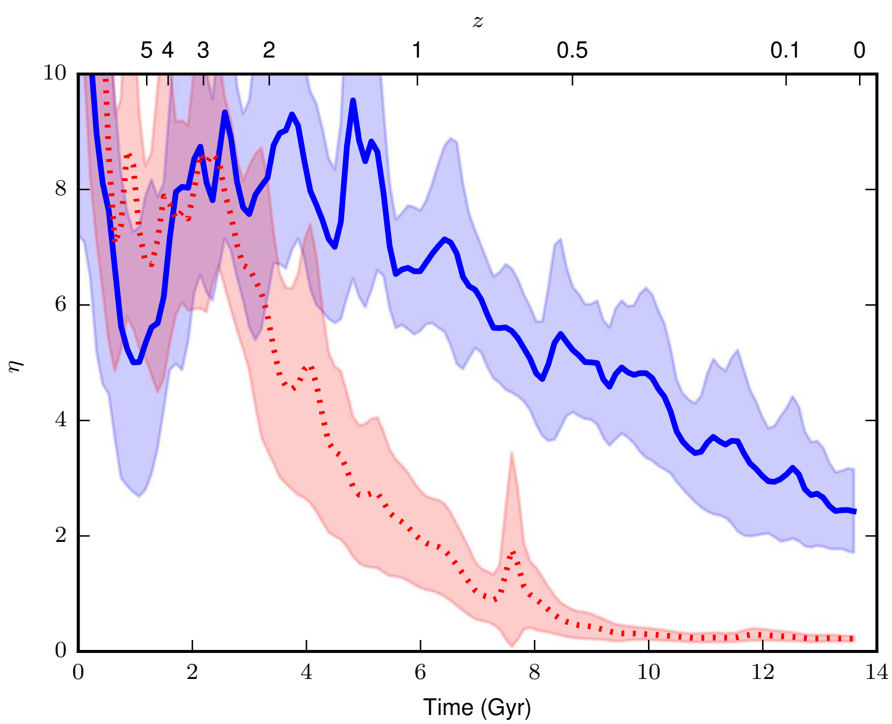

Figure 4.10: Outflow mass loading decreases as galaxies grow over time, as was previously shown by Keller et al. (2015). Here we see, when examining the mean mass loadings for the two populations (the well-regulated galaxies, where stellar feedback succeeds, and the unregulated galaxies, where it fails), that the unregulated galaxies have their mass loadings decrease sooner, and to lower values, than the well-regulated population. The error bars here are the 1σ scatter in each population.

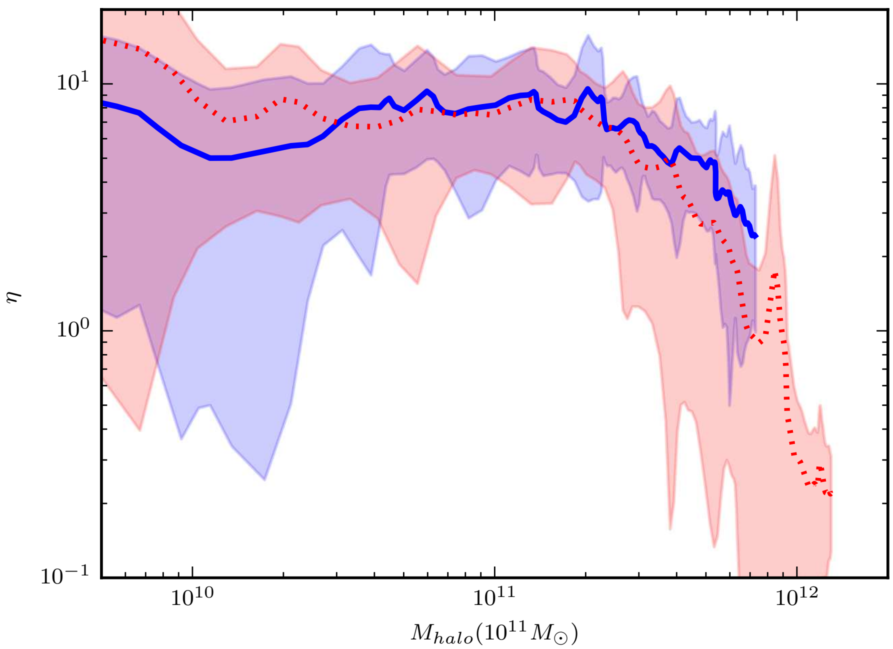

Figure 4.11: Unlike in the previous figure, if we look at mass loading as a function of halo mass, we instead see no significant difference between the two populations. Instead, both follow a similar trajectory, and the haloes which fail to self-regulate do so simply because they reach a higher mass earlier.

This choice reflects the nature of these outflows, where gas at high temperatures and low densities drifts outwards from the galaxy towards the virial radius. We chose a relatively thick shell to avoid the need for frequent simulation outputs. As such, our ability to resolve short-term bursts is somewhat reduced, but the overall outflow rates trace those from a test case with 8× more frequent outputs, and a shell 8× thinner. An excellent discussion of how to calculate outflow rates can be found in appendix A of Muratov et al. (2015).

If we take the mean mass loadings $\eta = \dot{M}_{\rm out}/{\rm SFR}$ of our two populations, we see in Fig. 4.10 that the mass loading for the unregulated population drops below $\eta = 1$ at $z \sim 0.5$, while the well-regulated population never drops below $\eta \sim 2$. This helps explain the correlation between the central concentration and stellar mass fraction (in particular, the dichotomy between the two populations, with low central baryon masses for well-regulated galaxies and high central masses for the unregulated galaxies). Failure to eject gas through outflows gives a higher central baryon mass, and those baryons inevitably become stars. However, we know that the unregulated population is on average heavier (both the full halo, as well as the central baryons). Does this earlier drop in outflow mass loading come about simply because the unregulated population gets heavier earlier?

Fig. 4.11 suggests exactly that. The mass loadings appear roughly constant, at $\eta \sim 10$ for most of the mass-range for both populations, but begin to fall at essentially the same mass, at what appears to be the same rate. An even tighter relation is seen in Fig. 4.12, when the relation between the central baryon mass, rather than just the halo mass, is examined. It appears that for the $\eta - M_{\rm halo}$ and $\eta - M_{\rm central}$ relation, a broken power-law fit, as defined below, describes both the regulated and unregulated population.

$$\eta = \begin{cases} \alpha M^{\beta} & \text{if } M < M_0 \\ (\alpha M_0^{\beta-\gamma}) M^{\gamma} & \text{if } M > M_0 \end{cases} \tag{4.5}$$

Using a simple non-linear least squares fit on the parameters α, β, γ, and M_0, we find that the most likely value for these parameters are $\alpha = 0.9 \pm 0.5$, $\beta = -0.01 \pm 0.06$, $\gamma = -1.3 \pm 0.1$, $M_0 = 10^{10.0 \pm 0.1}$ for the $\eta - M_{\rm central}$ relation, and $\alpha = 1 \pm 1$, $\beta = 0.0 \pm 0.1$, $\gamma = -1.8 \pm 0.2$, $M_0 = 10^{11.37 \pm 0.08}$ for the $\eta - M_{\rm halo}$ relation. A fit for both of the populations independently is consistent with these values derived for the full set of MUGS2 galaxies. Interestingly, *neither* of these slopes is consistent with simple

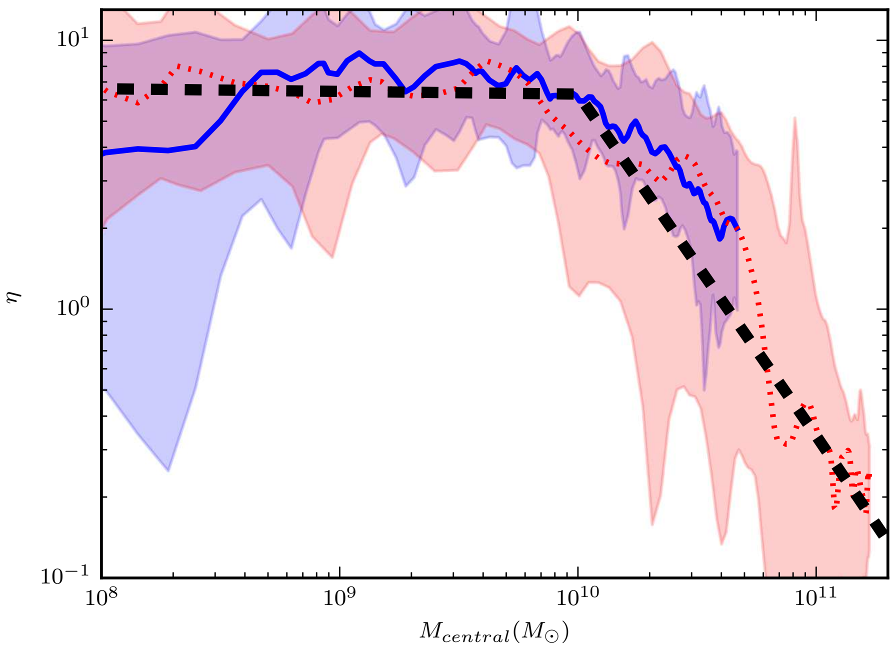

Figure 4.12: The mass loadings of the two populations are even more in agreement if we look at their relation to the central baryonic mass. As with the mass loading versus halo mass relation, we can fit a broken power law to this relation (shown here as the dashed line).

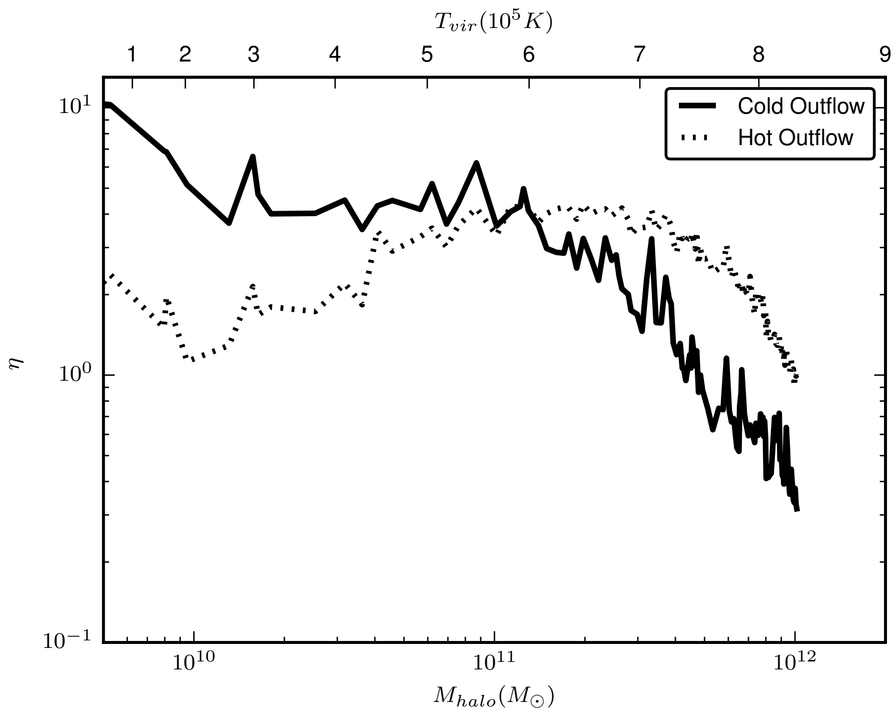

Figure 4.13: Mean outflow mass loading for the full sample, as a function of halo mass/virial temperature, and split into cold ($T < 10^5$ K) and hot ($T > 10^5$ K) components. For low-mass haloes, outflows are dominated by relatively cold gas (cooler superbubbles, and entrained material), while heavier haloes have primarily hot outflows. The transition occurs at a halo mass of $M_{\rm halo} \sim 10^{11}$ M$_\odot$, or a virial temperature of 6×10^5 K.

energy or momentum driven winds (although a single power-law fit does give a slope of $\sim 0.5 \pm 0.2$, consistent with an energy-driven scenario, albeit with a much weaker fit). These values are consistent, however, with the constraints derived for the mass–metallicity relation and gas content in nearby galaxies derived by Peeples & Shankar (2011) (namely, that α in the $\eta \propto v_c^{-\alpha}$ relation be steeper than 3).

The temperature of the outflows also shows an interesting trend as a function of halo mass. Fig. 4.13 shows that as halo mass increases, the mass loading of outflows with cold gas monotonically decreases, while the loading of hot gas is convex, peaking at $M_{\rm halo} = $ 2-5 $\times 10^{11}$ M$_\odot$, and then rapidly falling as halo mass increases. We define cold gas as having $T < 10^5$ K. We choose this as a cutoff point as it lies near the peak of the cooling curve, where we would expect, as Woods et al. (2014) showed, very little gas to be found. If we think in terms of virial temperature, this makes sense. At low $T_{\rm vir}$, gas around 10^5 K is buoyant, and will be driven out of the disc. The halo itself is smaller, with a shallower potential well, thus making it easier for the same amount of feedback energy to eject a larger amount of entrained gas. As the halo mass grows, eventually only the hottest gas is able to escape, and only if it is not weighed down by too much entrained material. Eventually, this effect means that the total mass loading begins to drop significantly.

We can see clearly in Fig. 4.14 that our winds essentially have a maximum effective velocity of $\sim 250 \mathrm{km\,s^{-1}}$. When the escape velocity at the edge of the galaxy (where we begin to measure outflows, at $0.1R_{\rm vir}$) exceeds this velocity, outflow mass loadings precipitously drop from ~ 10 to < 1. As Keller et al. (2014) showed, superbubble-heated gas tends to reach an equilibrium temperature of a a few million K, meaning that the outflow rates appear to fall significantly when outflowing gas, moving faster than the escape velocity from the disc is moving supersonically relative to the superbubble-heated gas. Radiative losses from cooling shocks may be important here for causing the drop in outflow efficiency that produces our two populations.

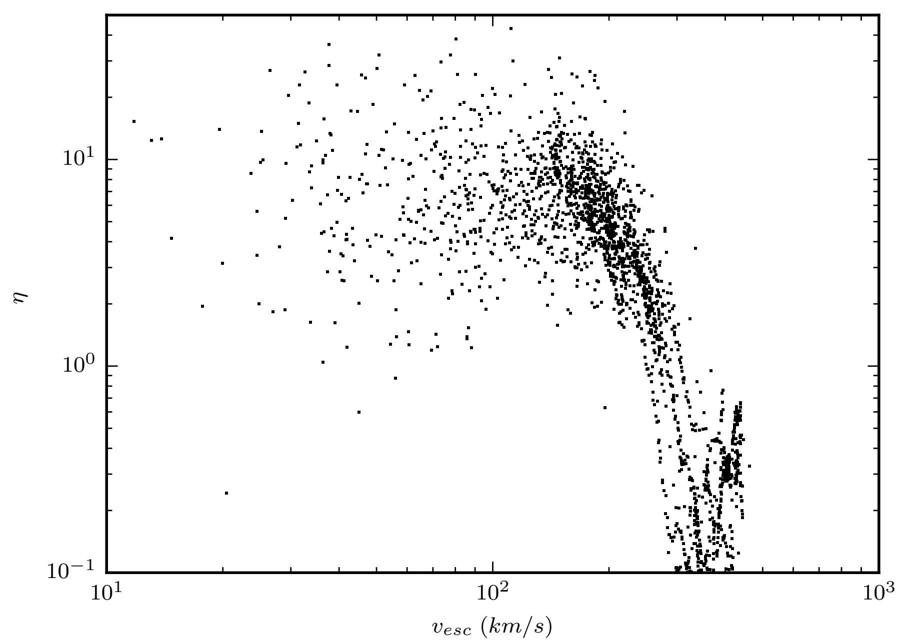

Figure 4.14: Mean outflow mass loading for the full sample, as a function of the escape velocity on the inner surface of our outflow shell ($0.1R_{\mathrm{vir}}$). Each galaxy is sampled 128 times over its evolution, giving us 2304 points across a range of redshifts. As can be seen, at $v_{\mathrm{esc}} \sim 250$ km/s, the mass loading begins to fall precipitously. This corresponds to the sound speed of solar-metallicity gas at a temperature of 3.5×10^6 K. This means that for gas at or above this temperature, sound waves alone are able to propel material significantly above the disc, and that kinetic energy losses due to shocks will be minimal. Gas cooler than that will need to be propelled supersonically, and will drive shocks in the CGM.

4.5 Discussion

In Keller et al. (2015), we showed that galactic outflows, driven by pure SN feedback modelled using the superbubble method of Keller et al. (2014) can produce a moderate mass $L*$ galaxy with a realistic star formation history and no significant bulge component. We have extended this work to a sample of 18 galaxies, covering a mass range of roughly an order of magnitude around that first galaxy. This allows us to probe the expected transition region, where SN feedback begins to fail as a self-regulation mechanism.

The transition between SN regulated galaxies at low mass and AGN regulated galaxies at high mass has been studied observationally in the past decade. Shankar et al. (2006) found that the relation between halo mass and stellar mass, r^*-band luminosity, or black hole mass all were characterized by double power laws, with breaks at $M_{\rm vir} \sim 3 \times 10^{11}$ M$_\odot$ or $M_* \sim 1 \times 10^{10}$ M$_\odot$. They interpreted these results as the transition between the scalings in SN and AGN regulated galaxies, and constructed a simple analytic model to show the plausibility of this idea. Croton et al. (2006) showed that the most massive galaxies could be produced in a semi-analytic model only when feedback luminosity no longer simply followed the SFR (as it would in stellar feedback), but instead scaled with an estimated black hole accretion luminosity (as one would expect from AGN feedback).

The most striking feature of this sample of simulated galaxies is the sharp divide between the two identified populations: the well-regulated galaxies and the unregulated galaxies. The well-regulated galaxies are bulgeless and blue, with a surfeit of extra-planar HI gas. The unregulated sample are red and bulge-dominated, with steep rotation curves, with maximum circular velocities as high as 700 km s^{-1}. The members of the well-regulated population have stellar mass fractions below 4%, while unregulated galaxies have stellar masses all above 6%, with some approaching the cosmic baryon fraction. Clearly, the unregulated galaxies do not match the observed properties of $L*$ galaxies in the nearby universe. SNe feedback in these galaxies has failed to prevent runaway bulge growth and star formation. It has failed because it has failed to efficiently drive winds, which Keller et al. (2015) showed to be essential for the formation of a realistic $L*$ galaxy. As we have assumed no additional losses in our feedback model it is unlikely that any physically motivated numerical change to how SN feedback is handled can remove this dichotomy.

Fig. 4.3 shows that while the unregulated galaxies tend to be more massive than the well-regulated ones, there is some overlap in the $M_{\rm halo}$ = 8-12 $\times 10^{12}$ $\rm M_\odot$ range, where there are both unregulated and well-regulated galaxies. Figs 4.7 and 4.8 show that the process of runaway star formation happens rapidly, and can begins over a wide range of halo masses. This is further evidence that something beyond simply the mass of the halo that hosts a galaxy is at play in determining whether or not SN fail to regulate the growth of that galaxy.

A much tighter correlation is seen when looking at the relation between the central baryon mass (essentially, the mass of baryons in the galaxy disc), and the stellar mass fraction. Figs 4.5 and 4.9 show that the stellar mass and central mass are tightly correlated, and that once the central mass reaches $\sim 10^{11}$ $\rm M_\odot$, SN feedback will begin to fail. This is not particularly surprising, as stars form in the disc, and if SFR occurred at a constant global efficiency, we would expect to see a correlation between the central baryon mass and the stellar mass. However, the two populations show quite different mean star formation efficiencies, with only $\sim 38\%$ of the well-regulated disc baryons existing in stars compared to $\sim 70\%$ in the unregulated population. This suggests strongly that the correlations seen between stellar surface density and quenching (Fang et al., 2013) can be set up by SN feedback before the AGN begins the quenching process. It should be noted that this correlation may simply be a consequence of size evolution in galaxies, combined with simple quenching dependent only on stellar mass (Peng et al., 2010; Lilly & Carollo, 2016). In this case too, though, that quenching relation appears to be initially established by where SN feedback begins to fail.

While propelling gas beyond the halo's virial radius will certainly ensure that material does not form stars or collapse through the disc to build a bulge, removing material from the halo is not necessary to preventing runaway star formation/bulge growth. Material cycling through the CGM, propelled to a few 100 kpc above the disc, can take hundreds of Myr to re-accrete back on to the disc. This means that the increasing escape velocity of the disc is more important to preventing outflows from regulating star formation than an increase in the total halo mass. A more massive halo, with a relatively light disc can still have high mass loadings in its SN-driven outflows, and still have those outflows remove star forming material from the disc for much a galaxy's life.

4.5.1 Outflow Scaling Relations and The End of Regulation

For gas ejected by stellar feedback, the path out of a galaxy disc is fraught. To actually escape the disc, buoyant gas must push through the gas above it. High resolution simulations of disc slices have shown that this means SN occurring higher above or below the disc drive hotter, faster outflows (von Glasow et al., 2013; Sarkar et al., 2015). These results have tended to show that when feedback is deposited randomly, as opposed to at density peaks, stronger outflows can be driven. This is problematic for the simple fact that star formation should be occurring most vigorously in the densest ISM gas, and this should therefore be the site of most feedback deposition. Drift of stars from their natal environment can give some offset between moderately dense gas and where supernovae eventually detonate, but it is unlikely that this is a significant effect for the majority of stars. Governato et al. (2010); von Glasow et al. (2013); Christensen et al. (2016) showed that when SN feedback is clustered, it produces stronger outflows compared to the same number of SN spread distributed more smoothly throughout the disc. Unfortunately, even these high-resolution, well controlled studies have found significant variation in how wind mass loadings scale with halo mass. The relationship between circular velocity and mass loading has been found to vary both as a function of how feedback energy is injected (von Glasow et al., 2013) and what scaling relationship was used to determine halo mass from of the slice (Creasey et al. (2013) found that using different scaling relations between the halo mass and surface density could give an index α that varies from 2.5 to 4.8). These fully cosmological simulations have the advantage of removing this second source of uncertainty.

The failure of SN to regulate the more massive, disc-heavy galaxies is ultimately a consequence of the relationship between the efficiency of SN powered outflows and the mass of the halo (or more precisely, the disc). Figs 4.11 and 4.12 show that the outflow mass loading is characterized by a broken power law, with roughly constant mass loadings at low mass, and mass loadings that follow a power law with negative slope once a critical mass is exceeded. This model for outflow mass loadings is similar to one explored by Font et al. (2011). They found that, in a semi-analytic study of the Milky Way satellites, the best fit for the observed luminosity function was a so-called 'saturated feedback' model, where mass loadings were flat at low masses, and decreased as a constant power law in haloes with $v_c > 65\,\mathrm{km\,s^{-1}}$ (somewhat lower than the critical value we have found). Further evidence against a single power law in the $\eta - M$ relation came from recent work by Hou et al. (2016). By combining the analysis of Font et al. (2011) along with more recent MW satellite data, the mass–metallicity relation in local galaxies, and estimates of the redshift of reionization, they found that only a broken power law for the $\eta - M$ relation can fit all of the observed data. Not only that, their 'saturated' model resembles quite closely the fit we have found here, with a flat slope at low masses, and $\eta \propto M_{\rm halo}^{-1.1}$ for high masses. Muratov et al. (2015) found a nearly flat $\eta - M_{\rm halo}$ relation using the FIRE feedback model, with $\eta \propto M_{\rm halo}^{-0.35}$.

This relation seems to arise as a result of different $\eta - M$ relations for cold and hot gas. The combination of a steadily decreasing mass loading for cold gas, combined with hot gas mass loadings that peak at $M_{\rm halo} \sim 5 \times 10^{11}$ $\mathrm{M}_\odot$ ultimately result in the broken power-law we see for all outflowing material. In an upcoming study, we will be examining how this relation ultimately arises through detailed examination of ultra high resolution simulations of outflow regions. A detailed study of the hydrodynamics of wind venting should determine the processes by which cold ISM is entrained within the hot outflowing gas, and hopefully explain the origin of the $\eta - M$ relations we have found here.

The results here also show that even in the unregulated population, superbubbles are still able to break out of the galaxy disc (as is shown by the adiabatic evolution of feedback-heated gas seen in Fig. 4.6). In order for a superbubble to cool adiabatically by a factor of ~ 100, it must be able to expand by that same factor, and only once it has left the galaxy disc is there enough room for it to do this. The failure of SN feedback in the massive, unregulated population is an issue of a drop in efficiency, rather than a complete shutoff, of galactic outflows. The reason the unregulated population exists is that the galaxies in this population spent roughly half of their lifetime above the critical mass in the $\eta - M$ relation, where SN cannot efficiently drive outflows. This has resulted in these galaxies becoming too centrally concentrated, and vastly overproducing stars. Figs 4.13 and 4.14 show that at higher masses (either for the halo itself, or simply for the interior regions), only the hottest material is able to escape from the disc.

The $\sim 250\,\mathrm{km\,s^{-1}}$ break in mass loading seen in Fig. 4.14 corresponds to the sound speed of relatively hot gas (3.5×10^6 K for solar metallicity). Even with no radiative losses whatsoever, if 10^{51} erg is deposited into 1000 $\mathrm{M}_\odot$ of gas (the specific energy that

$\eta = 10$ would yield), this gas would have a temperature of 2.5×10^6 K, and a sound speed of only $\sim 210\,\mathrm{km\,s^{-1}}$. This temperature is set by the self-regulating process of thermal evaporation, and is comparable to the internal temperatures seen in other studies of isolated superbubbles that have included the effects of evaporation (Mac Low & McCray, 1988; Silich et al., 1996; Keller et al., 2014). Thus, it is somewhat unsurprising that the mass-loadings seen here only stay high for escape velocities below $200\,\mathrm{km\,s^{-1}}$. With mass-loadings falling to unity at escape velocities of almost exactly $300\,\mathrm{km\,s^{-1}}$, we can infer that the total losses (radiatively and otherwise) between the initial SN explosions and the subsequent outflows are $\sim 80\%$. The roughly constant outflow rates seen at lower masses/escape velocities imply that a process other than radiative losses is limiting the outflow mass-loadings. The hydrodynamic coupling between hot, outflowing gas and the surrounding medium (the key process that is involved in setting these mass loadings) will be the subject of a subsequent study. Naturally, if additional feedback energy (i.e. non-SN feedback) is available to heat a significant amount gas above $\sim 3 \times 10^6$ K, or propel it to speeds above $\sim 250\,\mathrm{km\,s^{-1}}$, this limiting mass will be higher. If radiative or other losses are higher than what was calculated in these simulations, the limiting mass will of course be lower.

It should be noted that our selection criteria for haloes (specifically, the exclusion of haloes with massive neighbours within 2.7 Mpc), combined with the use of the zoom-in technique, specifically excludes the environmental effects. It is known that environmental effects can cause correlations in galaxies separated by > 5 Mpc (Weinmann et al., 2006). The galaxies here are therefore not probing the effects of quenching by nearby radio-loud AGN (Kauffmann, 2015), or the hot haloes of larger overdensities (Kauffmann et al., 2013). These limits therefore may not hold in denser environments, such as the outskirts of a cluster, where external processes may help regulate star formation.

4.5.2 Runaway bulge growth points to AGN feedback

The existence of an unregulated population of galaxies raises the question of what physical mechanism is missing in these simulations. What is important to consider is that this missing physics must be more effective in the high-mass, bulge dominated unregulated population without causing the low mass/well-regulated population to underproduce stars, or disrupt their discs.

While CRs rays may be important in certain ISM environments, and may drive the fastest components of galactic winds, there is no known mechanism involved in CR feedback that suggests they become more effective at higher mass. In particular, there is nothing to suggest that the critical mass we see at $M_{\rm halo} \sim 10^{12}\,{\rm M}_{\odot}$ is in any way related to the efficiency or effectiveness of CR feedback. For the unregulated population, previous results suggest that CRs alone will not be able to produce outflows any more effectively than we have seen SN alone drive, as the mass-loadings they can produce are typically $\ll 10$. Past simulations have also shown that for the mass range where SN feedback begins to fail to regulate star formation, radiation pressure either fails to prevent overproduction of stars (Aumer et al., 2013), or completely disrupts the thin disc (Roškar et al., 2014), producing 'puffy', spherical galaxies with large stellar scale heights, depending on the details of the subgrid model and how that translates into a coupling between the photon fluid and the ISM.

The fact that SN begin to fail at relatively high masses hints that the mechanism that begins to take over in regulating the growth of the galaxy is AGN. It has long been suspected that the high-mass end of galaxy evolution was dominated by AGN feedback from the growth of their SMBHs, and this has been explored heavily in semi-analytic models (Bower et al., 2006; Croton et al., 2006; Shankar et al., 2006). AGN feedback has also become an essential component of large-volume simulations, such as EAGLE (Schaye et al., 2015) and Illustris (Sijacki et al., 2015). Higher resolution hydrodynamic simulations such as Di Matteo et al. (2005); Ciotti et al. (2010); Hopkins et al. (2016) have found that AGN can have dramatic effect on the galactic ISM and star formation. A survey of SDSS galaxies with found that the detectable AGN fraction was essentially zero below $M_* \sim 10^{10}$ ${\rm M}_{\odot}$, rising to $\sim 50\%$ by $M_* \sim 5 \times 10^{10}$ ${\rm M}_{\odot}$, with essentially all galaxies with $M_* > 5 \times 10^{11}$ ${\rm M}_{\odot}$ hosting an AGN (Kauffmann et al., 2003b). This transition mass lies exactly where our two populations begin to diverge. No galaxy in our sample with $M_* < 4 \times 10^{10}$ ${\rm M}_{\odot}$ is unregulated, and all but two of the unregulated galaxies have stellar masses above 10^{11} ${\rm M}_{\odot}$ (the same effect, at the same stellar mass was seen in the group simulations of (Liang et al., 2016), which used a prescription for momentum-driven, SN powered winds). This is particularly interesting when considering the population of 'powerful' AGN in the SDSS peaks at $M_* \sim 10^{11}$ ${\rm M}_{\odot}$. If these powerful AGN effectively quench star formation within their host galaxies, clamping the stellar mass at or below $10^{11}\,{\rm M}_{\odot}$, this mechanism would put essentially all of our unregulated population back within the Hudson et al. (2015) SMHMR. If these AGN also ejected a significant fraction of the gas within the inner < 1 kpc of the unregulated population, it would also solve the problem of their unrealistically large bulges and peaked rotation curves. These results suggest that AGN not only *can* regulate star formation and bulge growth in massive discs, they *must* do so to produce realistic galaxies in haloes more massive than 10^{12} $M_\odot$.

The correlation between black hole mass and bulge mass (see Kormendy & Ho 2013 for a review of this evidence) is strong evidence that the central regions co-evolve with with the galaxy (pseudo-)bulge (to first order, this of course must be the case: they are formed from the same material, in roughly the same place). The fact that our unregulated population has grown a much too massive bulge makes AGN feedback an attractive potential resolution. In order to build these massive bulges, angular momentum losses in the gas disc must have been significant, funnelling material down towards the centre of the disc. This naturally would be a necessary component to fuelling the growth of an SMBH, and powering an AGN. The well-regulated population likely would under produce stars if AGN feedback was a strong effect in those galaxies. Conveniently, the lack of any sort of significant bulge component means that the SMBH within those galaxies would likely be starved of fuel, preventing any significant, sustained AGN feedback. Further evidence for the negligible effect of AGN feedback for these smaller galaxies comes again from the SDSS, where it can be seen that galaxies with $M_* < 5 \times 10^{10}$ $M_\odot$ contain a powerful AGN in less than 5% of the cases.

4.6 Conclusion

By correctly modelling SN-driven superbubble feedback, we allow clustered star formation to efficiently drive outflows. This allows SN feedback to produce lower mass galaxies with flat rotation curves, realistic SMHMRs, and small bulges. SN feedback breaks down as a regulator of stellar mass and bulge growth in galaxies with halo masses $> 10^{12}$ $M_\odot$ (or stellar masses $> 4 \times 10^{10}$ $M_\odot$). This breakdown produces a distinct pair of populations. Galaxies below these critical masses have stellar masses within the observed SMHMR, flat rotation curves, and more mass loaded winds over their evolutionary history. When simulated with SN feedback alone, galaxies above this mass have stellar fractions approaching the cosmic baryon fraction, redder stellar populations, steeply peaked rotation curves with maximum circular velocities as high as $700\,\mathrm{km\,s^{-1}}$, and relatively inefficient outflows. As massive galaxies grow, they move from the well-regulated to unregulated population quickly, typically producing the bulk of their stars in a burst lasting ≤ 1 Gyr, after which star formation slows simply due to a dearth of gas to form stars out of.

The cause for this transition is the relation between the mass loading of superbubble outflows η and the halo or disc mass. A critical value exists for both of these masses, where mass loadings begin to drop steeply as mass increases, reducing the ability of SN to regulate the SFR and baryon content of the galaxy. Once the escape velocity from the inner $0.1R_{\rm vir}$ exceeds $\sim 250\,{\rm km\,s^{-1}}$, mass loadings fall rapidly to > 1. A simple broken power-law fit describes the relation between the outflow mass loading and both the halo mass and disc mass. For disc mass below $10^{10}\,{\rm M_\odot}$ and halo mass below $2\times10^{11}\,{\rm M_\odot}$, outflow mass loadings are approximately constant, with $\eta \sim 8$. It is ultimately the mixing driven by thermal evaporation that sets this mass loading, and the transition mass we have observed here. These simulations are the first cosmological sample to explicitly include this physics.

SN feedback begins to fail at exactly the mass range that strong AGN are observationally detected. This coincides with the runaway growth of massive stellar bulges in the unregulated population. The associated black hole feeding and nuclear activity should not only regulate bulge growth but also the total baryonic distribution and star formation for galaxies at the high mass end. Up to this mass, SN-driven superbubbles alone can regulate the baryonic content and star formation in galaxies.

If high mass loadings ($\eta \sim 10$) are a critical component of galaxy evolution in nature, then it is energetically impossible for SNe alone to produce realistic galaxies above the halo masses we have found. Whether that mass loading is achieved physically, as we have done with thermal evaporation, or numerically, the fixed injection energy of SN will ultimately yield a maximum halo mass, above which SN will be unable to drive winds with high mass loadings.

Acknowledgements

The analysis was performed using the pynbody package (`http://pynbody.github.io/`, Pontzen et al. 2013). We thank Alyson Brooks, Fabio Governato, Tom Quinn, and John Kormendy for useful conversations regarding this paper. We also thank the referee of this paper for many helpful suggestions. The simulations were performed on the clusters hosted on SCINET, part of ComputeCanada. We greatly appreciate the contributions of these computing allocations. We also thank NSERC for funding supporting this research.

Bibliography

Agertz O., Kravtsov A. V., 2015, ApJ, 804, 18

Aumer M., White S. D. M., Naab T., Scannapieco C., 2013, MNRAS, 434, 3142

Bailin J., Stinson G., Couchman H., Harris W. E., Wadsley J., Shen S., 2010, ApJ, 715, 194

Behroozi P. S., Wechsler R. H., Conroy C., 2013, ApJ, 770, 57

Booth C. M., Agertz O., Kravtsov A. V., Gnedin N. Y., 2013, ApJ, 777, L16

Bower R. G., Benson A. J., Malbon R., Helly J. C., Frenk C. S., Baugh C. M., Cole S., Lacey C. G., 2006, MNRAS, 370, 645

Breitschwerdt D., McKenzie J. F., Voelk H. J., 1991, A&A, 245, 79

Broeils A. H., Rhee M.-H., 1997, A&A, 324, 877

Bullock J. S., Dekel A., Kolatt T. S., Kravtsov A. V., Klypin A. A., Porciani C., Primack J. R., 2001, ApJ, 555, 240

Chabrier G., 2003, PASP, 115, 763

Christensen C. R., Davé R., Governato F., Pontzen A., Brooks A., Munshi F., Quinn T., Wadsley J., 2016, ApJ, 824, 57

Chu Y.-H., Kennicutt Jr. R. C., 1994, ApJ, 425, 720

Ciotti L., Ostriker J. P., Proga D., 2010, ApJ, 717, 708

Cole S., Lacey C. G., Baugh C. M., Frenk C. S., 2000, MNRAS, 319, 168

Crain R. A., et al., 2015, MNRAS, 450, 1937

Creasey P., Theuns T., Bower R. G., 2013, MNRAS, 429, 1922

Croton D. J., et al., 2006, MNRAS, 365, 11

Dale J. E., Bonnell I. A., Clarke C. J., Bate M. R., 2005, MNRAS, 358, 291

Dale J. E., Ercolano B., Bonnell I. A., 2012, MNRAS, 424, 377

Davé R., Hellsten U., Hernquist L., Katz N., Weinberg D. H., 1998, ApJ, 509, 661

Dekel A., Silk J., 1986, ApJ, 303, 39

Di Matteo T., Springel V., Hernquist L., 2005, Nature, 433, 604

Dubois Y., et al., 2014, MNRAS, 444, 1453

Efstathiou G., 1992, MNRAS, 256, 43P

Erb D. K., 2008, ApJ, 674, 151

Everett J. E., Zweibel E. G., Benjamin R. A., McCammon D., Rocks L., Gallagher III J. S., 2008, ApJ, 674, 258

Fang J. J., Faber S. M., Koo D. C., Dekel A., 2013, ApJ, 776, 63

Finlator K., Davé R., 2008, MNRAS, 385, 2181

Font A. S., et al., 2011, MNRAS, 417, 1260

Gendelev L., Krumholz M. R., 2012, ApJ, 745, 158

Girichidis P., et al., 2016, ApJ, 816, L19

Governato F., et al., 2010, Nature, 463, 203

Gupta A., Mathur S., Krongold Y., Nicastro F., Galeazzi M., 2012, ApJ, 756, L8

Hahn O., Martizzi D., Wu H.-Y., Evrard A. E., Teyssier R., Wechsler R. H., 2015, preprint, (arXiv:1509.04289)

Heckman T. M., Armus L., Miley G. K., 1987, AJ, 93, 276

Hopkins P. F., 2013, MNRAS, 428, 2840

Hopkins P. F., Quataert E., Murray N., 2011, MNRAS, 417, 950

Hopkins P. F., Quataert E., Murray N., 2012a, MNRAS, 421, 3488

Hopkins P. F., Quataert E., Murray N., 2012b, MNRAS, 421, 3522

Hopkins P. F., Kereš D., Oñorbe J., Faucher-Giguère C.-A., Quataert E., Murray N., Bullock J. S., 2014, MNRAS, 445, 581

Hopkins P. F., Torrey P., Faucher-Giguère C.-A., Quataert E., Murray N., 2016, MNRAS, 458, 816

Hou J., Frenk C. S., Lacey C. G., Bose S., 2016, MNRAS,

Hudson M. J., et al., 2015, MNRAS, 447, 298

Ipavich F. M., 1975, ApJ, 196, 107

Jubelgas M., Springel V., Enßlin T., Pfrommer C., 2008, A&A, 481, 33

Kauffmann G., 2015, MNRAS, 454, 1840

Kauffmann G., et al., 2003a, MNRAS, 341, 54

Kauffmann G., et al., 2003b, MNRAS, 346, 1055

Kauffmann G., Li C., Zhang W., Weinmann S., 2013, MNRAS, 430, 1447

Keller B. W., Wadsley J., Benincasa S. M., Couchman H. M. P., 2014, MNRAS, 442, 3013

Keller B. W., Wadsley J., Couchman H. M. P., 2015, MNRAS, 453, 3499

Kormendy J., Ho L. C., 2013, ARAA, 51, 511

Kroupa P., Weidner C., 2003, ApJ, 598, 1076

Krumholz M. R., Matzner C. D., 2009, ApJ, 703, 1352

Krumholz M. R., Thompson T. A., 2013, MNRAS, 434, 2329

Kunth D., Mas-Hesse J. M., Terlevich E., Terlevich R., Lequeux J., Fall S. M., 1998, A&A, 334, 11

Larson R. B., 1974, MNRAS, 169, 229

Leitherer C., et al., 1999, ApJS, 123, 3

Leroy A. K., et al., 2015, ApJ, 814, 83

Liang L., Durier F., Babul A., Davé R., Oppenheimer B. D., Katz N., Fardal M., Quinn T., 2016, MNRAS, 456, 4266

Lilly S. J., Carollo C. M., 2016, preprint, (arXiv:1604.06459)

Lockman F. J., 1984, ApJ, 283, 90

Lynds C. R., Sandage A. R., 1963, ApJ, 137, 1005

Mac Low M.-M., McCray R., 1988, ApJ, 324, 776

Magorrian J., et al., 1998, AJ, 115, 2285

Marasco A., Fraternali F., Binney J. J., 2012, MNRAS, 419, 1107

Marigo P., Girardi L., Bressan A., Groenewegen M. A. T., Silva L., Granato G. L., 2008, A&A, 482, 883

Martin C. L., Shapley A. E., Coil A. L., Kornei K. A., Bundy K., Weiner B. J., Noeske K. G., Schiminovich D., 2012, ApJ, 760, 127

Mathews W. G., Baker J. C., 1971, ApJ, 170, 241

Meyer L., et al., 2012, Science, 338, 84

Morganti R., Oosterloo T. A., Emonts B. H. C., van der Hulst J. M., Tadhunter C. N., 2003, ApJ, 593, L69

Moster B. P., Naab T., White S. D. M., 2013, MNRAS, 428, 3121

Muller C. A., Oort J. H., Raimond E., 1963, Acad. Sci. Paris C. R., 257, 1661

Muratov A. L., Kereš D., Faucher-Giguère C.-A., Hopkins P. F., Quataert E., Murray N., 2015, MNRAS, 454, 2691

Murray N., Quataert E., Thompson T. A., 2005, ApJ, 618, 569

Murray N., Ménard B., Thompson T. A., 2011, ApJ, 735, 66

Nickerson S., Stinson G., Couchman H. M. P., Bailin J., Wadsley J., 2011, MNRAS, 415, 257

Nickerson S., Stinson G., Couchman H. M. P., Bailin J., Wadsley J., 2013, MNRAS, 429, 452

Peeples M. S., Shankar F., 2011, MNRAS, 417, 2962

Peng Y.-j., et al., 2010, ApJ, 721, 193

Pontzen A., Roškar R., Stinson G., Woods R., 2013, pynbody: N-Body/SPH analysis for python, Astrophysics Source Code Library (ascl:1305.002)

Prochaska J. X., Weiner B., Chen H.-W., Mulchaey J., Cooksey K., 2011, ApJ, 740, 91

Ritchie B. W., Thomas P. A., 2001, MNRAS, 323, 743

Rogers H., Pittard J. M., 2013, MNRAS, 431, 1337

Roškar R., Teyssier R., Agertz O., Wetzstein M., Moore B., 2014, MNRAS, 444, 2837

Salem M., Bryan G. L., 2014, MNRAS, 437, 3312

Sarkar K. C., Nath B. B., Sharma P., Shchekinov Y., 2015, MNRAS, 448, 328

Schaye J., et al., 2015, MNRAS, 446, 521

Shankar F., Lapi A., Salucci P., De Zotti G., Danese L., 2006, ApJ, 643, 14

Shen S., Wadsley J., Stinson G., 2010, MNRAS, 407, 1581

Sijacki D., Vogelsberger M., Genel S., Springel V., Torrey P., Snyder G. F., Nelson D., Hernquist L., 2015, MNRAS, 452, 575

Silich S. A., Franco J., Palous J., Tenorio-Tagle G., 1996, ApJ, 468, 722

Socrates A., Davis S. W., Ramirez-Ruiz E., 2008, ApJ, 687, 202

Songaila A., Cowie L. L., 1996, AJ, 112, 335

Springel V., Hernquist L., 2003, MNRAS, 339, 289

Stark A. A., Carlson E. R., 1984, ApJ, 279, 122

Stinson G., Seth A., Katz N., Wadsley J., Governato F., Quinn T., 2006, MNRAS, 373, 1074

Stinson G. S., Bailin J., Couchman H., Wadsley J., Shen S., Nickerson S., Brook C., Quinn T., 2010, MNRAS, 408, 812

Stinson G. S., Brook C., Macciò A. V., Wadsley J., Quinn T. R., Couchman H. M. P., 2013, MNRAS, 428, 129

Tegmark M., Silk J., Evrard A., 1993, ApJ, 417, 54

Veilleux S., Cecil G., Bland-Hawthorn J., 2005, ARAA, 43, 769

Vogelsberger M., Genel S., Sijacki D., Torrey P., Springel V., Hernquist L., 2013, MNRAS, 436, 3031

Vogelsberger M., Genel S., Sijacki D., Torrey P., Springel V., Hernquist L., 2014a, MNRAS, 438, 3607

Vogelsberger M., et al., 2014b, MNRAS, 444, 1518

Wakker B. P., Savage B. D., 2009, ApJS, 182, 378

Wakker B. P., van Woerden H., 1997, ARAA, 35, 217

Walch S. K., Whitworth A. P., Bisbas T., Wünsch R., Hubber D., 2012, MNRAS, 427, 625

Wang L., Dutton A. A., Stinson G. S., Macciò A. V., Penzo C., Kang X., Keller B. W., Wadsley J., 2015, MNRAS, 454, 83

Wang J., Koribalski B. S., Serra P., van der Hulst T., Roychowdhury S., Kamphuis P., Chengalur J. N., 2016, MNRAS, 460, 2143

Weiner B. J., et al., 2009, ApJ, 692, 187

Weinmann S. M., van den Bosch F. C., Yang X., Mo H. J., 2006, MNRAS, 366, 2

Werk J. K., et al., 2014, ApJ, 792, 8

Woods R. M., Wadsley J., Couchman H. M. P., Stinson G., Shen S., 2014, MNRAS, 442, 732

Zweibel E. G., McKee C. F., 1995, ApJ, 439, 779

van den Bosch F. C., 2001, MNRAS, 327, 1334

von Glasow W., Krause M. G. H., Sommer-Larsen J., Burkert A., 2013, MNRAS, 434, 1151

Chapter 5

ΛCDM is Consistent with SPARC Acceleration Law

Reprinted from B.W. Keller & J.W. Wadsley The Astrophysical Journal Letters *Volume 835, Issue 1, pp. 17-22, DOI:10.3847/2041-8213/835/1/L17 Published by The American Astronomical Society.*

Abstract

Recent analysis (McGaugh et al., 2016) of the SPARC galaxy sample found a surprisingly tight relation between the radial acceleration inferred from the rotation curves, and the acceleration due to the baryonic components of the disc. It has been suggested that this relation may be evidence for new physics, beyond ΛCDM. In this letter we show that 32 galaxies from the MUGS2 match the SPARC acceleration relation. These cosmological simulations of star forming, rotationally supported discs were simulated with a WMAP3 ΛCDM cosmology, and match the SPARC acceleration relation with less scatter than the observational data. These results show that this acceleration relation is a consequence of dissipative collapse of baryons, rather than being evidence for exotic dark-sector physics or new dynamical laws.

5.1 Introduction

For nearly a century, observations of kinematics in galaxies and clusters of galaxies have found large velocities inconsistent with the luminous matter within them. Even when thorough, comprehensive surveys of the baryonic mass within galaxies and clusters have been performed, most of the matter has been found to be missing. Zwicky (1937) presented observations of galaxy velocity dispersions in the Coma cluster, and proposed that the bulk of that cluster's mass was some sort of dark matter (DM). Later, the groundbreaking observations of Rubin & Ford (1970) showed that this dark matter was also ubiquitous within disc galaxies like our own. Today, there is a wealth of evidence for cold dark matter, not just from galaxy kinematics, but from the formation of large-scale structure (Blumenthal et al., 1984), the cosmic microwave background power spectrum (Planck Collaboration et al., 2014), and the primordial abundances of elements after Big Bang Nucleosynthesis (Walker et al., 1991). Dark matter is now part of the standard cosmology, ΛCDM, in which most of the matter in our universe is in fact dark. Despite this, we still do not know the actual form that dark matter particles take. Both direct detection experiments and searches for dark matter annihilation have failed to conclusively observe these particles (Aprile et al., 2012), and as such, alternative explanations for the kinematics of galaxies have been proposed.

The Spitzer Photometry & Accurate Rotation Curves (SPARC) sample, presented in Lelli et al. (2016a) is a new set of observations and derived mass models for a large number of rotation-dominated galaxies. By using $3.6\mu m$ observations, the stellar mass can be estimated with great accuracy. The stellar mass is complemented with $21cm$ observations of HI to get a measure of the gas mass within the disc. The recent paper by McGaugh et al. (2016) analyzed this sample, and determined a relation between the observed radial acceleration determined from the rotation curve (g_{obs}), and the acceleration induced by the baryons observed in the disc (g_{bar}). McGaugh et al. (2016) found that for large values of g_{bar}, $g_{obs} \sim g_{bar}$, while for values of $g_{bar} \lesssim 10^{-10} m\ s^{-2}$, the observed acceleration begins to rapidly outstrip the acceleration one would expect from the observed baryons. They find that the relation between g_{bar} and g_{obs} is well fit by:

$$g_{obs} = \frac{g_{bar}}{1 - \exp\left(-\sqrt{g_{bar}/g_{\dagger}}\right)}, \tag{5.1}$$

where $g_{\dagger} = 1.20 \pm 0.26 \times 10^{-10}\ ms^{-2}$. In addition to the simple functional form, McGaugh et al. (2016) find a surprisingly low scatter in this relation, with residuals normally distributed with $\sigma = 0.11$ dex. The authors noted that this is the same functional form as the Modified Newtonian Dynamics (MOND) (Milgrom, 1983) acceleration law, which attempts to explain galaxy rotation curves without DM.

A correlation between the total acceleration seen in disc galaxies and the acceleration due only to baryons has been known for some time Sancisi (2004); McGaugh (2004). Until recently, this has primarily been examined through the Mass-Discrepancy Acceleration Relation (MDAR): g_{bar} vs. M_{tot}/M_{bar}. McGaugh et al. (2016) directly probes a more fundamental relation, the Radial Acceleration Relation (RAR), with number of improvements that reduce the observational uncertainties.

In discussing these results, McGaugh et al. (2016) offer three possible explanations for the tight relation.

1. The end point of galaxy formation with conventional (baryonic?) physics.
2. New dark sector physics coupling dark matter and baryons
3. New dynamical laws (such as MOND Tensor-Vector-Scalar Gravity (TeVeS) (Bekenstein, 2004), etc.)

This is not the first set of observations that appear to be in discordance with ΛCDM. N-body simulations of halo formation have found DM halos follow a universal, "cuspy" density profile (Navarro et al., 1996). Yet observations of dwarf galaxies in the local universe find flat, "cored" central densities (the "cusp-core problem", Walker & Peñarrubia 2011). Meanwhile, DM-only simulations were finding that the local group should contain thousands of dwarfs, in contrast to the dozens actually observed (the "missing satellites problem" Klypin et al. 1999). Many of these halos are large enough that suppression of star formation by reionization could not explain their absence from the observations (the "too big to fail" problem Boylan-Kolchin et al. 2011).

A common feature in each of these conflicts is the comparison of observations to simulations of galaxy formation that rely purely on N-body, DM-only simulations. We now know that the impact of baryonic physics, chief among them the feedback from massive stars and black holes, can have a dramatic effect on the star formation history (e.g. Keller et al. 2015) and density profile of galaxies (Mashchenko et al., 2006).

Multiple studies (Pontzen & Governato, 2012; Sawala et al., 2016, etc) have found these problems disappear when galaxies are simulated with gas dynamics, along with reasonable models for star formation, radiative cooling, and stellar feedback. This is what constitutes a modern theory of galaxy formation, the first of the three options offered to explain the RAR. Galaxies are formed through the gravitational collapse of collisional particles (gas) into a rotationally supported disc. Conservation of angular momentum, combined with star formation and feedback within that disc, leads to the observed scaling relations and galaxy properties we see today. Whether this can also reproduce the RAR has been yet to be demonstrated.

In this letter, we show that the apparent tension between models of galaxy formation in ΛCDM and the SPARC observations also evaporates when the collisional collapse of baryons is taken into account. We find that the $g_{obs} - g_{bar}$ relation for a set of pre-existing cosmological galaxy simulations, evolved in a conventional ΛCDM cosmology, matches the SPARC acceleration relation, with even tighter scatter than the observed sample.

5.2 The MUGS2 Sample

The McMaster Unbiased Galaxy Simulations 2 (MUGS2) sample is an unbiased, statistically representative set of 18 cosmological zoom-in simulations of $L*$ disc galaxies. These galaxies were simulated in a WMAP3 ΛCDM cosmology, with parameters $H_0 = 73\,\mathrm{km\,s^{-1}\,Mpc^{-1}}$, $\Omega_M = 0.24$, $\Omega_{bar} = 0.04$, $\Omega_\Lambda = 0.76$, and $\sigma_8 = 0.76$. The MUGS2 $z = 0$ halo masses range from $3.7 \times 10^{11}\,\mathrm{M_\odot}$ to $2.2 \times 10^{12}\,\mathrm{M_\odot}$, with disc masses ranging from $1.8 \times 10^{10}\,\mathrm{M_\odot}$ to $2.7 \times 10^{11}\,\mathrm{M_\odot}$. For more details on the creation of the MUGS2 initial conditions, see the original MUGS paper, Stinson et al. (2010). For more information on the simulations themselves, see Keller et al. (2015, 2016).

MUGS2 was simulated using the modern smoothed particle hydrodynamics code Gasoline (Wadsley et al., 2004; Keller et al., 2014). The simulations used metal line radiative cooling (Shen et al., 2010), as well as a simple Schmidt law for star formation. What sets MUGS2 apart from the original MUGS, aside from improved hydrodynamics, is the use of a physically motivated, first principles model for treating feedback from supernovae. (SNe). Originally presented in Keller et al. (2014), the superbubble model captures the effects of thermal conduction and evaporation between a hot, SNe heated bubble and a surrounding shell of cold, swept-up interstellar medium (ISM). This model was derived to allow unresolved superbubbles to radiatively cool at realistic rates, with no free parameters, while automatically capturing the effects of clustered SNe.

In addition to the central spirals, we also include a number of dwarf companions from the MUGS2 sample. As with McGaugh et al. (2016), we exclude galaxies that are experiencing significant tidal interactions. Joshi et al. (2016) showed that tidal interactions on infalling galaxies can occasionally be seen out to 3 virial radii, we select galaxies between 3 to 5 virial radii from the central spiral. We exclude halos beyond 5 virial radii because our zoom-in simulations do not contain gas particles at these distances. In order to limit the effects of poor resolution, and to ensure that each radial bin contains sufficient baryonic resolution, we select only galaxies that contain 100 or more star particles. This gives us an additional 14 galaxies at $z = 0$, for a total of 32 galaxies. The stellar, gas, and total virial masses for each of our galaxies is shown in table 5.1.

Galaxy	M_*	$M_{\rm gas}$	$M_{\rm vir}$
$g15807_3$	1.66×10^7	1.52×10^8	1.74×10^{10}
$g8893_1$	2.14×10^7	1.06×10^7	1.10×10^{10}
$g1536_2$	2.62×10^7	1.03×10^8	8.36×10^9
$g3021_1$	3.24×10^7	3.93×10^7	2.49×10^{10}
$g4145_3$	4.04×10^7	9.55×10^7	2.83×10^{10}
$g7124_1$	4.76×10^7	2.83×10^8	3.54×10^{10}
$g27491_1$	6.66×10^7	4.22×10^8	2.53×10^{10}
$g1536_1$	1.19×10^8	3.75×10^8	5.29×10^{10}
$g4145_2$	1.76×10^8	8.40×10^8	4.83×10^{10}
$g15807_2$	3.04×10^8	1.09×10^9	5.50×10^{10}
$g4145_1$	3.93×10^8	5.29×10^8	1.30×10^{11}
$g15807_1$	7.54×10^8	1.68×10^9	8.17×10^{10}
$g4720_1$	1.03×10^9	1.36×10^9	9.70×10^{10}
$g22437_1$	1.94×10^9	8.22×10^8	1.53×10^{11}
$g7124_0$	5.22×10^9	4.97×10^{10}	3.66×10^{11}
$g8893_0$	7.36×10^9	9.10×10^{10}	5.80×10^{11}
$g5664_0$	9.44×10^9	7.29×10^{10}	4.77×10^{11}
$g21647_0$	1.18×10^{10}	1.01×10^{11}	7.44×10^{11}
$g422_0$	1.51×10^{10}	1.24×10^{11}	7.62×10^{11}
$g28547_0$	1.59×10^{10}	1.67×10^{11}	9.85×10^{11}
$g1536_0$	1.86×10^{10}	1.04×10^{11}	6.49×10^{11}
$g24334_0$	2.55×10^{10}	1.53×10^{11}	1.02×10^{12}
$g3021_0$	3.63×10^{10}	1.51×10^{11}	9.78×10^{11}
$g19195_0$	7.15×10^{10}	9.34×10^{10}	1.01×10^{12}
$g22437_0$	9.03×10^{10}	7.31×10^{10}	8.52×10^{11}
$g22795_0$	1.06×10^{11}	4.55×10^{10}	8.52×10^{11}
$g15784_0$	1.30×10^{11}	1.14×10^{11}	1.31×10^{12}
$g4720_0$	1.42×10^{11}	5.51×10^{10}	1.02×10^{12}
$g4145_0$	1.50×10^{11}	8.09×10^{10}	1.19×10^{12}
$g25271_0$	1.56×10^{11}	7.87×10^{10}	1.25×10^{12}
$g27491_0$	1.88×10^{11}	2.08×10^{11}	2.14×10^{12}
$g15807_0$	2.14×10^{11}	1.75×10^{11}	2.03×10^{12}

Table 5.1: Redshift 0 properties of our simulated galaxies. All masses are in solar masses. Subscript 0 denotes the central galaxy.

5.2.1 Calculating Accelerations from MUGS2

In order to compare to the SPARC sample, we located the central halos using the AMIGA halo finder (Knollmann & Knebe, 2009). We center the halos using the shrinking sphere method described in Power et al. (2003). Next, in order to measure rotation curves of the galaxies face-on, we calculate the net angular momentum vector of all gas within 10 kpc of the center of the disk, and rotate our simulations such that this vector is orthogonal to the x-y plane. Accelerations were measured in 100 circular annuli 300 pc wide in the radial dimension. For dwarfs, we use 15 600 pc-wide annuli, as the dwarfs have much smaller scale lengths, and to avoid issues from poor sampling of the dark matter or baryon particles within the dwarfs. Accelerations were then calculated using a direct N-body summation of all of the particles in the halo on those particles within the annulus. Only the in-plane component of the acceleration was used, to better follow McGaugh et al. (2016). For g_{obs} (the observed acceleration), all particles (gas, stars, and DM) within the simulation were used. To calculate g_{bar}, we simply calculate the contributions from stars and gas, g_* and g_{gas}, so that $g_{bar} = g_* + g_{gas}$. For each of g_* and g_{gas}, we use a direct summation only on those particles (stars and gas respectively). This process of direct summation to calculate gravity is equivalent to the numerical solution to Poisson's equation used in McGaugh et al. (2016). The mass model in SPARC (Lelli et al., 2016a) included stellar masses estimated from 3.6 μm near infrared observations, and gas masses estimated using 21 cm observations of HI. These HI masses were converted to total gas masses using the simple equation $M_{gas} = 1.33M_{HI}$ to take into account Helium mass. As most of the divergence from the $g_{obs} = g_{bar}$ relation occurs where H_2 fractions are small, omitting this component of the mass does not significantly change these results. Rather than using the total gas mass from our simulations, we follow the HI-based estimate from SPARC by calculating accelerations due to gas using $1.33M_{HI}$, rather than M_{gas}. This is especially important near the outskirts of the galaxy, where the contribution to the baryonic mass from ionized gas in the ISM and circumgalactic medium is most significant, and we would find our results diverging from McGaugh et al. (2016) if we did not match their methods here. The HI fraction is calculated using the radiative cooling code within Gasoline, which relies on tabulated equilibrium cooling rates from CLOUDY (Ferland et al., 2013).

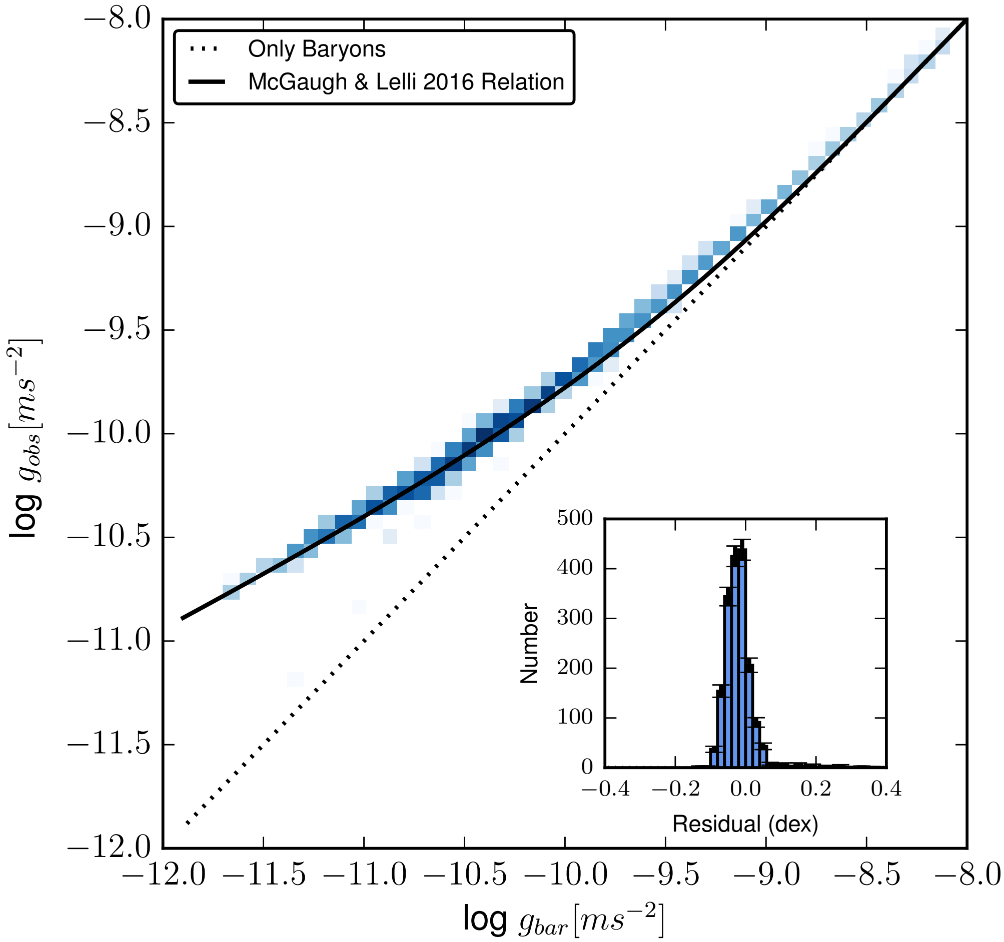

Figure 5.1: Total acceleration (g_{obs}) vs acceleration due to baryons (g_{bar}) from 2100 data points in the $z = 0$ MUGS2 sample, shown in the blue 2-dimensional histogram. The dotted black curve shows the 1:1 relation expected if the acceleration was due to baryons alone (without dark matter), while the solid line shows the relation presented in McGaugh et al. (2016). A Gaussian distribution fitted to these residuals finds a variance of $\sigma = 0.06$ dex, significantly lower than the 0.11 dex found by McGaugh et al. (2016).

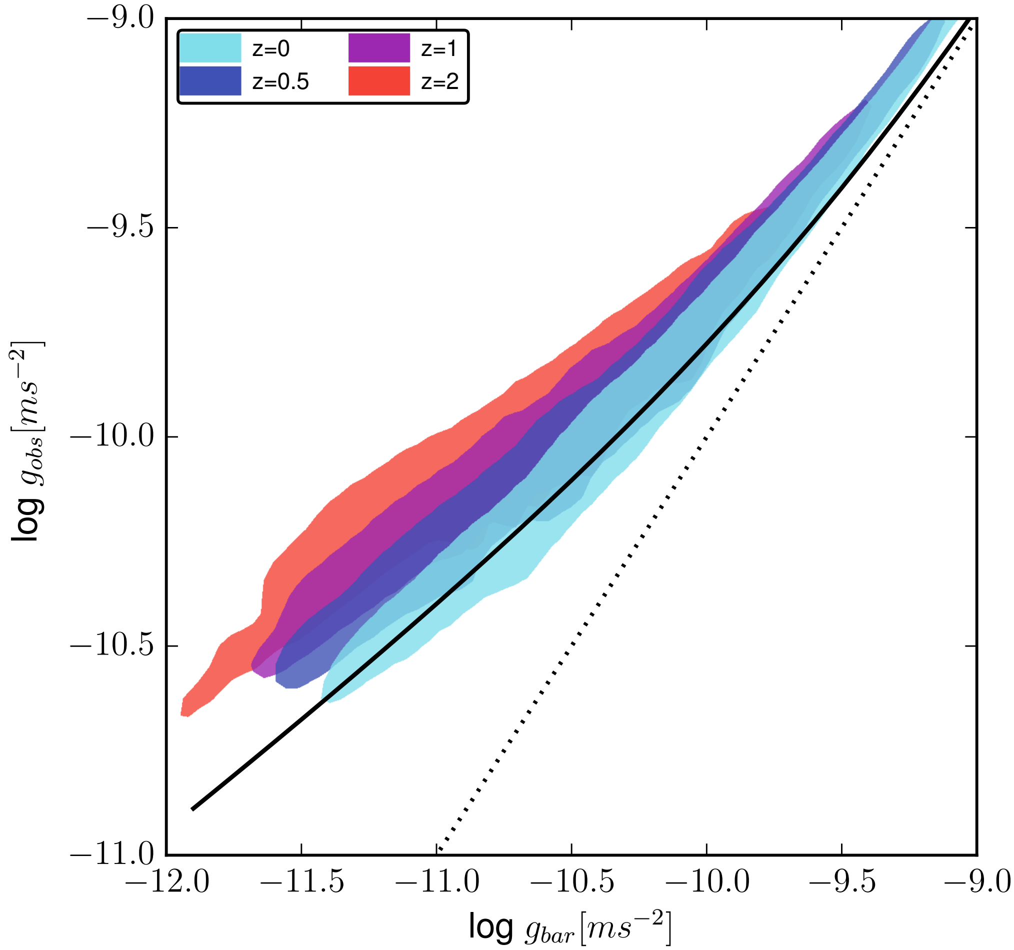

Figure 5.2: The simulated $g_{obs} - g_{bar}$ relation is not constant with redshift. As this figure shows, at higher redshift the low g_{bar} slope is much shallower than at $z = 0$. This shows that for high redshift galaxies, their discs can be depleted of baryons compared with $z = 0$. We have focused on the low g_{bar} end of the relation here, where the changes are most significant.

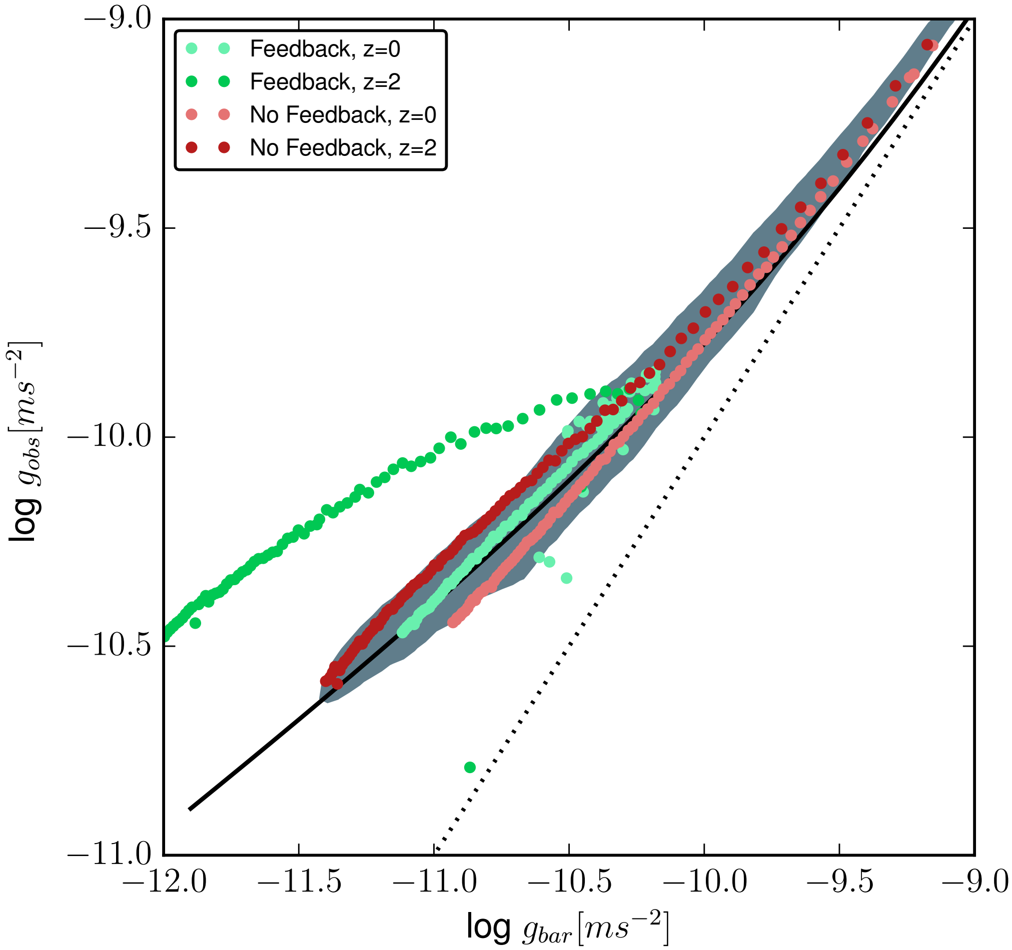

Figure 5.3: The evolution seen in figure 5.2 is primarily driven by feedback. This can be seen when looking at the same galaxy with and without feedback. Without feedback, the baryon fraction within the disc increases slightly from $z = 0$ to $z = 2$, but still roughly follows the RAR. At $z = 2$, strong outflows in the galaxy expel most of the baryons from the disc, flattening the acceleration relation. This effect is sensitive to the frequent merger-driven starbursts at high redshift, which can drive bursty outflows.

5.3 Results

5.3.1 z=0 Acceleration Relation

The MUGS2 sample gives us 2100 acceleration data points, just over 3/4 the sample size of McGaugh et al. (2016). Figure 5.1 shows the $g_{obs} - g_{bar}$ relation for the MUGS2 sample, compared both to the pure baryonic acceleration and the RAR. It is clear these simulated galaxies follow the McGaugh et al. (2016) relation *extremely* well. As can be seen from the inset residual distribution, our simulated galaxies follow the SPARC RAR even more tightly than the actual observational data. The scatter in our results, with $\sigma = 0.06$ dex, is consistent with the McGaugh et al. (2016) estimates. They decomposed their scatter of 0.11 dex into different sources, and when all of the observational uncertainties are removed, the remaining intrinsic scatter gives a variance of $\sigma = 0.06$ dex, very close to the value presented here here. A reduced χ^2 statistic of the SPARC relation fit to the $z = 0$ MUGS2 data finds a very good fit, with $\chi^2_\nu = 1.25$. These simulation data are fit by equation 5.1 at least as well as the original SPARC data.

5.3.2 Feedback & the Evolution of the Acceleration Relation

If the SPARC acceleration relation is in fact due to new physics, it would be surprising if the relation did not hold at all redshifts. This would not be the case if the relation was simply a consequence of galaxy evolution. In figure 5.2 we show that the acceleration relation in the MUGS2 sample actually shows significant redshift dependence, and only settles to the equation 5.1 relation near z=0. For these data points, we scaled the width of the annuli by the cosmic scale factor a, so that $\delta r = 300/(1+z)$ pc. This scaling ensures we are sampling primarily from the stellar disc, and not well beyond it. Omitting this scaling has little effect on these results, save for extending the points to very low values of g_{bar} and removing points from the high g_{bar} end. This evolution is a consequence of the huge impact that stellar feedback has on galaxies at $z \sim 2$. Keller et al. (2015) showed that SNe drive hot outflows from high redshift galaxies with mass loadings of $\dot{M}_{out}/\dot{M}_* \sim 10$. This leads to discs at high redshift with baryon fractions depleted relative to those at low redshift. This feedback effect is clear when a single galaxy, g1536, is compared to the same galaxy simulated without SNe feedback. As figure 5.3 shows, the redshift trend is nearly nonexistent without SNe feedback.

Even at $z = 2$, the galaxy without feedback falls within the scatter of the SPARC observations, and within the scatter of the $z = 0$ MUGS2 relation. This tells us that we need not invoke feedback processes to explain the $z = 0$ SPARC RAR. Simple dissipational collapse of gas is sufficient to produce a similar relation. The evolution as a function of redshift is therefore dominated primarily by the stronger effect of feedback at higher redshift.

5.4 Discussion

This paper is the first work to show that the RAR's acceleration scale and tight scatter, as reported by McGaugh et al. (2016), can be arise from fully self-consistent hydrodynamical simulations.

Efforts have been made in the past to explain related acceleration relations (the MDAR, the Baryonic Tully Fisher (BTFR) (McGaugh et al., 2000), etc.) with analytic arguments van den Bosch & Dalcanton (2000); Kaplinghat & Turner (2002), existing scaling relations (Di Cintio & Lelli, 2016), or hydrodynamical simulations (Santos-Santos et al., 2016). Analytic studies have found that the MOND-like scaling relations can arise as a consequence of exponential discs living within an an NFW halo (van den Bosch & Dalcanton, 2000). van den Bosch & Dalcanton (2000) showed that this can explain not only Tully-Fisher relation's relatively tight scaling over a large range of masses and surface densities (McGaugh & de Blok, 1998), but even explain the appearance of a characteristic acceleration in disk galaxy rotation curves (McGaugh, 1999).

Subsequent studies have suggested that an even harder constraint for ΛCDM to match is the tight scatter in the MDAR (Wu & Kroupa, 2015) or the RAR (Milgrom, 2016). A semi-empirical model recently published by Di Cintio & Lelli (2016) showed that both the BTFR and the MDAR can arise as a result of galaxies that follow a handful of scaling relations both for the baryonic content of the galaxy, as well as the dark matter halo it resided within. Both their model matches to the MDAR and the BTFR did show slightly higher scatter than the Lelli et al. (2016b) observations (0.17 vs. 0.11 (0.06 intrinsic) dex), which they suggest may be a result of the BTFR's sensitivity to measuring radius.

The BTFR and MDAR were also examined using galaxies from the MaGICC (Stinson et al., 2013) and CLUES (Gottloeber et al., 2010) simulations by Santos-

Santos et al. (2016). Their results also showed similar scatter to the MDAR reported in McGaugh (2014), with a scatter of $\sigma \sim 0.3$ dex.[1] This is significantly higher than the intrinsic scatter of 0.06 dex reported in McGaugh et al. (2016). This may be due to the use of a sample composed of simulations run using different subgrid physics prescriptions, which will naturally differ from one another. While matching the scatter of previous observations, which suffered from much higher observational uncertainties, matching both the fitting function and small intrinsic scatter of McGaugh et al. (2016) has never been done prior to this study.

Concurrently with the work presented here, Ludlow et al. (2016) presented a study using simulations from the EAGLE (Schaye et al., 2015) and APOSTLE (Sawala et al., 2016) projects. EAGLE and APOSTLE use a common set of subgrid physics. They found their simulations were fit well by the McGaugh et al. (2016) functional form of the RAR with $g_{\dagger} = 3 \times 10^{-10}\ ms^{-2}$ (well outside the uncertainties reported in McGaugh et al. (2016) for the value of $g_{\dagger}$). They also found that the z=0 relation is only somewhat sensitive to the subgrid physics model (as we have found as well). The fact that their $g_{\dagger}$ is larger than ours means EAGLE galaxies are somewhat baryon-depleted compared to ours. This, coupled with the lack of redshift evolution, suggests that the EAGLE feedback model drives stronger outflows at low redshift compared to the superbubble model used in MUGS2.

The EAGLE subgrid physics model is complex, and involves a number of different purely numerical parameters that were tuned to reproduce the observed stellar mass to halo mass relation (SMHMR) and size-mass relation, the details of which can be found in Crain et al. (2015). MUGS2 instead used a well-constrained, physically motivated model for SN feedback (Keller et al., 2014), with no free parameters beyond the energy available per supernovae, and which captures the effects of thermal evaporation that are ignored in EAGLE. This allows us to better capture the real variation that occurs in the efficiency of outflows over cosmic time (Keller et al., 2015; Muratov et al., 2015). Perhaps the clearest conclusion that can be drawn from the results of this paper and those of Ludlow et al. (2016) is that the scatter in the RAR will be fairly small regardless of the details of baryonic process like cooling, star formation, and feedback. However, the actual value of $g_{\dagger}$ *is* sensitive to these details, and the RAR may therefore be a useful new tool for constraining subgrid physics in galaxy

[1] While this number is not reported in McGaugh (2014), we have confirmed this value with Dr. McGaugh in private communication.

simulations.

5.5 Conclusion

We have shown here that the SPARC RAR can be produced by conventional galaxy formation in a ΛCDM universe. While we have used a pre-existing set of simulations, MUGS2, we expect a larger sample designed to match SPARC should find similar results. Neither the particular functional form (equation 5.1) nor the small scatter about this relation requires anything beyond the dissipational collapse of baryons in a DM halo. We predict the fit observed at $z = 0$ will not hold at all redshifts: vigorous feedback at high redshift acts to scour protogalaxies of their baryons, reducing the baryon fraction of the disc, flattening the $g_{obs} - g_{bar}$ relation. Stellar feedback is an essential process if we are to produce realistic galaxies. In order for a single RAR to hold at all redshifts, feedback efficiencies would have to be so low as to produce galaxies with stellar masses and bulge fractions in conflict with the observed SMHMR, and the observed kinematics of local galaxies. If one wished to use equation 5.1 to fit galaxies at all epochs, $g_\dagger$ would need to have a significant redshift dependence. If, on the other hand, high redshift observations of the $g_{obs} - g_{bar}$ relation found no evolution in shape, or a steeper slope at low g_{bar}, this would in fact constitute a serious disagreement with ΛCDM, as it would be difficult to produce the observed low cosmic star formation efficiency without strong outflows removing baryons from high redshift discs.

As figure 5.3 shows, the $z = 0$ SPARC relation is *not* a result of stellar feedback. While feedback does change the relationship at high redshift, its general form is reproduced by simple gas collapse and radiative cooling. This is one of the few apparent problems in ΛCDM that *doesn't* require feedback for its resolution!

Acknowledgements

We thank Hugh Couchman, Stacy McGaugh, and Laura Parker for valuable discussion and suggestions. The simulations used here were performed on SCINET, part of ComputeCanada. We appreciate these computing allocations. We also thank NSERC for funding support.

Bibliography

Aprile E., et al., 2012, Physical Review Letters, 109, 181301

Bekenstein J. D., 2004, Phys. Rev. D, 70, 083509

Blumenthal G. R., Faber S. M., Primack J. R., Rees M. J., 1984, Nature, 311, 517

Boylan-Kolchin M., Bullock J. S., Kaplinghat M., 2011, MNRAS, 415, L40

Crain R. A., et al., 2015, MNRAS, 450, 1937

Di Cintio A., Lelli F., 2016, MNRAS, 456, L127

Ferland G. J., et al., 2013, RMxAA, 49, 137

Gottloeber S., Hoffman Y., Yepes G., 2010, preprint, (arXiv:1005.2687)

Joshi G. D., Parker L. C., Wadsley J., 2016, MNRAS, 462, 761

Kaplinghat M., Turner M., 2002, ApJ, 569, L19

Keller B. W., Wadsley J., Benincasa S. M., Couchman H. M. P., 2014, MNRAS, 442, 3013

Keller B. W., Wadsley J., Couchman H. M. P., 2015, MNRAS, 453, 3499

Keller B. W., Wadsley J., Couchman H. M. P., 2016, MNRAS,

Klypin A., Kravtsov A. V., Valenzuela O., Prada F., 1999, ApJ, 522, 82

Knollmann S. R., Knebe A., 2009, ApJS, 182, 608

Lelli F., McGaugh S. S., Schombert J. M., 2016a, preprint, (arXiv:1606.09251)

Lelli F., McGaugh S. S., Schombert J. M., 2016b, ApJ, 816, L14

Ludlow A. D., et al., 2016, preprint, (arXiv:1610.07663)

Mashchenko S., Couchman H. M. P., Wadsley J., 2006, Nature, 442, 539

McGaugh S., 1999, in Merritt D. R., Valluri M., Sellwood J. A., eds, Astronomical Society of the Pacific Conference Series Vol. 182, Galaxy Dynamics - A Rutgers Symposium. (arXiv:astro-ph/9812327)

McGaugh S. S., 2004, ApJ, 609, 652

McGaugh S., 2014, Galaxies, 2, 601

McGaugh S. S., de Blok W. J. G., 1998, ApJ, 499, 41

McGaugh S. S., Schombert J. M., Bothun G. D., de Blok W. J. G., 2000, ApJ, 533, L99

McGaugh S., Lelli F., Schombert J., 2016, preprint, (arXiv:1609.05917)

Milgrom M., 1983, ApJ, 270, 371

Milgrom M., 2016, preprint, (arXiv:1609.06642)

Muratov A. L., Kereš D., Faucher-Giguère C.-A., Hopkins P. F., Quataert E., Murray N., 2015, MNRAS, 454, 2691

Navarro J. F., Frenk C. S., White S. D. M., 1996, ApJ, 462, 563

Planck Collaboration et al., 2014, A&A, 571, A16

Pontzen A., Governato F., 2012, MNRAS, 421, 3464

Power C., Navarro J. F., Jenkins A., Frenk C. S., White S. D. M., Springel V., Stadel J., Quinn T., 2003, MNRAS, 338, 14

Rubin V. C., Ford Jr. W. K., 1970, ApJ, 159, 379

Sancisi R., 2004, in Ryder S., Pisano D., Walker M., Freeman K., eds, IAU Symposium Vol. 220, Dark Matter in Galaxies. p. 233 (arXiv:astro-ph/0311348)

Santos-Santos I. M., Brook C. B., Stinson G., Di Cintio A., Wadsley J., Domínguez-Tenreiro R., Gottlöber S., Yepes G., 2016, MNRAS, 455, 476

Sawala T., et al., 2016, MNRAS, 457, 1931

Schaye J., et al., 2015, MNRAS, 446, 521

Shen S., Wadsley J., Stinson G., 2010, MNRAS, 407, 1581

Stinson G. S., Bailin J., Couchman H., Wadsley J., Shen S., Nickerson S., Brook C., Quinn T., 2010, MNRAS, 408, 812

Stinson G. S., Brook C., Macciò A. V., Wadsley J., Quinn T. R., Couchman H. M. P., 2013, MNRAS, 428, 129

Wadsley J. W., Stadel J., Quinn T., 2004, New Astronomy, 9, 137

Walker M. G., Peñarrubia J., 2011, ApJ, 742, 20

Walker T. P., Steigman G., Kang H.-S., Schramm D. M., Olive K. A., 1991, ApJ, 376, 51

Wu X., Kroupa P., 2015, MNRAS, 446, 330

Zwicky F., 1937, ApJ, 86, 217

van den Bosch F. C., Dalcanton J. J., 2000, ApJ, 534, 146

Chapter 6

Conclusion & Future Work

This thesis has explored the effects of SN feedback in the formation of galaxies like our own. Supernovae produce extremely hot ejecta ($T > 10^8$ K) that rapidly shocks and expands against the significantly under-pressured surroundings. As massive stars form in clusters, these individual SN remnants merge together, forming a superbubble. These superbubbles are much more effective at pushing and heating the ISM than an equivalent amount of energy distributed as individual SN. The primary mechanism that sets the temperature of these superbubbles is the evaporation of cold gas, driven by thermal conduction. Thermal conduction becomes effective above 10^5 K, and strongly self-limits the temperature of superbubbles to $\sim 2 - 5 \times 10^6$ K. In this thesis, we have developed a new model for SN feedback that takes into account these previously ignored superbubble processes, and used that model to study the growth and evolution of star-forming galaxies. This model allowed us to see how SN can (and cannot!) regulate the flow of gas into and out of galaxies, where it may forms stars. Previous work (Stinson et al., 2013; Hopkins et al., 2014) has suggested that star-forming galaxies could only regulate their growth if SN feedback was augmented with early feedback from radiation pressure, stellar winds, and UV heating. With careful, physically motivated feedback models, we have now shown that this is not the case: the additional energy & free parameters provided by early feedback are not necessary. The primary insight this thesis provides is that the processes which mix feedback-heated gas with the ISM (i.e. thermal evaporation) are just as important as the amount of energy provided by feedback. Neither can be omitted if one wishes to construct an accurate simulation of galaxy formation.

In Chapter 2, we presented a detailed description of the new superbubble model, implemented in the SPH code Gasoline2. We rely on the strongly self-limiting process of thermal evaporation (Cowie & McKee, 1977), where cold mass is evaporated into a hot bubble at a rate strongly dependent on the temperature of the hot bubble. This drives the interior of the bubble to a temperature of a few 10^6 K, evaporating material more or less rapidly as the temperature dips above or below this value. This is the characteristic temperature for SN-heated gas. We use this physics to develop a new model for SN feedback, which gives realistic estimates for cooling in unresolved hot bubbles, and accurately calculates the mass loading of SN energy. We demonstrated that this model is insensitive to resolution, unresolved ISM structure, and uncertain (tangled?) magnetic fields. The strong temperature dependence of thermal evaporation means that significant changes to the conduction rate coefficient (such as the suppression by magnetic fields) result in only slight changes to the equilibrium temperature of feedback-heated gas. Finally, after investigating the behaviour of individual bubbles, we showed that superbubble feedback is more effective at both regulating star formation and at driving galactic winds in isolated disc and dwarf galaxies.

Isolated disc simulations, like that shown in chapter 2, lack a full cosmological history. To see how SN feedback can impact the overall growth and history of a galaxy like the Milky Way, we needed to simulate the galaxy from high redshift to the present. In chapter 3, we use zoom-in cosmological simulations (Navarro & White, 1993) of a Milky Way-like galaxy to compare the effects of different feedback models. The galaxy, when simulated using our new superbubble model, was able to produce a realistic stellar mass fraction for the galaxy's entire history. Not only did the galaxy simulated with superbubble feedback have the correct stellar mass, we showed that it also was effectively bulgeless, with a unpeaked, flat rotation curve. These two properties arose via a single process. At high redshift, superbubble feedback efficiently drives heavily mass-loaded winds, expelling gas from the ISM of the galaxy. The gas that forms a stellar bulge is accreted at high redshift, meaning that these winds preferentially remove low angular momentum material, while preserving the gas with high angular momentum. Thus, superbubble feedback is able to naturally prevent both runaway star formation and the formation of a bulge through these winds. Higher-resolution simulations of wind venting will help to determine if these mass loadings are realistic, and to remove additional uncertainty that arises from a marginally-resolved ISM.

While a single galaxy can be a useful case study, multiple objects must be studied in order to look at population-scale effects. Chapter 4 extends the results of chapter 3 by simulating an additional 17 objects, and uses these simulations to examine if SN regulation can operate effectively in galaxies both heavier and lighter than the Milky Way. With this new sample (the McMaster Unbiased Galaxy Simulations 2, or MUGS2), we were able to demonstrate a critical mass at which SN regulation of gas accretion and star formation breaks down. Simulated galaxies that exceed this mass ($\sim 10^{12}\,\mathrm{M}_{\odot}$) overproduce stars, most of which form in a dense stellar bulge. All of this arises due to a fundamental relation between the mass loading of superbubble-driven winds and the mass of the galaxy. When the escape velocity of the disc exceeds the sound speed of superbubble-heated gas (which has a characteristic temperature of

$\sim 3 \times 10^6$ K), only outflows which have entrained less material are able to escape the galaxy. This leads to less gas ejection, and a shutdown of regulation. This shutdown occurs exactly at the galaxy mass where powerful AGN are observed, and it results in a vigorous transport of gas to the nucleus of the galaxy. This makes these results strong evidence that this shutdown is a key component in the "hand-off" between SN and AGN feedback.

The MUGS2 simulations produced in chapter 4 contain a wealth of data useful for future studies. Chapter 5 applied the MUGS2 galaxies produced in Keller et al. (2016) to examine the radial acceleration relation (RAR) derived by McGaugh et al. (2016) from observations in the SPARC (Lelli et al., 2016) catalog. We found that the tight relation seen in the SPARC data does not require new fundamental physics (such as self-interacting dark matter, modified gravity, or MOND). Instead, the simple combination of dissipational collapse with angular momentum conservation produces the RAR. This means that even galaxies where SN fail to regulate their star formation (or even where SN are omitted altogether) fall on the same observed relation. This was the first published demonstration that ΛCDM could produce the RAR, using untuned simulations made prior to the publication of McGaugh et al. (2016).

This thesis has shown that, with correct modelling, SN feedback can regulate the growth of galaxies up to the mass of the Milky Way, but no further. In galaxies below this mass, SN efficiently drive galactic winds, primarily at high redshift, which act to limit the availability of low angular momentum gas, slowing the formation of stars and the stellar bulge. Without the feedback from SMBHs, galaxies more massive than ours form far too many stars, primarily in a concentrated central bulge. The transition from SN to AGN feedback occurs due to a rapid drop in the effectiveness of SN-driven outflows. Finally, we showed that independent of the detailed internal processes of galaxy evolution, the acceleration relation observed by McGaugh et al. (2016) is simply a natural consequence of galaxy formation, removing what could have been potential tension with ΛCDM cosmology.

6.1 The Impact and Context of these Results

6.1.1 How Clustered Supernovae Heat The ISM

Supernovae provide an enormous source of energy. Simple accounting shows that the energy released from a stellar population can eject more gas from a galaxy disc than the mass of the population itself, if that energy couples to enough mass before radiating away (Larson, 1974). Radiative losses may be significant if SN detonate in a sufficiently dense environment, with cooling times as short as a few thousand years (Chevalier, 1974). However, when massive stars form in clusters, bubbles of shocked stellar wind and SN ejecta merge to form a superbubble. These superbubbles have significantly longer cooling times (Mac Low & McCray, 1988), and can deposit an order of magnitude more energy and momentum into the ISM before cooling (Gentry et al., 2017). How these superbubbles drive the outflows that regulate the formation of stars within the galactic disc depends on the mass loading of these outflows. This global outflow mass loading depends heavily on the local mass loading: how much mass is mixed into a superbubble before it vents from the galaxy.

The question of local mass loading has been explored before in simulation. Thacker & Couchman (2000) presented a survey of methods for depositing feedback energy. Their work showed that choosing to deposit feedback energy into single resolution elements vs. smoothing it over multiple elements had a significant impact on whether that feedback energy could couple to the ISM without radiating away. Thacker & Couchman (2000) advocated the use of a brief adiabatic period, similar to the delayed cooling model used in Stinson et al. (2006) to prevent overcooling when feedback energy was smoothed. A more recent study by Dalla Vecchia & Schaye (2012) directly examined the question of local mass loading with a model that used the temperature of post-feedback gas as a single tunable parameter. This is effectively the same as choosing the amount of mass that each SN heats (the local mass loading). They found that lower mass loadings result in hotter post-feedback gas, with longer cooling times, and subsequently much more effective SN feedback. The Keller et al. (2014) superbubble model relies on a physical mechanism (thermal evaporation) for determining this mass loading. Previous feedback models have been designed primarily to avoid the overcooling that can occur when this mass loading is too high: superbubble feedback instead attempts to calculate the correct local mass loading, and allows the feedback-heated gas to cool with realistic temperatures and densities. The amount of material heated by feedback is as important as the energy available from feedback. On a galactic scale, too-high mass loadings may mean that more material is ejected from the disc, but at lower overall temperatures and velocities. This material will re-accrete on shorter timescales than hotter ejecta, increasing the star formation rate. Conversely, too-low mass loading will give hot, high-entropy outflows that leave the disc efficiently and re-accrete much later (if at all). As these outflows contain little mass, the ISM that remains will still be able to form stars effectively, again increasing the star formation rate. The results we presented here show that thermal evaporation gives a mass-loading rate between these two extremes, allowing effective outflows for galaxies up to $M_{vir} \sim 10^{12}$ M$_\odot$.

As we showed in Keller et al. (2015), including thermal evaporation in simulations of a Milky Way-like galaxy drastically changes the effectiveness of SN-driven galactic winds. Starving the galaxy of gas (either through ejection of accreted gas, or prevention of accretion) is the only effective mechanism for regulating star formation on cosmic timescales (Kereš et al., 2009). To prevent the formation of bulges larger than the ones seen in Milky Way-like galaxies, bulge-forming (low-angular momentum) gas must be removed from the ISM. As SN-driven winds are most effective at high redshift, when this material is mostly accreted, the outflows driven from the galaxy preferentially remove bulge-forming gas. A similar result was seen in simulations of dwarf galaxies (Governato et al., 2010; Brook et al., 2011), but Keller et al. (2015) has shown that bulgeless disc galaxies similar to the Milky Way can be produced through the same mechanism, and that this mechanism simultaneously regulates star formation. An important conclusion of this study is that much of the past work (Stinson et al., 2013; Agertz et al., 2013; Hopkins et al., 2014) showing that SN feedback was unable to regulate star formation without the addition of "early feedback" from radiation pressure, stellar winds, or photoionization was likely underestimating the effectiveness of SN. Since many of these studies used simpler, more numerically-sensitive feedback models that also omitted thermal evaporation, they were unable to effectively drive sufficient mass into hot, high-entropy gas that could leave the galaxy. This study tells us that the disc-dominant morphology and low stellar fraction in galaxies like our own all arise from the same mechanism: heavily mass loaded winds at high redshift.

6.1.2 The Challenge of Modelling Feedback

Developing a versatile, accurate, resolution-insensitive model for SN feedback has been a challenge in galaxy simulations for decades (Katz, 1992; Rosdahl et al., 2016). While a number of recent models have been developed that are able to produce galaxies which match some observables, all of these models have relied on weakly constrained numerical parameters to enhance the effectiveness of feedback and counter the losses due to limited resolution. Rosdahl et al. (2016) illustrated this clearly, in a recent comparison project. This paper implemented 5 popular feedback algorithms in the RAMSES code: simple thermal dumps; a delayed cooling model similar to Agertz et al. (2013); a kinetic model similar to Dalla Vecchia & Schaye (2008); a stochastic thermal model based on Dalla Vecchia & Schaye (2012); and a hybrid model from Kimm et al. (2015). Each of these models, with "fiducial" parameter choices, produced star formation rates that varied by nearly an order of magnitude in the Kennicutt (1998) star formation relation. On top of that, the galaxies showed marked morphological differences and over 3 orders of magnitude of variation in the average wind mass loadings.

With previous models for stellar feedback, both the qualitative behaviour as well as the precise, quantitative effects have been heavily determined by poorly constrained numerical parameters. This has made interpreting the results of simulations difficult, as it is unclear which effects are a result of the underlying physics and which are simply a result of the choice of parameters used for the simulation. Physics-driven, parameter-free models help to remove this ambiguity, and allow us to produce simulations that better match reality.

6.1.3 Feedback Beyond Supernovae

Subgrid models are essential for including feedback from sources other than SN as well. Non-supernovae mechanisms for launching outflows and regulating star formation are now frequently studied with numerical simulations. Radiation pressure has been examined in a number of studies (Hopkins et al., 2014; Roškar et al., 2014; Agertz & Kravtsov, 2015) using fairly simple treatments, without full radiative transport. These simulations have included various models for feedback from SN and stellar winds, and have not yet converged on a consensus regarding the effects of radiation. However, both Roškar et al. (2014) and Agertz & Kravtsov (2015) found that the optical depths required for radiation pressure to drive effective outflows produce unrealistic galaxy morphologies. The effects of cosmic rays are beginning to be examined in simulations with (Girichidis et al., 2016) and without (Jubelgas et al., 2008; Booth et al., 2013) treatments for magnetohydrodynamics. Most simulations have found that cosmic rays are unable to drive sufficiently mass-loaded outflows from Milky Way-like galaxies, but may be important both for dwarf galaxies and launching the cold, dusty phases of outflows in larger galaxies. With a better constrained SN model, these mechanisms can now be re-examined with greater control, allowing SN and other effects to be disentangled.

It has been suggested by numerous studies (Benson et al., 2003; Bower et al., 2006) that AGN feedback is critical to shaping the galaxy luminosity function. Most observations (Kauffmann et al., 2003) show that strong AGN are hosted in galaxies with halo masses slightly greater than $\sim 10^{12}\ M_{\odot}$. By simulating a collection of galaxies that bracket this mass, but omitting the effects of AGN feedback, we were able to show that SN alone break down as a mechanism of regulating star formation in these massive galaxies. Importantly, this also results in large angular momentum transport for gas within the disc, funneling material to the central regions where SMBHs reside. This, combined with the failure of SN-driven galactic winds, suggests that SN are actually the mechanism that determines where powerful AGN occur, a mechanism that has begun to be studied in Bower et al. (2016).

6.1.4 Baryonic Physics & Feedback in Tests of Cosmology

Chapter 5 presented the first simulation result to reproduce the McGaugh et al. (2016) RAR. A later study (Ludlow et al., 2016) used data from the EAGLE (Schaye et al., 2015) and APOSTLE (Sawala et al., 2016) simulations and confirmed both the fit to the RAR, and the insensitivity to feedback that we found. Earlier, a semi-empirical model used by Di Cintio & Lelli (2016) showed that a related observation, the mass-discrepancy acceleration relation, could be produced simply as a result of other pre-existing scaling relations. Taken together, these results should seriously temper attempts to fit/explain the RAR using new, exotic physics. If conventional baryonic physics produces the same relation in a ΛCDM cosmology, there is little need to turn to modified gravity (Moffat, 2016; Verlinde, 2016; Burrage et al., 2016) to explain it.

Tests of cosmology are moving to scales where the effects of baryonic physics are becoming more pronounced. Comparisons between the predictions of collisionless structure formation have found that CDM produces far more dwarf galaxies than those we observe in the local group (Klypin et al., 1999; Boylan-Kolchin et al., 2011). Observations of the dwarves we do see shows their density profiles have flattened "cores", suggesting they are depleted in dark matter within the inner few kpc (Moore, 1994; Simon et al., 2005). While alternative forms of dark matter may reproduce these observations (Spergel & Steinhardt, 2000; Avila-Reese et al., 2001), it is notable that what appear to be tension between CDM simulations and the observations is actually tension between *collisionless* CDM simulations and the observations. In dwarf galaxies, the effects of stellar feedback are extremely important, with a handful of supernovae capable of ejecting the entire ISM. When these effects are taken into account, much of the apparent tension disappears (Mashchenko et al., 2006; Pontzen & Governato, 2012; Sawala et al., 2016). On galaxy scales, ΛCDM predictions *must* include the details of baryonic effects, including feedback.

6.2 Further Questions & Future Directions

The results presented in this thesis have clarified the impact of SN feedback, but also raised some questions. While we now know how SN act to regulate the growth of stars in galaxies up to the mass of the Milky Way, details about the transition to AGN regulation at high mass are still unclear. The outflows that shape the galaxy contain detailed, multiphase structure that is unresolved in our simulations. How exactly mass is entrained within these outflows and how that material is recycled back into the disc will require further study. Additionally, the small sample of 18 galaxies we studied in chapters 4 and 5 are a tiny fraction of the range of mass, morphology and environment in real galaxies. How does superbubble feedback work to shape the scaling relations seen in galaxies both more and less massive than the ones we have seen here? The results of chapter 4 suggest that feedback from AGN is a critical process for more massive galaxies. How does this mechanism work in tandem with SN to regulate the formation of massive galaxies?

6.2.1 Launching Multiphase Galactic Winds

One of the biggest questions raised in chapter 4 was the origin of the scaling relation between outflow mass loadings and disc mass. Observations of galactic winds tell us that they are multiphase (Stark & Carlson, 1984; Wakker & van Woerden, 1997), containing ionized, neutral, and molecular gas. This structure is unresolved in our simulations, and may ultimately be important to the cooling rates and recycling times for these outflows. Complete, detailed observations of outflowing material in the CGM are difficult. This gas tends to be too cool and diffuse to be a strong emitter of X-rays, and absorption line studies require the lucky coincidence of a background quasar (Weiner et al., 2009). The presence of cold clouds in particular is a significant problem for theories of galactic wind launching. Analytic calculations and high resolution simulations suggest that these clouds should be disrupted and mixed on timescales far shorter than is required to ballistically launch them into the CGM. In light of this, why do we see these clouds? They may be formed in-situ, or may be launched by the fragmentation of superbubble shells, already accelerated to high velocities during the momentum-conserving snowplow phase of the bubble's growth (Lagos et al., 2013). These processes all take place on length scales far below what is resolvable in the cosmological simulations we have presented here. High resolution simulations of superbubble breakout from the ISM will be able to tell us what indeed is the origin of these clouds. Understanding the details of the multiphase CGM is key to understanding how galaxies accrete and expel gas, as thermal instability in the CGM (which depends heavily on its density, temperature, and metallicity) may be the mechanism by which spiral galaxies today acquire the gas required to form new stars (Marasco et al., 2012).

A related question to the detailed, large-scale breakout of galactic winds from the ISM is the detailed, small scale breakout of SN from their natal environments. Studies have already been published examining the destruction of molecular clouds by stellar winds and ionizing radiation (Murray et al., 2010; Walch et al., 2012). Only a handful have focused on how SN-heated gas can escape from molecular clouds (Rogers & Pittard, 2013), and these have looked at very controlled, simple initial clouds. The transition between individual SN in a molecular cloud and the growth of a new superbubble is important to determining the maximum efficiency of SN, and how much of the 10^{51} erg released per SN is lost before a superbubble can begin to form.

This, like the evolution of cold clumps in galactic winds, will require high-resolution simulations of star formation within realistic molecular clouds. Studies have begun (Dobbs, 2015) to study molecular clouds selected from global disc simulations and re-simulated at higher resolution. Combining these kinds of simulations with models for small-scale star formation, feedback from stellar winds and massive stars, as well as thermal conduction and evaporation will allow us to determine a more accurate energy budget for stellar feedback.

6.2.2 Scaling Relations in Galaxy Populations

The MUGS2 sample has been simulated with a robust, physically motivated model for SN feedback, using initial conditions without selection bias in either merger history or spin parameter. Despite this, with a relatively limited range of halo masses ($\sim 4 \times 10^{11} - 2 \times 10^{12}\ M_{\odot}$), we are unable to probe the evolution of the large population of galaxies observed, which span many orders of magnitude in mass. Modern large volume simulations like Illustris (Vogelsberger et al., 2014) and EAGLE (Schaye et al., 2015) contain $> 10^6$ individual galaxies, spanning a range of masses that include both galaxies lighter and more massive than those we have studied here. These larger sample sizes are essential to understanding how whole populations of galaxies evolved from the earliest linear structures. While these simulations contain models for star formation, feedback from both stars and AGN, as well as radiative cooling, these have all been fine-tuned to fit observed scaling relations. This limits the ability of these simulations to explain the origins of the observations they have been tuned to fit. The superbubble model contains no free/tuned parameters, and accurately follows the evolution of feedback-heated gas as it evaporates cool material that surrounds it. It is the only feedback model currently in existence that captures the important physical process of thermal conduction and evaporation. It will allow us to build a statistically significant sample of physically realistic galaxies.

6.2.3 Feedback from AGN

While observational evidence abounds for the existence of SMBHs (Kormendy & Ho, 2013), and the impact of the AGN they power (Veilleux et al., 2005), there is still great uncertainty as to how they regulate their own growth, and the growth of the galaxies they live in. We have found that a transition must occur between galaxies regulated by SN feedback to AGN feedback as they grow heavier than the Milky Way. How this handoff occurs remains widely unexplored. The superbubble feedback model is agnostic to the source of heating: it simply captures the effect of evaporation between unresolved hot and cold gas. It's therefore equally well-suited to model the effect of heating from AGN as it is for heating from SN. Using superbubble feedback, along with new models for SMBH growth (Hopkins & Quataert, 2010) and migration (Tremmel et al., 2015), we will be able to simulate the growth of SMBHs in galaxies with greater confidence, using physically motivated feedback and accretion models. This will allow us to study the full gamut of galaxies that exist, and study how the tight scaling relations between stellar bulges and SMBHs might arise.

6.3 Final Thoughts

Less than a century ago, even the most basic nature of external galaxies was contentious. Prominent astronomers argued "spiral nebulae" were members of our own galaxy, the Milky Way. Today, we stand on the shoulders of past observers, theorists, and simulators in constructing a self-consistent theory of galaxy formation. Previous generations have painted a picture of galaxy formation as gravitational collapse through hierarchical, bottom-up merging. The details of how stars form within galaxies remains unclear. A puzzling & important question is the inefficiency of star formation at all scales. This thesis has explored one mechanism for this inefficiency, feedback by SN . Thermal conduction is critical to evaporating the star-forming ISM into hot outflows that starve young, high-redshift galaxies of star formation fuel. This mechanism is effective in galaxies up to the mass of our own; it breaks down in more massive galaxies. This tells us two important facts about how galaxies evolve. First, it tells us that SN alone may regulate star formation in galaxies with $M_{vir} < 10^{12}\,\mathrm{M}_{\odot}$. Second, it tells us that SN *cannot* be the only source of energy that regulates the formation of massive galaxies. While many questions remain about the processes that govern the life cycle of galaxies, the results shown here help us to understand one of the major process: how SN regulate galaxy formation.

Bibliography

Agertz O., Kravtsov A. V., 2015, ApJ, 804, 18

Agertz O., Kravtsov A. V., Leitner S. N., Gnedin N. Y., 2013, ApJ, 770, 25

Avila-Reese V., Colín P., Valenzuela O., D'Onghia E., Firmani C., 2001, ApJ, 559, 516

Benson A. J., Bower R. G., Frenk C. S., Lacey C. G., Baugh C. M., Cole S., 2003, ApJ, 599, 38

Booth C. M., Agertz O., Kravtsov A. V., Gnedin N. Y., 2013, ApJ, 777, L16

Bower R. G., Benson A. J., Malbon R., Helly J. C., Frenk C. S., Baugh C. M., Cole S., Lacey C. G., 2006, MNRAS, 370, 645

Bower R., Schaye J., Frenk C. S., Theuns T., Schaller M., Crain R. A., McAlpine S., 2016, preprint, (arXiv:1607.07445)

Boylan-Kolchin M., Bullock J. S., Kaplinghat M., 2011, MNRAS, 415, L40

Brook C. B., et al., 2011, MNRAS, 415, 1051

Burrage C., Copeland E. J., Millington P., 2016, preprint, (arXiv:1610.07529)

Chevalier R. A., 1974, ApJ, 188, 501

Cowie L. L., McKee C. F., 1977, ApJ, 211, 135

Dalla Vecchia C., Schaye J., 2008, MNRAS, 387, 1431

Dalla Vecchia C., Schaye J., 2012, MNRAS, 426, 140

Di Cintio A., Lelli F., 2016, MNRAS, 456, L127

Dobbs C. L., 2015, MNRAS, 447, 3390

Gentry E. S., Krumholz M. R., Dekel A., Madau P., 2017, MNRAS, 465, 2471

Girichidis P., et al., 2016, ApJ, 816, L19

Governato F., et al., 2010, Nature, 463, 203

Hopkins P. F., Quataert E., 2010, MNRAS, 407, 1529

Hopkins P. F., Kereš D., Oñorbe J., Faucher-Giguère C.-A., Quataert E., Murray N., Bullock J. S., 2014, MNRAS, 445, 581

Jubelgas M., Springel V., Enßlin T., Pfrommer C., 2008, A&A, 481, 33

Katz N., 1992, ApJ, 391, 502

Kauffmann G., et al., 2003, MNRAS, 346, 1055

Keller B. W., Wadsley J., Benincasa S. M., Couchman H. M. P., 2014, MNRAS, 442, 3013

Keller B. W., Wadsley J., Couchman H. M. P., 2015, MNRAS, 453, 3499

Keller B. W., Wadsley J., Couchman H. M. P., 2016, MNRAS,

Kennicutt Jr. R. C., 1998, ApJ, 498, 541

Kereš D., Katz N., Davé R., Fardal M., Weinberg D. H., 2009, MNRAS, 396, 2332

Kimm T., Cen R., Devriendt J., Dubois Y., Slyz A., 2015, MNRAS, 451, 2900

Klypin A., Kravtsov A. V., Valenzuela O., Prada F., 1999, ApJ, 522, 82

Kormendy J., Ho L. C., 2013, ARAA, 51, 511

Lagos C. d. P., Lacey C. G., Baugh C. M., 2013, MNRAS, 436, 1787

Larson R. B., 1974, MNRAS, 169, 229

Lelli F., McGaugh S. S., Schombert J. M., 2016, preprint, (arXiv:1606.09251)

Ludlow A. D., et al., 2016, preprint, (arXiv:1610.07663)

Mac Low M.-M., McCray R., 1988, ApJ, 324, 776

Marasco A., Fraternali F., Binney J. J., 2012, MNRAS, 419, 1107

Mashchenko S., Couchman H. M. P., Wadsley J., 2006, Nature, 442, 539

McGaugh S., Lelli F., Schombert J., 2016, preprint, (arXiv:1609.05917)

Moffat J. W., 2016, preprint, (arXiv:1610.06909)

Moore B., 1994, Nature, 370, 629

Murray N., Quataert E., Thompson T. A., 2010, ApJ, 709, 191

Navarro J. F., White S. D. M., 1993, MNRAS, 265, 271

Pontzen A., Governato F., 2012, MNRAS, 421, 3464

Rogers H., Pittard J. M., 2013, MNRAS, 431, 1337

Rosdahl J., Schaye J., Dubois Y., Kimm T., Teyssier R., 2016, preprint, (arXiv:1609.01296)

Roškar R., Teyssier R., Agertz O., Wetzstein M., Moore B., 2014, MNRAS, 444, 2837

Sawala T., et al., 2016, MNRAS, 457, 1931

Schaye J., et al., 2015, MNRAS, 446, 521

Simon J. D., Bolatto A. D., Leroy A., Blitz L., Gates E. L., 2005, ApJ, 621, 757

Spergel D. N., Steinhardt P. J., 2000, Physical Review Letters, 84, 3760

Stark A. A., Carlson E. R., 1984, ApJ, 279, 122

Stinson G., Seth A., Katz N., Wadsley J., Governato F., Quinn T., 2006, MNRAS, 373, 1074

Stinson G. S., Brook C., Macciò A. V., Wadsley J., Quinn T. R., Couchman H. M. P., 2013, MNRAS, 428, 129

Thacker R. J., Couchman H. M. P., 2000, ApJ, 545, 728

Tremmel M., Governato F., Volonteri M., Quinn T. R., 2015, MNRAS, 451, 1868

Veilleux S., Cecil G., Bland-Hawthorn J., 2005, ARAA, 43, 769

Verlinde E. P., 2016, preprint, (arXiv:1611.02269)

Vogelsberger M., et al., 2014, MNRAS, 444, 1518

Wakker B. P., van Woerden H., 1997, ARAA, 35, 217

Walch S. K., Whitworth A. P., Bisbas T., Wünsch R., Hubber D., 2012, MNRAS, 427, 625

Weiner B. J., et al., 2009, ApJ, 692, 187